APPLICATIONS OF NONLINEAR OPTICS TO THE DEVELOPMENT OF ALL-SOLID-STATE SOURCES OF TUNABLE LIGHT.

Yan Tang

A Thesis Submitted for the Degree of PhD
at the
University of St Andrews

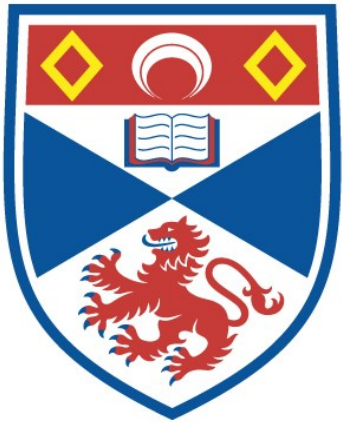

1997

University of St Andrews
School of Physics and Astronomy
St Andrews, Fife
KY16 9SS

Applications of Nonlinear Optics to the Development of All-Solid-State Sources of Tunable Light

A thesis presented to the University of St Andrews
in application for the degree of Doctor of Philosophy.

by

Yan Tang
(School of Physics and Astronomy)

April 1997

ProQuest LLC.
789 East Eisenhower Parkway
P.O. Box 1346
Ann Arbor, MI 48106 – 1346

Declaration

I, Yan Tang, hereby certify that this thesis, which is approximately 50000 words in length, has been written by me, that it is the record of work carried out by me and that has not been submitted in any previous application for a higher degree.

date 22/4/97 signature of candidate .....

I was admitted as a research student in November, 1993 and as a candidate for the degree of Doctor of Philosophy in April, 1997; the higher study for which this is a record was carried out in the University of St. Andrews between 1993 and 1997.

date 22/4/97 signature of candidate .....

I hereby certify that the candidate has fulfilled the conditions of the Resolution and Regulations appropriate for the degree of Doctor of Philosophy in the University of St. Andrews and that the candidate is qualified to submit this thesis in application for that degree.

date 22/4/97 signature of supervisor .....

In submitting this thesis to the University of St. Andrews I understand that I am giving permission for it to be made available for use in accordance with the regulations of the University Library for the time being in force, subject to any copyright vested in the work not being affected thereby. I also understand that the title and abstract will be published, and that a copy of the work may be made and supplied to any bona fide library or research worker.

date 22/4/17 signature of candidate .....

Acknowledgements

First and foremost I would like to thank my research supervisor, Professor Malcolm Dunn, for his guidance, encouragement and invaluable advice during the period of this work. I would also like to thank my joint supervisor, Professor Wilson Sibbett, for kindly help in many aspects. I also wish to acknowledge the Women Centenary Fellowship Committee for awarding me the research fellowship and all the financial support during my three year's study.

This is an opportunity to say especial thanks to my colleague Cameron Rae for his generous help, discussion and support through all of my work and patience in correcting all my English writing. I am also grateful to Christian Rahlff for the early collaboration on the construction of the slab geometry laser. I also wish to express my thanks to Finlay Colville, for many helpful discussions regarding the OPO theory and for one very useful suggestion from him in building a folded cavity to detect the idler wave of the KTP OPO. My thanks also should go to my colleagues, Garry Morrison and Dominic Withers for their kindly help whenever I need a hand in my work. In this opportunity, I also wish to thank Jian Wang for helpful discussion in the late stage of my work and the help to enable me to use LaTeXto write my thesis.

Finally, I wish to thank my husband, Dr. Yong Cui, without his encouragement, I don't think I could have reached this stage.

Publications and Papers

"Low threshold, high efficiency and widely tunable infrared source from a KTP based OPO", Yan Tang, Cameron F. Rae, Christian Rahlff and Malcolm H. Dunn, (paper has been submitted to *J. Opt. Soc. Am. B*, in March 1997).

"Tuning, threshold and conversion efficiency properties of critically phase-matched KTP OPOs", Y. Tang, C. F. Rae and M. H. Dunn, in Conference on Lasers and Electro-Optics (Anaheim, California, 1996), *OSA Technical Digest Series*, Paper CWF14, 266 (1996).

"High repetition-rate, mid-infrared KTA-OPO at 3.44 μm", C. Rahlff, Y. Tang, W. Sibbett and M. H. Dunn, in Conference on Lasers and Electro-Optics (Anaheim, California, 1996), *OSA Technical Digest Series*, Paper CWF16, 267 (1996).

"Thermal dependence of the principal refractive indices of lithium triborate", Y. Tang, Y. Cui, and M. H. Dunn, *J. Opt. Soc. Am. B*, **12**, 638-643 (1995).

"Low-threshold operation of an all-solid-state KTP optical parametric oscillator", J. A. C. Terry, Y. Cui, Y. Tang, W. Sibbett and M. H. Dunn, *J. Opt. Soc. Am. B*, **11**, 758-769 (1994).

"Comparison of lithium triborate and beta barium borate as nonlinear media for optical parametric oscillators", M. H. Dunn, Y. Cui, A. J. Henderson, G. Roberson, Y. Tang, D. E. Withers, W. Sibbett, and B. D. Sinclair *J. Opt. Soc. Am. B* **10**, 1737-1743 (1993).

"Widely tunable of all-solid-state optical parametric oscillator for the visible and near infrared", Y. Cui, D. E. Withers, C. F. Rae, C. J. Norrie, Y. Tang, B. D. Sinclair, W. Sibbett, and M. H. Dunn, *Opt. Lett.* **18**, 122 (1993).

"All-solid-state optical parametric oscillator for the visible", Y. Cui, M. H. Dunn, C. J. Norrie, W. Sibbett, B. D. Sinclair, Y. Tang, and J. A. C. Terry, *Opt. Lett.* **17**, 646 (1992).

"All-solid-state optical parametric oscillator for the visible", Y. Cui, M. H. Dunn, C. J. Norrie, W. Sibbett, B. D. Sinclair, Y. Tang, and J. A. C. Terry, in Conference on Lasers and Electro-Optics (Anaheim, California, 1992), *OSA Technical Digest Series*, **12**, Paper CTuR1, 198 (1992).

"A lithium triborate optical parametric oscillator pumped at 266 nm", Y. Tang, Y. Cui, and M. H. Dunn, *Opt. Lett.* **17**, 192 (1992).

"A lithium triborate optical parametric oscillator pumped at 266 nm", Y. Tang, Y. Cui, and M. H. Dunn, in 1991 European Quantum Electronics Conference and Tenth National Quantum Electronics Conference (Heriot-Watt University, Edinburgh, August 27th-30th, 1991). *91 EQEC Technical Digest*, Post-deadline paper PD 8, 14 (1991).

Abstract

This thesis describes the development of singly-resonant optical parametric oscillators (OPOs) based on the nonlinear material KTP (potassium titanyl phosphate), and used to provide tunable light in the infrared, with low oscillation threshold and high efficiency. Further, the generation of tunable red light by the frequency mixing of the signal wave from the OPO with the pump wave in a non-critical temperature phase-matched lithium triborate crystal (LBO) is reported. We believe this is the first demonstration of such an application of LBO.

Two diode-pumped solid-state lasers were used as the pump sources. One was an electro-optically Q-switched Nd:YLF laser which provided high peak power ($\sim$600 kW) pulses; and the other one was an acousto-optically Q-switched slab-geometry Nd:YLF laser which provided high repetition rate (1$\sim$10 kHz) and low peak power($\leq$30 kW) pulses. A second version of the acousto-optically Q-switched slab-geometry Nd:YLF laser was designed and constructed with improvements in the pump module and cooling system so as to be much more compact and easier to control.

In the first stage of this work, two theoretical models were constructed. One was a model for pump threshold of singly-resonant OPOs for the case of focused Gaussian beams, and was based on Guha's theory. The second one was a model for conversion efficiency of singly-resonant OPOs, for the case of plane waves with pump depletion, and was derived from the coupled wave equations.

In the second stage of this work, the effects of beam focusing and Poynting vector walk-off on pump threshold and conversion efficiency for OPOs were extensively studied theoretically and experimentally. Experimental results were found to be in good agreement with theory. The high pump threshold of the critically phase-matched KTP OPO led to several other pump configurations being considered, including intracavity OPOs, cylindrical focusing, and double-pass of the pump. As a result of the KTP OPO study, very low pump thresholds were achieved in both non-critical phase-matched (NCPM) and critical phase-matched (CPM) KTP OPOs by using long crystal in both intracavity OPOs and

the double-pass-pump configuration. Maximum external conversion efficiency from pump to signal was demonstrated to be 37% for the NCPM OPO and 40% for the CPM OPO. The signal wavelength tuning ranges were observed to be 1.54-1.56 μm from the NCPM KTP OPO, and 1.58-1.8 μm from the CPM KTP OPO.

In the final stage of this work, the temperature phase-matching properties of LBO were investigated with the use of our measured thermo-optical coefficients of LBO. A particularly interesting result of the investigation is the possibility of sum-frequency generation in non-critically phase-matched LBO with temperature tuning giving considerable wavelength ranges for both the type I and type II geometries. Experimentally, we demonstrated tunable red light generation by sum-frequency mixing of the 1 μm pump wave and the signal wave of the KTP OPO with an over all conversion efficiency of more than 13%. The wavelength tuning range was observed to be 0.62-0.65 μm. The effects of beam focusing on the conversion efficiency for sum-frequency generation were analysed theoretically, and several opportunities for further improvement were shown clearly from this analysis.

Contents

Chapter 1

Introduction

In recent years, the great progress in diode-pumped solid-state lasers and nonlinear materials has opened up opportunities for exciting developments of nonlinear optical frequency conversion. Highly efficient, reliable, compact, and long-lived coherent radiation sources with flexible frequency choice are not only seen in the laboratory but also in the commercial marketplace. The spectral range covered by developed nonlinear optical devices now can be throughout the ultraviolet to the far-infrared. Even so, there is still a great deal of room left for the study and development of nonlinear optical frequency conversion techniques. For example, we know that as one of the most useful materials in the infrared, KTP has been used for non-critically phase-matched (NCPM) OPOs pumped at 1 μm, and has received a great deal of attention because it is able to operate with a low power laser pump and at high efficiency at the useful eye-safe signal output wavelength of 1.5 μm. However, it cannot be wavelength-tuned effectively. An interesting question then comes up, namely can a critical phase-matched (CPM) KTP OPO operate at low power pump with reasonably high efficiency? This would be important for improving the availability of practical tunable sources in the infrared region. In addition, as we know, it is also difficult to get tunable radiation in the ultraviolet. Currently, LBO is the only crystal which is phase-matchable down to 0.16 μm and has potential for temperature tuning over the uv region. However, until recently, temperature-tuned LBO has been mostly used for OPOs pumped in the near ultraviolet or green [1, 2], and not much attention has been paid to sum-frequency generation for extending tuning ranges to shorter wavelengths.

Based on the study of nonlinear optical frequency conversion, this thesis describes the development of singly-resonant KTP OPOs and frequency up-conversion from such OPOs using sum-frequency mixing of their outputs with that of the pump laser in non-critically

phase-matched LBO. The principal goal of this work is to investigate the feasibility of low threshold, high efficiency operation of an OPO using only modest pump energies available from diode-pumped Q-switched Nd:YLF lasers, and the feasibility of improving spectral coverage in the infrared and uv regions. In order to develop all-solid-state tunable sources, all the nonlinear frequency conversion devices developed in this work were based on the use of diode-pumped Nd:YLF lasers.

1.1 All-solid-state tunable optical parametric oscillator

Right from the first demonstration of the laser, an important goal has been the development of widely-tunable devices covering many spectral regions.

In early times, dye lasers and color center lasers were the only available sources for generating tunable light. The range of the spectrum covered by dye lasers using different dyes can be 0.4-1 μm; and it can be 0.8-4 μm from color center lasers. However both types of lasers are inconvenient to use either because fresh dye solution must be constantly flowed through the active region for a dye laser, or because of the cryogenic temperature needed for operation for a color center laser.

Vibronic crystal lasers were a more recent and exciting development, as convenient and now widely-used tunable sources. However, the tuning range with each crystal is limited to a small range.

In contrast with the above, the optical parametric oscillator is the most convenient source to use, since it can convert laser light at one frequency to a broad frequency range, while preserving the general characteristics of the initial input wave.

The principles of OPOs have been well known for more than 30 years now. Just shortly after the invention of the laser, the first OPO was demonstrated by Giordmaine and Miller (in 1965)[3, 4]. However, because of the poor quality of available laser sources and nonlinear optical crystals, the development on parametric devices was slow, and effective and practical OPOs have not appeared until recent years. Since the late 1980s, the development of new nonlinear materials, and improvements in the techniques used to grow crystals and in the degree of purity of the raw materials used in these processes has led to the general availability of materials with higher nonlinear coefficient, high damage threshold and high optical quality. Further, the development of diode lasers has led to novel pump schemes for solid-state lasers with the advantages of compact, highly-efficient devices with narrow

linewidth and much improved spatial mode quality. These two significant advances are opening the door for a new generation of compact, reliable and widely tunable sources, which are named: *all-solid-state tunable sources.* A typically example of such a device is illustrated in Fig. 1.1. Basically the system includes a diode-pumped solid-state laser [often, it is a neodymium (Nd) laser.], an optional frequency up-converter, and an optical parametric oscillator. It can be seen that all the radiation generation processes in an all-solid-state tunable source are carried out entirely within the solid-state phases.

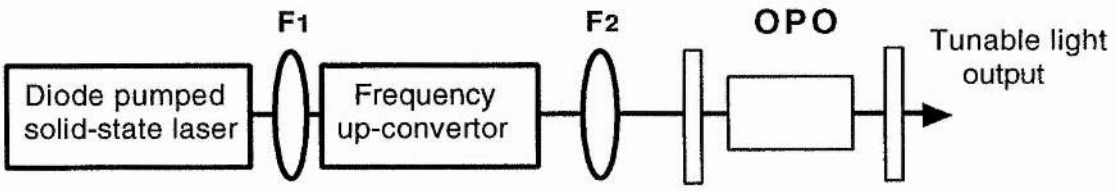

Figure 1.1: Configuration of an all-solid-state tunable source.

1.2 Tunable lights in infrared

The development of tunable radiation sources has long been of interest in the infrared region. The presence of many molecular vibrational lines makes that region attractive for spectroscopy, with uses from basic research to petroleum exploration. Strong water lines are promising for medical treatment and for applications such as sensing water content in integrated-circuit packages. Military agencies are also looking at this spectral region for laser countermeasures against sensors. Because of eye safety, infrared radiation is attractive for applications such as laser radar, remote sensing, and range-finding.

However, the lack of good tunable laser sources in this region has hindered development of these applications. Lead-salt and color-center lasers are tunable, but their inherent limitations have restricted their use. Free-electron lasers and chemical lasers are much more powerful but have their own operation restrictions. In contrast, OPOs with the possibilities of broader tunability over much of this region and generating millijoule, nanosecond pulses in a more manageable package are promising to replace the above infrared lasers for these applications.

There are several nonlinear materials for infrared OPOs such as BBO, LBO, KTP, and $LiNbO_3$, some relevant properties of those crystals for the use in infrared OPOs are listed

Table 1.1: Some properties of nonlinear crystals for infrared OPO.

Material	Transparency	Non-linearity	Figure of merit	Damage threshold
	range (μm)	d_{eff} (10^{-12}m/V)	d^2/n^3 ($10^{-24}m^2/V^2$)	ns pulses (GW/cm^{-2})
LiB_3O_5	0.16-2.6	0.85	0.18	20
β-BaB_2O_4	0.19-2.6	2	0.94	14
$KTiPO_4$	0.35-4.5	3.2	1.84	1 (10 ns)
$LiNbO_3$	0.33-5.5	5.44	3.1	10
$LiIO_3$	0.31-5	1.8	0.64	2
$AgGaS_2$	0.5-13	13.4	13.2	0.02 (10 ns)
$AgGaSe_2$	0.71-18	33	59.5	0.03 (50 ns, 2 mm)
$ZnGeP_2$	0.74-12	88	247.8	0.05 (25 ns, 2 mm)

in Table 1.1. The choice of crystal depends on operating conditions, available pump source wavelength and pump energy level.

In early times, the work was concentrated on the use of materials such as $LiNbO_3$ and $LiIO_3$. However, these materials suffered many problems, in particular, the problem of low damage threshold, which limited the infrared OPOs from operating at high power and high efficiency.

The large nonlinear coefficients and extended infrared transparency ranges make chalcopyrite crystals an important class for infrared parametric devices. But the useful crystals in this family, $ZnGeP_2$, $AgGaS_2$, and $AgGaSe_2$, suffer from low optical damage intensities. An interesting possibility is the feasibility of tuning the entire range from 2.3 to 18 μm using a single $AgGaSe_2$ crystal pumped by a Ho:YAG laser at 2.05 μm.

Since the last decade, the newly developed materials: BBO, LBO, KTP and its isomorphs, with their several attractive properties of large d_{eff}, high damage threshold and wide transparency range, have given great promises for high efficiency parametric applications in the spectral regions of infrared.

A typical example of a BBO based parametric device for the infrared is the third-harmonic of Nd:YAG laser pumped OPO, in which the entire near uv to mid infrared range from 415 nm to 2.5 μm can be covered. From such an OPO, more than 30% total efficiency (in terms of useful outputs at the signal and idler wavelengths) in a walk-off compensated configuration has been reported by Bosenberg *et al.* [5].

The LBO based OPOs in the infrared region also are important. The high damage threshold and lower birefringence of LBO have made it an interesting material for uv pumped broadly tunable OPOs using only modest energies from diode-pumped solid-state lasers and tight focusing. Moreover, LBO allows for temperature tuning over its entire tuning range under non-critical phase-matching conditions. For example, as reported by Lin *et al.* [6], with the use of LBO and pump at 0.532 μm, the wavelength can be tuned over a broad spectral range from 0.65 μm to 2.5 μm in a type I NCPM temperature tuning geometry.

For infrared OPO, pump wavelength is an important consideration. Principally, with the use of suitable nonlinear material and the 1 μm pump light from the primary pump laser, tunable radiation in infrared spectral region can be produced effectively in only a single-step process. Pump wavelength is also important particularly when it is recognised that phase-matching and oscillation become more difficult as the difference between signal and idler beams increases. Thus 1 μm neodymium lasers work much better as pumps for OPOs emitting 2 to 3 μm radiation than for generating longer signal wavelengths.

KTP can be phase-matched at 1 μm, and meets many key requirements for high efficiency parametric devices as seen in the Table 1.1. Previous works have shown that the NCPM KTP OPO can be operated at a low pump power with high efficiency. For instance, Marshall *et al.* have reported for 47% external conversion efficiency from pump to signal in a singly-resonant device[7]; and Terry *et al.* reported a low pump threshold of around 0.5 mJ [8]. The disadvantage of this OPO is the slow wavelength tuning rate. As the phase-matching angle of KTP is turned away from the NCPM point (θ=90°), the phase-matching becomes a critical geometry, and the wavelength tuning rate in such a geometry increases sharply. The entire wavelength tuning range for a 1 μm pumped KTP OPO is 1.5-3.3 μm, which covers the greater part of the mid-infrared region. Until now, although the wide tuning range in the infrared spectral region is so important, the 1 μm pumped KTP OPO in a CPM geometry has only been mentioned in a few publications [9, 10] with no investigation of efficiency and pump threshold. We believe this is because of the walk-off problem in the CPM geometry. In fact, it is notable that there are two attractive features in the CPM KTP OPO when the crystal is oriented on either the $x-z$ plane or $y-z$ plane, and there are the large d_{eff} ($\geq$ 2 pm/V) over all the phase-matchable regions, and the occurrence of only one extraordinary wave (it is the idler in type III, and the signal in type II). These would certainly give advantages for a singly-resonant CPM OPO in increasing efficiency and reducing threshold.

Alternative materials to KTP are its isomorphs, *e.g.* KTA, RTA, and CTA. These are relatively new crystals and have very similar wavelength tuning properties to that of the KTP but with much broader transparency ranges of 0.35 - 5.3 μm. Therefore the study of a KTP based OPO is also useful for the further work with the use of its isomorphs for OPOs to extend the tuning range to $4 \sim 5$ μm.

Another notable advance recently in the field of infrared OPOs is the use of periodically poled lithium niobate (PPLN) for quasi-phase-matching (QPM). QPM was proposed before birefringence phase-matching[11], but difficulties in fabrication QPM materials have prevented its application. Recent advances in fabricating practical QPM materials have renewed interest in this approach. PPLN has very large effective nonlinearity (d_{eff}), and with suitable period it can provide non-critical phase-matching for generation of any wavelengths in its transmission range from 0.35 - 4 μm. The main disadvantage of PPLN currently is its small aperture due to the limitation of fabrication. This has restricted the applications in low power pump case, such as fs lasers and cw lasers pumped OPOs. The first PPLN synchronously pumped OPO has been demonstrated by Butterworth *et al.* [12]. In this experiment, a frequency-doubled diode-pumped APM Nd:YLF laser was used as the pump, the OPO can be temperature tuned over the range of 0.9 -1.3 μm. Also as reported in CLEO'96, the first 1 μm pumped cw singly-resonant OPO based on PPLN has been demonstrated by Bosenberg *et al.* [13], the pump threshold in this device can be as low as a few watts, and more than 1 watt of radiation with a broad tuning range in the mid-infrared was produced. Although PPLN is not suitable for Q-switched laser pumped OPOs because of the unavailability of large apertures and therefore increased risk of damage, Myers *et al.* have reported the use of a diode-pumped Q-switched Nd:YAG laser to pump the PPLN based OPO. They achieved 0.1 mJ of pump threshold, which was more than a factor of 10 below the damage limit.

1.3 Frequency up-conversion from OPO

The optical parametric oscillator provides a means of generating tunable signal and idler waves by pumping at frequency ω_p. However, when a tunable frequency ω_d is desired to be greater than the pump frequency ω_p, a single-step process based on a second-order nonlinearity does not suffice. Mainly there are two approaches which can accomplish this objective. The standard approach is the SHG+SFG+OPO, which means second harmonic generation, then optional sum-frequency mixing (THG or 4HG) followed by the OPO itself.

An alternative approach can be optical parametric oscillation followed by sum-frequency generation of the signal and residual pump, *e.g.* OPO+SFG. In the second approach, if the frequency mixing is between the signal wave and harmonic wave of the pump, this geometry means that the pump must be separated into two parts before the OPO, one part for the OPO, and other one for the harmonic generation.

The advantage of the first approach is that it is more direct than the second approach to achieve tunable radiation at short wavelength. The BBO, LBO or green pumped KTP OPOs are all examples of this approach. The shortest tuning ranges that can be reached by this approach currently are limited to the near ultraviolet region.

In contrast, there are two major advantages in the second approach. First, the possibility of extending the tunable range to the deep uv. Second, less steps of frequency harmonic generation may be required because the final stage of frequency up-conversion can bring the generated wavelength further towards short wavelengths. The theoretical and experimental investigation of sum-frequency generation between the pump and the signal in intracavity geometries were investigated just shortly after the advent of the optical parametric oscillator [14, 15]. Now, the newly developed crystals, such as BBO and LBO have opened the door for the use of the second approach in frequency up-conversion. As we know, the shortest output wavelength of BBO is limited by its cut-off wavelength in the uv region and its large birefringence also effects the output beam quality and conversion process, so that the most favourable material in this application is LBO. Recently, several results on the use of the second approach with LBO to generate radiation in uv and visible have been reported [16, 17, 18, 19, 20]. Among them, there are two interesting achievements. First, the high efficiency uv generation at 0.289 μm has been demonstrated by Marshall *et al.* [16]. They obtained 0.5 W uv output at 289 nm from a 2 W (80 Hz) 1.064 μm diode-pumped laser by frequency mixing of one wave of 0.355 μm and one wave of 1.58-1.59 μm from a KTP OPO, the overall efficiency from the pump laser to the uv was 25%. The second is where the generated tunable wavelength has reached as short as 172.7 nm as reported by Seifert *et al.* [17]. In their work, the tunable output (0.74 -0.85 μm) from a fs Ti:sapphire regenerative amplifier system was split into two equal parts for generating of fourth harmonic and tunable infrared radiation around 1.9 μm in a temperature tuned LBO OPO, and then the two waves were combined in LBO cut at $\theta = 90^o$, $\phi = 73^o$, to generate tunable fs pulsed light in the range of 172.7-187 nm. The possibility of further extending the tuning range to 160 nm (the transmission cut-off of LBO) has been pointed out by Borsutzky *et al.* [18], who have demonstrated tunable deep

uv light generation in the range of 188-242 nm from a pulsed Nd:YAG laser.

So far, there has no report of the use of temperature tuned LBO in SFG, despite the fact that the temperature tuning offers much more favourable advantages than angle tuning. This might be due to the lack of accurate thermal-optical coefficient for prediction. Therefore, we believe, the work presented in this thesis regarding the measured thermal-optical coefficients of LBO would be very useful for improving this situation and extending applications of LBO in such areas.

1.4 This work

The programme of this work is outlined in Fig. 1.2. The work were carried out in four steps, which are: (1) Construct a *cw* diode laser pumped Q-switched Nd:YLF laser; (2) Develop a 1.047 μm pumped KTP for both NCPM and CPM geometries; (3) Experimentally measure thermo-optical coefficients for LBO; (4) Generate tunable red light (0.62-0.65 μm) by frequency mixing the signal beam of the KTP OPO and the pump beam in a non-critical temperature phase-matched LBO.

A EO Q-switched diode-pumped Nd:YLF laser was used for the initial experimental study, because of its higher peak power than the that of the AO Q-switched Nd:YLF laser.

1.5 Thesis outline

The remaining seven chapters of the thesis are organised as follows: Chapter 2 gives the necessary theoretical background for the discussion of the performance of nonlinear optical frequency conversion, including the theoretical models developed to calculate efficiency for SFG and OPO, and to calculate threshold for OPO. Chapter 3 reviews briefly some useful nonlinear optical materials and describes in more detail the properties of the KTP and LBO, of which both have been used in this work. Chapter 4 gives a description of the pump sources, including the performance of the AO Q-switched *cw* diode-pumped Nd:YAG laser and its development, and the performance of the EO Q-switched pulsed diode-pumped Nd:YLF laser. Chapter 5 describes the experiment work on KTP OPO for both NCPM and CPM geometries, including detailed analysis and design considerations in this chapter. Chapter 6 describes the measurement of thermo-optical coefficient of LBO and lists all the predictions for the generation of tunable light in visible, uv and deep uv regions by the use

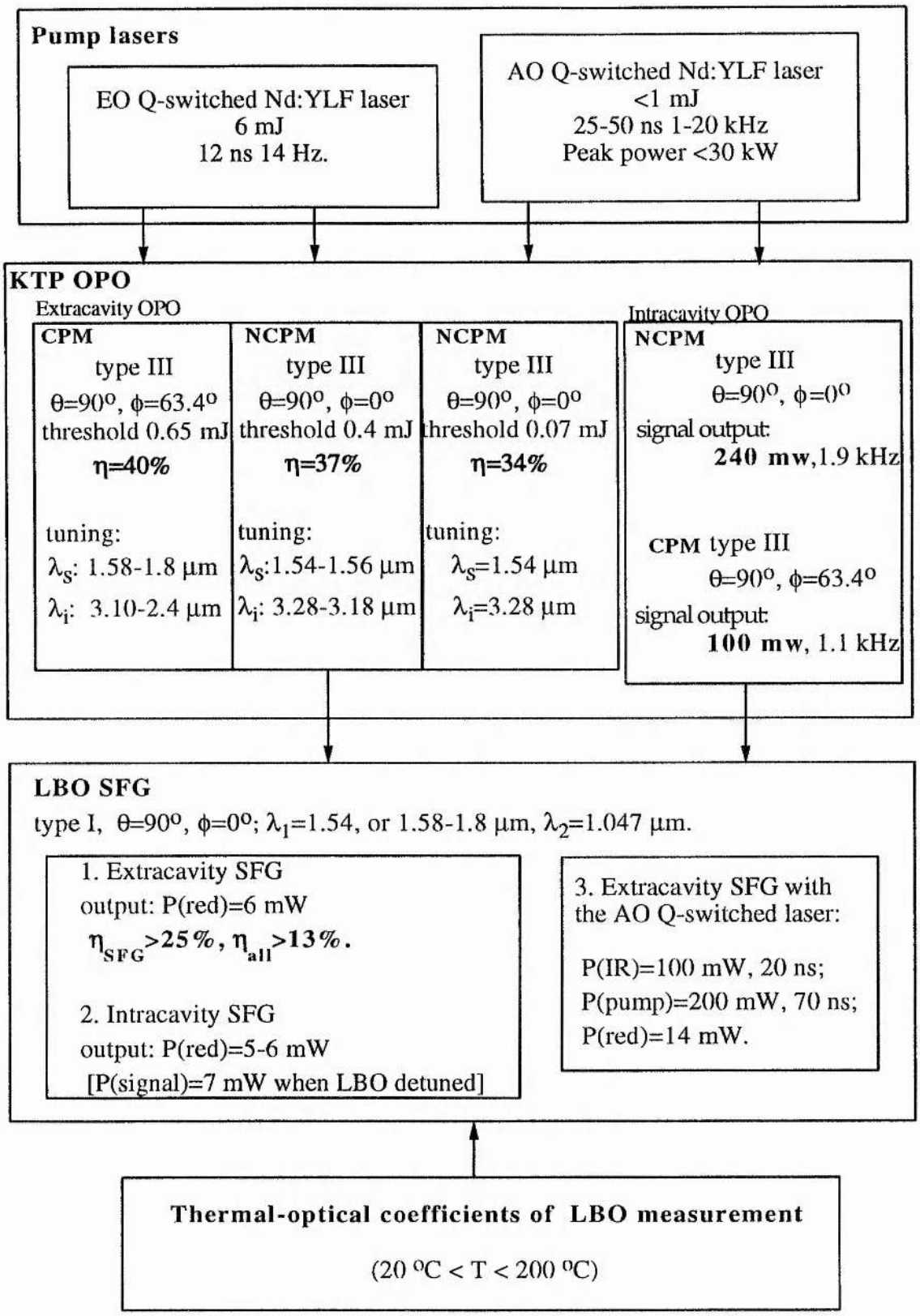

Figure 1.2: Configuration of an all-solid-state tunable source.

of temperature phase-matched LBO in the scheme of OPO + SFG. Then in Chapter 7, a brief description and discussion of the experiment on tunable red light generation with the use of the temperature phase-matched LBO and the scheme of OPO + SFG is given. The final chapter, chapter 8, discusses the achievements of this work and the direction for the future work.

Bibliography

[1] Y. Tang, Y. Cui, and M. H. Dunn, *Opt. Lett.* **17**, 192 (1992).

[2] G. Robertson, A. Henderson, and M. H. Dunn, *Opt. Lett.* **16**, 1584 (1991).

[3] C. C. Wang and G. W. Racette, *Appl. Phys. Lett.* **6**, 169 (165).

[4] J. A. Giordamaine and R. C. Miller, *Phys. Rev. Lett.* **14**, 973 (1965).

[5] W. R. Bosenberg and C. L. Tang, *Appl. Phys. Lett.* **56**, 1819 (1990).

[6] S. Lin, J. Y. Huang, J. Ling, C. Chen, and Y. R. Shen, *Appl. Phys. Lett.* **59**, 2805-2807 (1991).

[7] Alex Kaz, Larry R. Marshall, CWD1, CLEO'93.

[8] J. A. C. Terry, Y. Cui, Y. Tang, W. Sibbett, and M. H. Dunn, *J. Opt. Soc. Am. B* **11**, 758 (1994).

[9] K. Kato, *IEEE J. Quantum Electron.* **QE-27**, 1137 (1991).

[10] J. T. Lin, *Optical and Quantum Electronics* **22**, S283 (1990).

[11] J. A. Armstrong, N. Bloembergen, J. Ducuing, and P. S. Pershan, *Phys. Rev.* **127**, 1918 (1962).

[12] V. Pruneri, S. D. Butterworth, D. Hanna, *Appl. Phys. Lett.* **69**, 1029-1031, (1996).

[13] W. R. Bosenberg, et al., CThA3, CLEO'96.

[14] P. P. BEY, and C. L. Tang, *IEEE J. Quantum Electron.* **QE-8**, 361 (1972).

[15] A. J. Campillo, *IEEE J. Quantum Electron.* **QE-8**, 914 (1972).

[16] L. Marshall, *Laser Focus World* 83-87, April (1994).

[17] F. Seifert, J. Ringling, F. Noack, V. Petrov, and O. Kittelmann, *Opt. Lett.* **19**, 1538-1540 (1994).

[18] A. Borsutzky, R. Brunger, and R. Wallenstein, *Appl. Phys.* **B52**, 380-384 (1991).

[19] E. C. Cheung, Karl Koch, and Gerald T. Moore, *Opt. Lett.* **19**, 1967 (1994).

[20] B. Wu, F. Xie, C. Chen, D. Deng, and Z. Xu, *Opt. Commun.* **88**, 451-454 (1992).

Chapter 2

Theoretical Background

In this chapter, the general physical principles responsible for the second-order nonlinear optical frequency conversion process are described, and equations are derived for sum-frequency mixing and optical parametric generation processes. Additionally, in this chapter, detailed consideration is given for the design of singly-resonant OPOs, and frequency up-conversion devices, including optimum phase-matching, conversion efficiency, and threshold calculations. MKS units are adopted throughout the analysis.

2.1 The second-order nonlinear interaction

When an electromagnetic wave E, propagates through a dielectric material, it induces a polarization P. In the case where the electric field is smaller than the intra-atomic field, the response of the induced polarization will be linear, and is described by the constitutive relation

$$P = \varepsilon_o \chi^{(1)} E \tag{2.1}$$

where ε_o is the free space permittivity and $\chi^{(1)}$ is the linear susceptibility. The real part of the linear susceptibility $\chi^{(1)}$ is related to the refractive index of the medium, n, by $\chi^{(1)}=n^2-1$, and is responsible for the familiar linear optical phenomena of reflection and refraction. In the case of where the electric field strength is comparable to the intra-atomic electric field, as with laser radiation, this linear relation between induced polarization and field no longer suffices, and Eq.(2.1) is replaced by a power series in the field namely:

$$P = \varepsilon_o \chi^{(1)} E + \chi^{(2)} E^2 + \chi^{(3)} E^3 + ... \tag{2.2}$$

where $\chi^{(2)}$, $\chi^{(3)}$,....., are the nonlinear susceptibilities of the medium respectively and are tensors of the third, fourth, and higher ranks. It must be noted that although ε_o is separated from $\chi^{(1)}$, following the procedure in linear optics, this is traditionally not extended to the higher order susceptibilities[1]. Concern here is with the first nonlinear term $\chi^{(2)}$ only. This is usually referred to as the second order nonlinear susceptibility. This term is only finite in anisotropic media, and in order to describe such media the relationship is rewritten in terms of the polarization vector

$$\mathbf{P}^{(2)} = \chi^{(2)}:\mathbf{EE} \tag{2.3}$$

Consider the circumstance in which the nonlinear polarization is produced by the interaction of two waves at the frequencies ω_1 and ω_2, where[1]

$$E_1(z,t) = E_1 \cos(k_1 z + \omega_1 t)$$

and

$$E_2(z,t) = E_2 \cos(k_2 z + \omega_2 t)$$

Substituting the superposition of these two waves for $\mathbf{E}$, and assuming that $\mathbf{P}$ and $\mathbf{E}$ are along the same direction z, then we expect the nonlinear polarization to be of the form

$$P^{(2)} = \chi^{(2)}[E_1^2 \cos^2(k_1 z + \omega_1 t) + E_2^2 \cos^2(k_2 z + \omega_2 t)$$

$$+2E_1 E_2 \cos(k_1 z + \omega_1 t)\cos(k_2 z + \omega_2 t)]$$

The polarization then consists of a number of components with different frequencies; that

[1] In general, these two waves do have different phases and, strictly, they should be written as follows:

$$E_i(z,t) = E_i \cos(\omega_i t + k_i z + \phi_i) \qquad i = 1, 2$$

is[2],

$$P_{2\omega_1} = \frac{1}{2}\chi^{(2)}E_1^2\cos[2(k_1z+\omega_1t)] \qquad (SHG) \tag{2.4}$$

$$P_{2\omega_2} = \frac{1}{2}\chi^{(2)}E_2^2\cos[2(k_2z+\omega_2t)] \qquad (SHG) \tag{2.5}$$

$$P_{\omega_1+\omega_2} = \chi^{(2)}E_1E_2\cos[(\omega_1+\omega_2)t+(k_1+k_2)z)] \qquad (SFG) \tag{2.6}$$

$$P_{\omega_1-\omega_2} = \chi^{(2)}E_1E_2\cos[(\omega_1-\omega_2)t+(k_1-k_2)z)] \qquad (DFG) \tag{2.7}$$

and a steady term,

$$P_0 = \chi^{(2)}(E_1^2+E_2^2) \qquad (OR) \tag{2.8}$$

Here each expression has been labelled by the name of the physical process that it describes, such as second-harmonic generation (SHG), sum-frequency generation (SFG), difference-frequency generation (DFG), and optical rectification (OR). Considering the general case for SHG, that is the two waves are derived from one fundamental beam, and so E_1=E_2, k_1=k_2, and ω_1=ω_2, then equations (2.4) and (2.5) can be combined and rewritten as

$$\begin{aligned} P_{2\omega} &= P_{2\omega_1} + P_{2\omega_2} \\ &= \chi^{(2)}E^2\cos[2(kz+\omega t)] \end{aligned} \tag{2.9}$$

Therefore, the process of SHG is in fact a special case of SFG and can be described by Eq.(2.6). The processes of sum-frequency generation and difference-frequency generation are illustrated in Fig. 2.1 and Fig. 2.2 respectively. One interesting application of sum-frequency generation is to produce tunable radiation in the visible and ultraviolet spectral region by choosing one of the input waves to be a fixed frequency, and the other to be frequency tunable.

One important difference between the two processes of SFG and DFG can be deduced from the description of difference-frequency generation in terms of a photon energy-level

[2]Also the convention (see Ref.[1], P. 3) that the real field is given by

$$E_R = \frac{1}{2}(Ee^{i(kz+\omega t)} + E^*e^{-i(kz+\omega t)}) = R_e(Ee^{i(kz+\omega t)})$$

another common convention has been used, although, (see Ref.[2], P.7) is to define the real field as

$$E_R = (Ee^{i(kz+\omega t)} + E^*e^{-i(kz+\omega t)}) = 2R_e(Ee^{i(kz+\omega t)})$$

This results in the expressions for the nonlinear polarization component differing by factor of 2 from Eqs. (2.4) -(2.7). That is:

$$P_{\omega_1\pm\omega_2} = 2\chi^{(2)}E_1E_2\cos[(\omega_1\pm\omega_2)t+(k_1\pm k_2)z)]$$

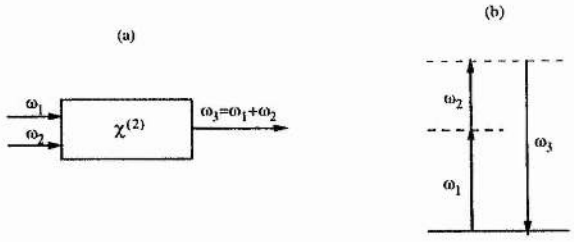

Figure 2.1: Sum-frequency generation. (a) Geometry of the interaction. (b) Energy-level description.

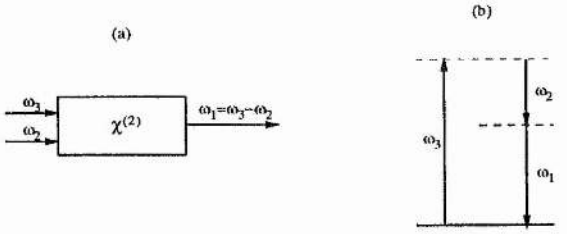

Figure 2.2: Difference-frequency generation. (a) Geometry of the interaction. (b) Energy-level description.

diagram [part(b) of Fig. 2.2]. The conservation of energy requires that for every photon that is created at the difference-frequency ω_1, an input photon at the higher frequency ω_3 must be destroyed and a photon at the lower frequency ω_2 must be created. Thus, the lower-frequency input field is amplified by the process of DFG. For this reason, the process of difference-frequency generation is also known as optical parametric amplification (OPA).

If a nonlinear crystal used in a process of optical parametric amplification is placed inside an optical resonator, as shown in Fig. 2.3, the ω_2 and/or ω_1 fields, and if so desired the $\omega_3 = \omega_1 + \omega_2$ field can be made large through parametric amplification and resonant processes. Such a device is known as an optical parametric oscillator.

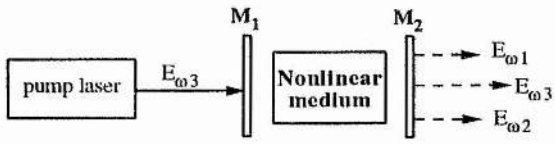

Figure 2.3: A general schematic of an optical parametric oscillator.

2.1.1 Nonlinear susceptibility and the d-effective coefficient

As previously mentioned, $\chi^{(2)}$ is a third-rank tensor with 27 components in the form of $\chi^{(2)}_{ijk}(\omega_3 = \omega_1 + \omega_2)$ when an interaction of the form, $\omega_3 = \omega_1 + \omega_2$ is considered. The indices ijk refer to the Cartesian components of the fields. In general, $\chi^{(2)}$ is dependent on the frequencies of all the fields involved in the nonlinear interaction. Under the assumptions of lossless media and negligible dispersion over the whole frequency range containing ω_1, ω_2, and ω_3, a number of symmetry conditions are introduced to restrict the various components of $\chi^{(2)}$, and results in 27 essential, frequency independent components [2]. After further reduction, $\chi^{(2)}$ can then be represented in the form

$$\chi^{(2)}_{ijk}(\omega_3 = \omega_1 + \omega_2) \equiv d_{il} \tag{2.10}$$

where the relationships between the values of j, k, and l are given by

$$\begin{array}{lcccccc} jk: & 11 & 22 & 33 & 23,32 & 31,13 & 12,21 \\ l: & 1 & 2 & 3 & 4 & 5 & 6 \end{array} \tag{2.11}$$

The nonlinear susceptibility tensor is then represented by the 3 x 6 matrix

$$\mathbf{d} = \begin{pmatrix} d_{11} & d_{12} & d_{13} & d_{14} & d_{15} & d_{16} \\ d_{21} & d_{22} & d_{23} & d_{24} & d_{25} & d_{26} \\ d_{31} & d_{32} & d_{33} & d_{34} & d_{35} & d_{36} \end{pmatrix} \tag{2.12}$$

For a material in general, the nonlinear tensor $\mathbf{d}$ will be relatively straight-forward to measure for the process of second harmonic generation. When the Kleinman symmetry condition is valid, the remaining tensors describing other interactions can then be approximately derived from $\mathbf{d}(2\omega)$ as determined for the SHG process. For example, the sum-frequency generation polarization vector (with $\omega_3 = \omega_2 + \omega_1$) can be described as (see Ref. [2], page 40.)

$$\begin{pmatrix} p_x(\omega_3) \\ p_y(\omega_3) \\ p_z(\omega_3) \end{pmatrix} = \begin{pmatrix} d_{11}\ d_{12}\ d_{13}\ d_{14}\ d_{15}\ d_{16} \\ d_{21}\ d_{22}\ d_{23}\ d_{24}\ d_{25}\ d_{26} \\ d_{31}\ d_{32}\ d_{33}\ d_{34}\ d_{35}\ d_{36} \end{pmatrix} \begin{pmatrix} E_x(\omega_1)E_x(\omega_2) \\ E_y(\omega_1)E_y(\omega_2) \\ E_z(\omega_1)E_z(\omega_2) \\ E_y(\omega_1)E_z(\omega_2) + E_z(\omega_1)E_y(\omega_2) \\ E_x(\omega_1)E_z(\omega_2) + E_z(\omega_1)E_x(\omega_2) \\ E_x(\omega_1)E_y(\omega_2) + E_y(\omega_1)E_x(\omega_2) \end{pmatrix} \tag{2.13}$$

However, strictly speaking, difference-frequency generation can only be described by the same d_{il} tensor under the condition of full permutation symmetry[2], *i.e.* the indices χ_{ijk} can be freely permuted. For instance,

$$\begin{aligned} d_{12} \equiv \chi_{122} = \chi_{212} \equiv d_{26} \\ d_{14} \equiv \chi_{123} = \chi_{213} \equiv d_{25} \\ \cdots\cdots \end{aligned} \tag{2.14}$$

Under this symmetry condition, the independent elements of d_{il} reduce from 18 to 10, and the form of d_{il} under this condition becomes

$$\mathbf{d} = \begin{pmatrix} d_{11} & d_{12} & d_{13} & d_{14} & d_{15} & d_{16} \\ d_{16} & d_{22} & d_{23} & d_{24} & d_{14} & d_{12} \\ d_{15} & d_{24} & d_{33} & d_{23} & d_{13} & d_{14} \end{pmatrix} \tag{2.15}$$

Hence, for difference-frequency generation, the process is described by

$$\begin{pmatrix} p_x(\omega_1) \\ p_y(\omega_1) \\ p_z(\omega_1) \end{pmatrix} = \begin{pmatrix} d_{11}\ d_{12}\ d_{13}\ d_{14}\ d_{15}\ d_{16} \\ d_{16}\ d_{22}\ d_{23}\ d_{24}\ d_{14}\ d_{12} \\ d_{15}\ d_{24}\ d_{33}\ d_{23}\ d_{13}\ d_{14} \end{pmatrix} \begin{pmatrix} E_x(\omega_3)E_x^*(\omega_2) \\ E_y(\omega_3)E_y^*(\omega_2) \\ E_z(\omega_3)E_z^*(\omega_2) \\ E_y(\omega_3)E_z^*(\omega_2) + E_z(\omega_3)E_y^*(\omega_2) \\ E_x(\omega_3)E_z^*(\omega_2) + E_z(\omega_3)E_x^*(\omega_2) \\ E_x(\omega_3)E_y^*(\omega_2) + E_y(\omega_3)E_x^*(\omega_2) \end{pmatrix} \tag{2.16}$$

Using Eq.(2.13) to calculate the polarization, account has still to be taken of each polarization component along the principal axes of the crystal in terms of $\mathbf{E}(\omega_1)$, $\mathbf{E}(\omega_2)$ and the nonlinear coefficient tensor. For convenience, an effective second-order nonlinear coefficient d_{eff} has been introduced for practical application by forming the relationship

$$\mathbf{P}_{\omega_1+\omega_2} = d_{eff}\mathbf{E}(\omega_1)\mathbf{E}(\omega_2) \tag{2.17}$$

Boyd and Kleinman [3] have given the relationship between d_{eff} and the nonlinear coefficient tensor $d_{il}(2\omega)$ as:

$$d_{eff} = \mathbf{U}_3 \bullet \mathbf{d}(2\omega) : \mathbf{U}_1\mathbf{U}_2 \tag{2.18}$$

where $\mathbf{U}_i$ are the unit vectors denoting the direction of the polarization of the electric fields $\mathbf{E}_i$ within the crystal and at frequencies ω_i $(i = 1, 2, 3)$. In order to obtain a direct expression of d_{eff} from Eq.(2.18), the components of unit vectors $\mathbf{U}_i(i = 1, 2, 3)$ need to be known first. If one takes k as the unit wave vector, then the wave vector can be given by

$$\mathbf{K} = n(\frac{\omega}{c})\mathbf{k} \tag{2.19}$$

where the directional orientation of k is described by resolving k onto the three principal axes through the relationships: $k_x = \sin\theta\cos\phi$, $k_y = \sin\theta\sin\phi$, and $k_z = \cos\theta$; n is the refractive index in the propagation direction; θ is the angle between the wave propagation direction k and the z axis; and ϕ is the angle from the x axis in the $x - y$ plane. From Maxwell's equations, the components of $\mathbf{E}$ now can be derived to be

$$E_i = \frac{k_x}{n^2 - n_x^2} n^2(\mathbf{k} \bullet \mathbf{E}) \tag{2.20}$$

where $i = x, y, z$; n_x, n_y, and n_z are the principal refractive indices of crystal. The direction cosines of the electric field of a monochromatic plane wave propagating in the direction k inside a nonlinear crystal can be written as

$$\begin{aligned}
\cos\alpha &= \frac{k_x}{n^2 - n_x^2}\left[\left(\frac{k_x}{n^2 - n_x^2}\right)^2 + \left(\frac{k_y}{n^2 - n_y^2}\right)^2 + \left(\frac{k_z}{n^2 - n_z^2}\right)^2\right]^{-\frac{1}{2}} \\
\cos\beta &= \frac{k_y}{n^2 - n_y^2}\left[\left(\frac{k_x}{n^2 - n_x^2}\right)^2 + \left(\frac{k_y}{n^2 - n_y^2}\right)^2 + \left(\frac{k_z}{n^2 - n_z^2}\right)^2\right]^{-\frac{1}{2}} \\
\cos\gamma &= \frac{k_z}{n^2 - n_z^2}\left[\left(\frac{k_x}{n^2 - n_x^2}\right)^2 + \left(\frac{k_y}{n^2 - n_y^2}\right)^2 + \left(\frac{k_z}{n^2 - n_z^2}\right)^2\right]^{-\frac{1}{2}}
\end{aligned} \tag{2.21}$$

As it has been well known, an optical wave $\mathbf{E}(\omega_i)$ propagating in a anisotropic medium with a wave vector $\mathbf{K}(\theta, \phi)$ can be decomposed into two eigen components with mutually perpendicular polarization directions, denoted by $\mathbf{E}(\omega_i)_a$ (slow ray) and $\mathbf{E}(\omega_i)_b$ (fast

ray). Therefore, the cosine vector of an electric field $\mathbf{E}(\omega_i)_l$ propagating in a crystal with polarization l can be written as:

$$\mathbf{U}(\omega_i)_l : \quad \cos\alpha(\omega_i)_l, \quad \cos\beta(\omega_i)_l, \quad \cos\gamma(\omega_i)_l. \tag{2.22}$$

where l denotes a or b for the two eigen components.

Finally, the mathematical expression of d_{eff} in a very general form for a three wave interaction process can be written as:

$$\begin{aligned} d_{eff} &= \mathbf{U}_3 \bullet \mathbf{d}(\omega_1 + \omega_2) \colon \mathbf{U}_1\mathbf{U}_2 \\ &= \textstyle\sum_{i\zeta} U_{3i} d_{i\zeta}(\omega_1 + \omega_2)(\mathbf{U}_1\mathbf{U}_2)_\zeta \end{aligned} \tag{2.23}$$

where U_{3i} is the ith component of the unit vector $\mathbf{U}_3$, $(i = x, y, z)$; $d_{i\zeta}(\omega_1 + \omega_2)$ is the nonlinear coefficient tensor, $(\zeta = 1, 2, ...6.)$, and $(\mathbf{U}_1\mathbf{U}_2)_\zeta$ is the ζth component of a column vector.

It is important to note that we have adopted MKS units throughout the theoretical analysis and that the d_{eff} coefficient is derived from the definition (2.3). Hence, the unit of d_{eff} are $coulombs.volt^{-2}$. However there is an alternative convention, in which the nonlinear susceptibility is defined through the equation

$$\mathbf{P}^{(2)} = \varepsilon_0 \chi^{(2)} \colon \mathbf{EE} \tag{2.24}$$

In this case the units of $\chi^{(2)}$ are $metres\ volt^{-1}$(or pm/V). To convert from one convention to the other, the conversion factor used is

$$pm/V = 10^{-9}/(36 \times \pi) \bullet coulomb/V^2 \tag{2.25}$$

2.1.2 Optics of crystals and double refraction

(1) Uniaxial crystal: Within a uniaxial crystal a particular propagation direction exists called the *optic axis* or z axis, for which the observed birefringence is zero. The birefringence is maximised if beam propagation is normal to this direction. The plane containing the z axis and the wave vector k is named the *principal plane.* A wave whose polarization is normal to the principal plane is called an *ordinary wave*, while light whose polarization is parallel to the principal plane is called an *extraordinary wave.* The refractive index of the o-wave does not depend on the propagation direction, but the refractive index of the e-beam is a function of the polar angle θ, and can be determined by the equation:

$$n_e(\theta) = n_o[(1 + \tan^2\theta)/(1 + (n_o/n_e)^2 \tan^2(\theta)]^{1/2} \tag{2.26}$$

If $n_o > n_e$ then the crystal is termed negative uniaxial; if $n_o < n_e$ then it is positive uniaxial.

(2) Biaxial crystal: In biaxial crystals, the dependence of refractive indices on the light propagation direction and its polarization corresponds to a much more complex surface than for uniaxial crystals.

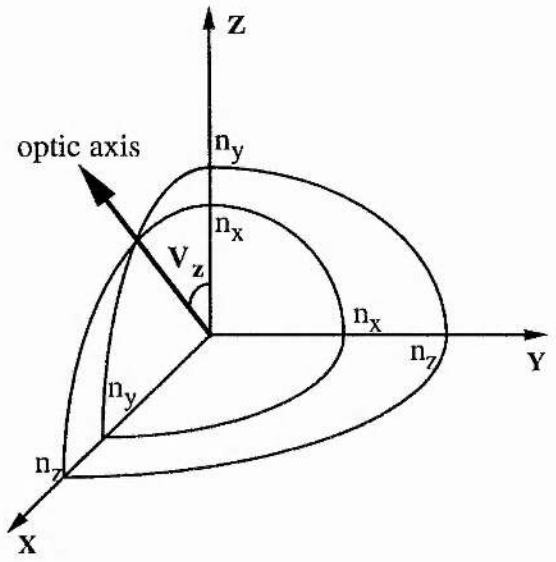

Figure 2.4: Indications of refractive indices in biaxial crystal.

If we restrict the principal refractive indices to the order of $n_x < n_y < n_z$, and only consider the case of light propagation in the principal planes $x-z$, $x-y$ and $y-z$, then the optic axes, whose directions are given by the intersection points of the ellipse and circle in the index ellipsoid (see Fig. 2.4), will always be in the plane $x-z$. The optic axis angle V_z, formed by one of the optic axes with the z axis can be found from the expression:

$$\sin V_z = \frac{n_z}{n_y}\left(\frac{n_y^2 - n_x^2}{n_z^2 - n_x^2}\right)^{1/2} \tag{2.27}$$

In the $x-y$ plane, the refractive index of the wave polarized normally to this plane is constant and equals n_z, and that of the wave polarized in this plane changes from n_y to n_x with ϕ varying from 0^o to 90^o. Hence, a biaxial crystal in the plane $x-y$ is similar to a negative uniaxial crystal with $n_o = n_z$ and

$$n_e(\phi) = n_y[(1+\tan^2\phi)/(1+(n_y/n_x)^2\tan^2(\phi)]^{1/2} \tag{2.28}$$

In the $y-z$ plane, the refractive index of the wave polarized normally to this plane is constant and equals n_x, and that of the wave polarized in this plane changes from n_y to

n_z with θ varying from 0^o to 90^o. Hence, a biaxial crystal in the plane $y-z$ is similar to a positive uniaxial crystal with $n_o = n_x$ and

$$n_e(\theta) = n_y[(1+\tan^2\theta)/(1+(n_y/n_z)^2\tan^2(\theta)]^{1/2} \tag{2.29}$$

Similarly in the $x-z$ plane, it is that $n_o = n_y$; and

$$n_e(\theta) = [\frac{\sin^2\theta}{n_z^2} + \frac{\cos^2\theta}{n_x^2}]^{-1/2} \tag{2.30}$$

However, at $\theta > V_z$, it is similar to a positive uniaxial crystal, *i.e.* $n_o < n_e(\theta)$; and at $\theta < V_z$, it is similar to a negative uniaxial crystal, *i.e.* $n_o > n_e(\theta)$.

(3) Double refraction: In an anisotropic medium, the energy of an extraordinary wave propagates at an angle α from its wave propagation direction **k**, where α is named the double-refraction angle. The energy propagating direction vector **s** can be shown to be the normal to the tangent drawn at the point of intersection of the wave vector **k** with the $n(\theta)$ curve [5]. The relationship between vectors **k** and **s** for both negative and positive uniaxial crystals are shown in Figure 2.5.

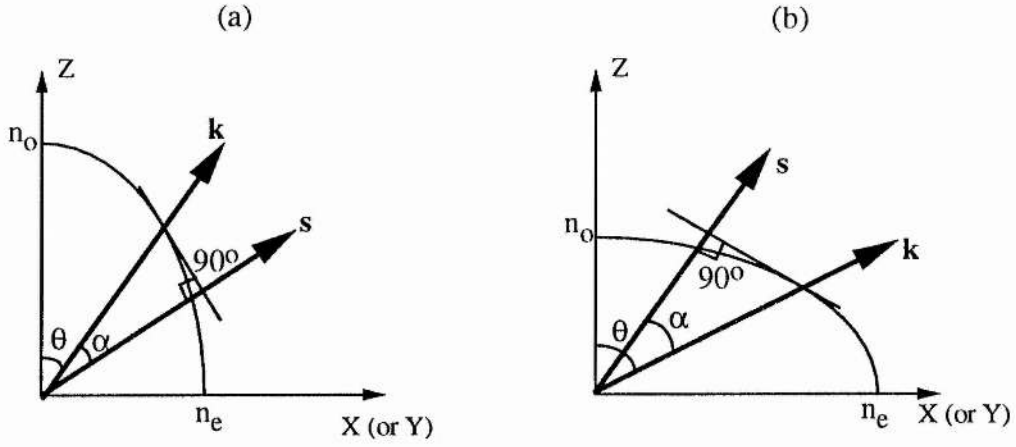

Figure 2.5: Displacement of the wave vector **k** and beam vector **s** in anisotropic negative (a) and positive (b) uniaxial crystals.

The double-refraction angle in the case of uniaxial crystals is straight forward to derive as has been shown in Ref.[5] and is given by:

$$\alpha(\theta) = \pm\arctan[(n_o/n_e)^2\cdot\tan\theta] \mp \theta$$

where the upper signs refer to a negative crystal and the lower signs to a positive crystal.

For biaxial crystals, the calculation of the double-refraction angle is more complicated. If we use **D** to represent the electric displacement and **H** to represent the magnetic field, then Maxwell's equations imply that for a plane wave **D**, **E** and **k** are orthogonal to the magnetic field **H**. Therefore **D**, **E** and **k** must be coplanar [4]. The Poynting vector **S**=**E**∧**H**, means that the direction of the energy flow lies in the same plane as **D**, **E** and **k**, but is not parallel to **k**. Figure 2.6 shows the relative directions of these vectors, from which it can be seen that the angle between **D** and **E** is equal to α. Hence we have

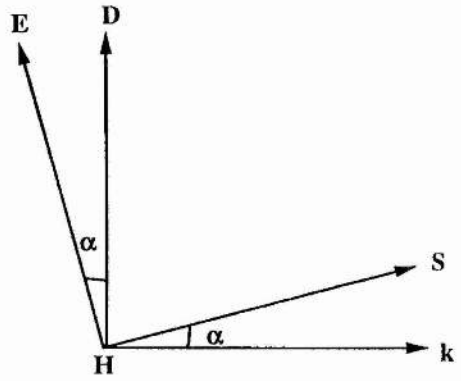

Figure 2.6: Relationship between the wave propagation direction **k** and the Poynting vector **S**, and between the electric field **E** and electric displacement vector **D**, in an anisotropic medium.

$$\sin\alpha = \mathbf{e} \bullet \mathbf{k}$$

and

$$\cos\alpha = \mathbf{e} \bullet \mathbf{d}$$

where **e** and **d** are the unit vectors denoting the directions of **E** and **D**. As has been shown in Ref.[6], with a few steps of derivation, the double-refractive angle for a biaxial crystal is given by

$$\tan\alpha = \frac{\mathbf{e} \bullet \mathbf{k}}{\mathbf{e} \bullet \mathbf{d}} = n^2 \left[\left(\frac{k_x}{n^{-2} - n_x^{-2}} \right)^2 + \left(\frac{k_y}{n^{-2} - n_y^{-2}} \right)^2 + \left(\frac{k_z}{n^{-2} - n_z^{-2}} \right)^2 \right]^{-\frac{1}{2}} \qquad (2.31)$$

For a three wave interaction, the walk-off angle is defined as the maximum angle of Poynting vector walk-off associated with the three waves.

Normally, the crystal used for a nonlinear optical device is either a uniaxial crystal or a biaxial crystal oriented for propagation in a principal plane. In such a case, there will be at least one ordinary wave, while all the extraordinary waves are polarized in a plane

which is orthogonal to the polarization direction of the ordinary wave. From Eq.(2.31), it can be seen that if two eigen-waves at frequencies ω_1 and ω_2 have the same polarization direction, then the high frequency eigen-wave has a larger double-refraction angle α than the low frequency eigen-wave. Therefore, the walk-off angle is the double-refraction angle of the extraordinary eigen-wave with the highest frequency.

2.2 Wave equations for propagation in nonlinear media

The equations governing the propagation of electromagnetic fields in a nonlinear medium are derived from Maxwell's wave equations describing a non-dielectric medium condition, That is:

$$\bigtriangledown^2 \mathbf{E} = \mu\sigma\frac{\delta \mathbf{E}}{\delta t} + \mu\varepsilon\frac{\delta^2 \mathbf{E}}{\delta t^2} + \mu\frac{\delta^2 \mathbf{P}_{NL}}{\delta t^2} \tag{2.32}$$

where $\varepsilon = \varepsilon_0(1+\chi^{(1)})$, ε and μ are the electric and magnetic permeabilities, and σ is the coefficient of absorption. Assuming that the higher-order terms than $\chi^{(2)}$ in Eq.(2.2) can be neglected, then Eq.(2.32) is the most general form of description for a wave propagating in a nonlinear medium with quadratic nonlinearity. The first term on the right hand side allows for absorption, while the other two are the source terms for wave propagation. Since an analytic solution for a Gaussian beam is impossible, the plane-wave approximation has been used all the time to analytically solve the wave equations.

2.2.1 The coupled wave equations for plane waves

Considering a total field $\mathbf{E}$, made up of three plane waves propagating in the z direction with frequencies ω_1, ω_2 and ω_3 and according to

$$\begin{aligned}
\mathbf{E}_1(z,t) &= \tfrac{1}{2}\left[E_1(z)e^{i(\omega_1 t - k_1 z)} + c.c\right] \\
\mathbf{E}_2(z,t) &= \tfrac{1}{2}\left[E_2(z)e^{i(\omega_2 t - k_2 z)} + c.c\right] \\
\mathbf{E}_3(z,t) &= \tfrac{1}{2}\left[E_3(z)e^{i(\omega_3 t - k_3 z)} + c.c\right]
\end{aligned} \tag{2.33}$$

then the total instantaneous field is

$$\mathbf{E} = \frac{1}{2}[\mathbf{E}_1(z)e^{(ik_1 z-\omega_1 t)} + c.c.] + \frac{1}{2}[\mathbf{E}_2(z)e^{(ik_2 z-\omega_2 t)} + c.c.] + \frac{1}{2}[\mathbf{E}_3(z)e^{(ik_3 z-\omega_3 t)} + c.c.] \tag{2.34}$$

For the case of $\omega_3 = \omega_1 + \omega_2$, then by applying a slow variation over distances comparable to a wavelength, (i.e. $k\frac{\delta E}{\delta z} \gg \frac{\delta^2 E}{\delta z^2}$), one obtains, after rearranging the resulting terms into their frequency components, a set of coupled equations describing the nonlinear parametric interaction between the three plane waves. These are

$$\frac{dE_1}{dz} = -\frac{1}{2}\frac{\mu_0\sigma_1 c}{n_1}E_1 - \frac{i\omega_1}{\cos^2\alpha_1}\frac{d_{eff}}{cn_1}E_3E_2^*e^{-i\Delta kz}$$

$$\frac{dE_2^*}{dz} = -\frac{1}{2}\frac{\mu_0\sigma_2 c}{n_2}E_2^* + \frac{i\omega_2}{\cos^2\alpha_2}\frac{d_{eff}}{cn_2}E_1E_3^*e^{i\Delta kz} \tag{2.35}$$

$$\frac{dE_3}{dz} = -\frac{1}{2}\frac{\mu_0\sigma_3 c}{n_3}E_3 - \frac{i\omega_3}{\cos^2\alpha_3}\frac{d_{eff}}{cn_3}E_1E_2e^{i\Delta kz}$$

where $\Delta k = k_3 - k_2 - k_1$ is the momentum-mismatch and α_i ($i = 1, 2$, and 3) denotes the Poynting vector double-refraction angle at the three fields (see Ref.[7] and Ref.[8]).We have used the convention of Eq.(2.24) to set the unit of d_{eff} to be pm/V, and the equations have been simplified by applying the relationship of $\sqrt{\frac{\mu_0\varepsilon_0^2}{\varepsilon_i}} = \frac{1}{cn_i}$, $i = 1, 2$, and 3. It can be readily seen that the three differential equations are coupled to each other via the nonlinear coefficient d_{eff}.

With the relation $E_i = \rho_i e^{-j\phi_i}$, we can further convert the coupled wave equations (2.35) into polar dependent variables, which are

$$\frac{\delta\rho_1}{\delta r} = -\frac{1}{2}\frac{\mu_0\sigma_1 c}{n_1}\rho_1 - \frac{\omega_1 d_{eff}}{n_1 c\cos^2\alpha_1}\rho_2\rho_3\sin\theta$$

$$\frac{\delta\rho_2}{\delta r} = -\frac{1}{2}\frac{\mu_0\sigma_2 c}{n_2}\rho_2 - \frac{\omega_2 d_{eff}}{n_2 c\cos^2\alpha_2}\rho_1\rho_3\sin\theta$$

$$\frac{\delta\rho_3}{\delta r} = -\frac{1}{2}\frac{\mu_0\sigma_3 c}{n_3}\rho_3 - \frac{\omega_3 d_{eff}}{n_3 c\cos^2\alpha_3}\rho_1\rho_2\sin\theta \tag{2.36}$$

$$\frac{\delta\theta}{\delta r} = \Delta k + \frac{d_{eff}}{c}\left(\frac{\omega_3}{n_3\cos^2\alpha_3}\frac{\rho_1\rho_2}{\rho_3}\right.$$

$$\left. - \frac{\omega_2}{n_2\cos^2\alpha_2}\frac{\rho_1\rho_3}{\rho_2} - \frac{\omega_1}{n_1\cos^2\alpha_1}\frac{\rho_2\rho_3}{\rho_1}\right)\cos\theta$$

where $\theta = \Delta kr + \phi_3(r) - \phi_2(r) - \phi_1(r)$.

Analytical solutions can be achieved for both undepleted and depleted plane wave inputs, but this may require some further approximations to be made with regard to absorption, walk-off and phase mismatching. Also, it must be borne in mind that to obtain more accurate results, the plane wave results should be averaged over the transverse distribution of the input beam [9].

The small signal solution

Using the small signal approximation, where the amplitude of the input wave is assumed to be constant, the analytic solutions of Eq.(2.35) have been widely introduced in text books, such as references [2] and [10]. Although the result is not valid for cases where the conversion efficiency is high, it is useful in the understanding of essential features of three beam interactions and for determining system gain and oscillation threshold of OPOs. Therefore, in this section we list some small signal solutions for the cases of sum-frequency generation, parametric amplification and parametric oscillation, these being the most relevant to this work.

(1) Small signal solution for sum-frequency generation: For the interaction $\omega_3 = \omega_2 + \omega_1$, and where the assumptions have been made of negligible absorption, $\sigma_1 = \sigma_2 = \sigma_3 = 0$, and $E^{\omega_3}(0) = 0$, by integrating Eq.(2.35) the output field, $E^{\omega_3}(L)$ is found to be

$$E^{(\omega_3)}(L) = -\frac{i\omega_3}{\cos^2\alpha_3}\frac{d_{eff}}{cn_3}E^{(\omega_1)}E^{(\omega_2)}\frac{e^{i\Delta kL}-1}{i\Delta k} \tag{2.37}$$

and the output intensity is

$$I^{\omega_3} \equiv \frac{P^{\omega_3}}{A} = \frac{1}{2}\sqrt{\frac{\varepsilon_3}{\mu_0}}|E^{\omega_3}|^2$$

$$= \frac{1}{4}\sqrt{\frac{\varepsilon_3}{\mu_0}}\left(\frac{\omega_3 d_{eff}L}{cn_3\cos^2\alpha_3}\right)^2 E_1^2E_2^2\frac{\sin^2(\Delta kL/2)}{(\Delta kL/2)^2}$$

$$= \frac{1}{\varepsilon_0}\frac{1}{c^3n_1n_2n_3}\left(\frac{\omega_3 d_{eff}L}{\cos^2\alpha_3}\right)^2 I_1I_2\frac{\sin^2(\Delta kL/2)}{(\Delta kL/2)^2} \tag{2.38}$$

It can be seen then from the above equation (2.38) that

$$I^{\omega_3} \propto \frac{\sin^2(\Delta kL/2)}{(\Delta kL/2)^2}$$

and the effect of phase mismatch is included entirely in the factor of

$$\frac{\sin^2(\Delta kL/2)}{(\Delta kL/2)^2} \tag{2.39}$$

As shown in Fig. 2.7, when Δk=0, then $\frac{\sin^2(\Delta kL/2)}{(\Delta kL/2)^2}$ is equal to 1, and I^{ω_3}, consequently, reaches its maximum; when $\Delta kL/2$=π, then $\frac{\sin^2(\Delta kL/2)}{(\Delta kL/2)^2}$=0 and therefore, I^{ω_3}=0. Hence, the various phase-match acceptance parameters, such as angular and temperature acceptance, are often defined by the factor of $\Delta kL/2 = \pi$, as it will be discussed in later sections of this chapter.

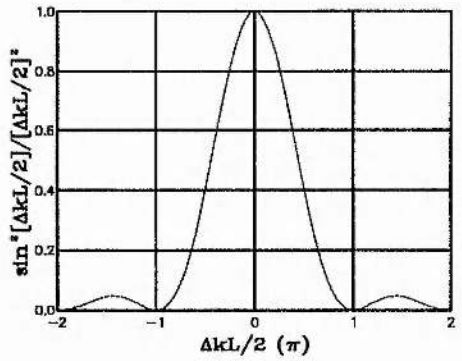

Figure 2.7: The effect of phase mismatch

(2) Small signal solution for parametric amplification and oscillation: With the frequency relationship of $\omega_p = \omega_s + \omega_i$ and assuming a constant pump field amplitude, and $\alpha_p = \alpha_s = \alpha_i = 0$, $\sigma_p = \sigma_s = \sigma_i = 0$, then the three coupled equations are reduced to two simultaneous differential equations (*signal* and *idler* terms), which are

$$E_s(z) = E_s(0)[\cosh(gz) - i\frac{\Delta k}{2g}\sinh(gz)] - i\frac{1}{g}K_s E_p(0)E_i^*(0)\sinh(gz)e^{i\frac{\Delta k}{2}z} \tag{2.40}$$

$$E_i(z) = E_i(0)[\cosh(gz) - i\frac{\Delta k}{2g}\sinh(gz)] - i\frac{1}{g}K_i E_p(0)E_s^*(0)\sinh(gz)e^{i\frac{\Delta k}{2}z} \tag{2.41}$$

where

$$g = \sqrt{\gamma_0^2 - (\frac{\Delta k}{2})^2} \tag{2.42}$$

$$\gamma_0^2 = K_i^* K_s E_p^*(z) E_p(z) \tag{2.43}$$

$$\begin{aligned} K_i &= \sqrt{\frac{\mu_0}{\varepsilon_i}}\omega_i d_{eff} \\ K_s &= \sqrt{\frac{\mu_0}{\varepsilon_s}}\omega_s d_{eff} \\ K_p &= \sqrt{\frac{\mu_0}{\varepsilon_p}}\omega_p d_{eff} \end{aligned} \tag{2.44}$$

The solution for depleted input

In the regime of depleted input, the plane-wave theory of the three-wave interaction without absorption was first formulated by Armstrong *et al.* [7] in 1962, who obtained explicit solutions for photon fluxes in terms of the *Jacobian* elliptical sine function, *sn*. Based on the original work, Baumgartiner and Byer [8] reviewed and extended the coupled wave equations for parametric amplification. In the work described here, the theoretical models for the calculation of conversion efficiency for SFG and OPOs are based on the exact analytic solution given in Ref.[8].

Numerical methods also play an important role in solving problems for the depleted case. With the great availability of computational power, solving numerically the coupled wave equations has become a practical alternative to deriving analytical solutions. It has the significant advantage of allowing one to include in the modelling more physical effects, such as absorption and phase mismatching, and therefore can give more accurate results than the analytic solution.

In this section, a description is given of both methods.

(1) Exact solution Using the polar forms of the coupled wave equations, Eq.(2.36), and assuming zero absorption for the three waves, then we have

$$\frac{\delta\rho_1}{\delta r} = -\frac{\omega_1 d_{eff}}{n_1 c \cos^2\alpha_1}\rho_2\rho_3 \sin\theta$$

$$\frac{\delta\rho_2}{\delta r} = -\frac{\omega_2 d_{eff}}{n_2 c \cos^2\alpha_2}\rho_1\rho_3 \sin\theta$$

$$\frac{\delta\rho_3}{\delta r} = -\frac{\omega_3 d_{eff}}{n_3 c \cos^2\alpha_3}\rho_1\rho_2 \sin\theta \tag{2.45}$$

$$\frac{\delta\theta}{\delta r} = \Delta k + \frac{d_{eff}}{c}\left(\frac{\omega_3}{n_3\cos^2\alpha_3}\frac{\rho_1\rho_2}{\rho_3}\right.$$

$$\left.-\frac{\omega_2}{n_2\cos^2\alpha_2}\frac{\rho_1\rho_3}{\rho_2} - \frac{\omega_1}{n_1\cos^2\alpha_1}\frac{\rho_2\rho_3}{\rho_1}\right)\cos\theta$$

where $\theta = \Delta k r + \phi_3(r) - \phi_2(r) - \phi_1(r)$.

An invariant for the parametric conversion process representing the power flow per unit area parallel to the direction of propagation is

$$W = \frac{\varepsilon_0 c}{2}\left(n_1\rho_1\cos^2\alpha_1 + n_2\rho_2\cos^2\alpha_2 + n_3\rho_3\cos^2\alpha_3\right) \tag{2.46}$$

or

$$W = \mathbf{I}_1(0)\cos^2\alpha_1 + \mathbf{I}_2(0)\cos^2\alpha_2 + \mathbf{I}_3(0)\cos^2\alpha_3$$

Introducing the normalised dependent and independent variables given by

$$u_i = \left(\frac{\varepsilon_0\lambda_i n_i}{4\pi W}\cos^2\alpha_i\right)^{1/2}\rho_i = \left[\frac{\mathbf{I}_i\cos^2\alpha_i}{\omega_i W}\right]^{1/2} \tag{2.47}$$

where $i = 1, 2$, and 3, and

$$\xi = \frac{4 d_{eff}\pi(\pi W)^{1/2} r}{(\varepsilon_0\lambda_1\lambda_2\lambda_3 n_1 n_2 n_3\cos^2\alpha_1\cos^2\alpha_2\cos^2\alpha_3)^{1/2}} \tag{2.48}$$

the resulting set of normalized coupled equation from Eq.(2.45) is

$$\frac{\delta u_1}{\delta\xi} = -u_2 u_3 \sin\theta \tag{2.49}$$

$$\frac{\delta u_2}{\delta\xi} = -u_1 u_3 \sin\theta \tag{2.50}$$

$$\frac{\delta u_3}{\delta\xi} = u_1 u_2 \sin\theta \tag{2.51}$$

$$\frac{\delta\theta}{\delta\xi} = \Delta S + \left(\frac{u_1 u_2}{u_3} - \frac{u_2 u_3}{u_1} - \frac{u_1 u_3}{u_2}\right)\cos\theta \tag{2.52}$$

where $\Delta S = \Delta kr/\xi$. The phase equation Eq.(2.52) can be integrated with a substitution from Eq.(2.51) to give

$$\cos\theta = \left(\Gamma - \frac{1}{2}\Delta S u_3^2(0)\right) \tag{2.53}$$

and

$$\Gamma = u_1(0)u_2(0)u_3(0)\cos\theta(0) + \frac{1}{2}\Delta S u_3^2(0) \tag{2.54}$$

where Γ is a constant of integration. The solution to the normalized coupled equations is based on integrating Eq.(2.51) and after substituting of the integration constant and the Manley-Rowe relations, the resultant integral is

$$\xi = \pm\frac{1}{2}\int_{u_3^2(0)}^{u_3^2(\xi)} \frac{d\left(u_3^2\right)}{\left[u_3^2\left(m_2 - u_3^2\right)\left(m_1 - u_3^2\right) - \left(\Gamma - \frac{1}{2}\Delta S u_3^2\right)^2\right]^{1/2}} \tag{2.55}$$

where $m_1 = u_1^2 + u_2^2$, $m_2 = u_2^2 + u_3^2$, and $m_3 = u_1^2 - u_2^2$, are the Manley-Rowe [11] relations. The cubic polynomial in the denominator radical suggests the use of elliptic integrals as solutions. The three roots of the denominator polynomial are placed in the order of $u_{3c}^2 \geq u_{3b}^2 \geq u_3^2 \geq 0$. Two algebraic substitutions

$$y^2 = \frac{\left(u_3^2 - u_{3a}^2\right)}{\left(u_{3b}^2 - u_{3a}^2\right)} \tag{2.56}$$

and

$$\gamma^2 = \frac{\left(u_{3b}^2 - u_{3a}^2\right)}{\left(u_{3c}^2 - u_{3a}^2\right)} \tag{2.57}$$

then convert the integral expression into the standard elliptic integrals [12]

$$\xi = \pm\frac{1}{\left(u_{3c}^2 - u_{3a}^2\right)^{\frac{1}{2}}}\int_{y(0)}^{y(\xi)} \frac{dy}{\left[\left(1 - y^2\right) - \left(1 - \gamma^2 y^2\right)\right]^{1/2}} \tag{2.58}$$

The inverse operation of the elliptic integral is a *Jacobian* elliptic function. The general solution for the normalized u values is

$$u_3^2(\xi) = u_{3a}^2 + \left(u_{3b}^2 - u_{3a}^2\right) sn^2\left[\left(u_{3c}^2 - u_{3a}^2\right)^{\frac{1}{2}}(\xi + \xi_0), \gamma\right] \tag{2.59}$$

$$u_2^2(\xi) = u_2^2(0) + u_3^2(0) - u_3^2(\xi) \tag{2.60}$$

$$u_1^2(\xi) = u_1^2(0) + u_3^2(0) - u_3^2(\xi) \tag{2.61}$$

where

$$\xi_0 = \mathbf{F}(\sin^{-1}[Y(0)], \gamma)(u_{3c}^2 - u_{3a}^2)^{\frac{1}{2}}$$

and $\mathbf{F}(\phi, r)$ is a standard elliptic integral.

Numerical solutions of the above equations (2.59), (2.60) and (2.61), can be obtained for particular nonlinear frequency conversion devices with given parameters, as will be discussed in the following sections of this chapter.

(2) Numerical solution In cases where absorption may be considerable and it is unacceptable to neglect the phase mismatch to be zero, then it seems inevitable that numerical methods must be used to allow the inclusion of all those relevant effects.

The coupled wave equations (2.36) is a stand alone system of four first-order ordinary differential equations at the form

$$\rho_i' = f_i(r, \rho_1, \rho_2, \rho_3, \theta) \qquad (i = 1, 2, 3)$$

and

$$\theta' = g(r, \rho_1, \rho_2, \rho_3, \theta)$$

In numerical work we can only obtain a particular solution, and this will consist of a table giving the values of ρ_i and θ along side the corresponding values of r. Thus in the case of the first-order differential equations, we need to specify not only the differential equation itself, but also the initial conditions

$$\rho_i(r_0) = \rho_{i0} \qquad (i = 1, 2, \text{and } 3)$$

and

$$\theta(r_0) = \theta_0$$

Subject to certain mathematical conditions, there is a unique solution for each equation in Eq.(2.36) which passes through the initial condition, (r_0, ρ_{i0}, θ_0).

The most commonly used method in solving such problems is Runge-Kutta methods. A book written by Scraton [13] gives a general introduction to the use of the Runge-Kutta method to numerically solve Eq.(2.36). Currently the solving process can be implemented on computer by using available software such as Mathcad in PC and NAG Fortran Library Routines in Unix.

A typical example of this work can be seen in Ref.[14], in which, with the use of a new modified Runge-Kutta method, Bakker *et al.*, presented a numerical method for the description of optical frequency conversion between three short-pulsed fields and including the effects of phase mismatch, group-velocity differences, and depletion of the electromagnetic fields. Some other examples of using this method can be seen in Ref.[15] given by Breteau *et al.*, and Ref.[16], given by Bowers *et al.* All of these studies have shown clearly that the numerical method is powerful to use, and in particular in modelling the performance of singly-resonated OPOs with Q-switched pump lasers.

2.2.2 Nonlinear optical interactions with focused Gaussian beams

In practice, a tightly focused Gaussian beam is often used to increase its intensity and hence the efficiency of the nonlinear optical process.

Previously, Boyd and Kleinman [3] have considered how to adjust the focus of the incident laser beam in order to optimise the efficiency of the second-harmonic generation process. They find that the highest efficiency is obtained when beam walk-off effects are negligible, when the incident laser beam is focused so that the beam waist is located at the centre of the crystal, the ratio L/b (where L is crystal length, $b \equiv 2\pi w_0^2/\lambda$, is confocal parameter) is equal to 2.84, and when the wave vector mismatch is set equal to $\Delta k = 3.2/L$. In this case, the power generated at the second-harmonic frequency is equal to

$$p_{2\omega} = 1.068 \left[\frac{128\pi^2 \omega_1^3 d^2 L}{c^4 n_1 n_2} \right] p_\omega^2$$

In addition, Boyd and Kleinman [3] show heuristically that other parametric processes, such as sum- and difference-frequency generation, are optimised by choosing the same confocal parameter for both input waves and applying the same criteria used to optimise second-harmonic generation.

In recent years, as computational technique and software have progressed dramatically, the processes of nonlinear optical interactions with focused Gaussian beams have tended to be modelled numerically, as has been reported in Refs. [16], [17], and [18]. In particular, Smith *et al.* have developed a set of very useful models for sum- and difference-frequency generation [17], and for a seeded nanosecond optical parametric oscillator [16].

The key to successfully implementing numerical modelling for a nonlinear process with consideration being taken of Gaussian beams is in the integration of the three waves

through the mixing crystal by using Fourier-transform techniques. When non-uniform transverse profiles are considered, the coupled wave equation (2.35) should be replaced by the form

$$\frac{\delta\varepsilon_j(x,y,z,t)}{\delta z} = \frac{i}{2k_j}\left[\frac{\delta^2\varepsilon_j(x,y,z,t)}{\delta y^2} + \frac{\delta^2\varepsilon_j(x,y,z,t)}{\delta x^2}\right] - \tan\alpha\frac{\delta\varepsilon_j(x,y,z,t)}{\delta x}$$

$$+ P_j(x,y,z,t) - \sigma_j\varepsilon_j(x,y,z,t) \tag{2.62}$$

where j is the frequency index, α is the walk-off angle in the x direction, and σ is the linear loss in the crystal.

The complex variable ε_j is a Fourier component of the optical electric field E_j, defined by

$$E_j = \frac{1}{2}\left\{\varepsilon_j \exp\left[-i(\omega_j t - k_j z\right] + \varepsilon_j^* \exp\left[i(\omega_j t - k_j z\right]\right\} \tag{2.63}$$

P_j is the polarization term at frequency ω_j and is given by

$$\begin{aligned}
P_1(x,y,z,t) &= i\frac{d_{eff}}{c}\frac{\omega_1}{n_1}\varepsilon_3(x,y,z,t)\varepsilon_2^*(x,y,z,t)\exp(i\Delta kz)\\
P_2(x,y,z,t) &= i\frac{d_{eff}}{c}\frac{\omega_2}{n_2}\varepsilon_3(x,y,z,t)\varepsilon_1^*(x,y,z,t)\exp(i\Delta kz)\\
P_3(x,y,z,t) &= i\frac{d_{eff}}{c}\frac{\omega_3}{n_3}\varepsilon_1(x,y,z,t)\varepsilon_2(x,y,z,t)\exp(-i\Delta kz)
\end{aligned} \tag{2.64}$$

Fourier transforming the electric fields and polarizations in the transverse dimension, using

$$\varepsilon_j(x,y,z,t) = \int_{-x}^{x}\int_{-x}^{x}\varepsilon_j(s_x,s_y,z,t)\exp\left[i2\pi\left(s_x x + s_y y\right)\right]ds_x ds_y \tag{2.65}$$

$$P_j(x,y,z,t) = \int_{-x}^{x}\int_{-x}^{x}P_j(s_x,s_y,z,t)\exp\left[i2\pi\left(s_x x + s_y y\right)\right]ds_x ds_y \tag{2.66}$$

and substituting these definitions of $\varepsilon_j(x,y,z,t)$ and $P_j(x,y,z,t)$ into Eq.(2.62), the equation for the individual spatial frequency component waves propagation can be found:

$$\frac{\delta\varepsilon_j(s_x,s_y,z,t)}{\delta z} = -i\left[\frac{2\pi^2(s_x^2+s_y^2)}{k_j} + 2\pi s_y\tan\alpha\right]\varepsilon_j(s_x,s_y,z,t) + P_j(s_x,s_y,z,t) \tag{2.67}$$

This procedure results in three coupled first-order ordinary differential equations for the change in each spatial frequency component of the fields as they propagate through the crystal. The equations are coupled through the nonlinear interaction term $P_j(s_x,s_y,z,t)$. Based on the above, a time dependent model of three wave mixing was then developed by Smith *et al.* [17], in which, a frequency mixing process can be modelled for each

time step by propagating half of a z step, using a Runge-Kutte algorithm to numerically integrate the coupled ordinary differential equations. One then applies a fast-Fourier-transform algorithm to transform the resulting spatial-frequency fields $\varepsilon_j(s_x, s_y, z, t)$ into fields $\varepsilon_j(x, y, z, t)$ in $x - y$ space. $P_j(x, y, z, t)$ can then be found by inserting these fields into Eq.(2.67). One then applies the fast-Fourier transform algorithm again to obtain the $P_j(s_x, s_y, z, t)$'s, which are used in Eq.(2.67) to propagate the second half of the z step. As has been described in Refs.[16] and [17], this method can provide modelling results for the three waves fluences in the spatial and temporal domains.

2.3 Phase-matching and acceptance parameters

From the small signal solution of the coupled wave equations as discussed in the previous section, we know that the prerequisite for an efficient three wave interaction is:

$$\Delta k = 0 \tag{2.68}$$

which is called the phase-matching condition. For collinear phase-matching, this means

$$n^{\omega_3}\omega_3 = n^{\omega_2}\omega_2 + n^{\omega_1}\omega_1 \tag{2.69}$$

where $\omega_3 = \omega_2 + \omega_1$. In a normally dispersive crystal, the index of refraction n increases with ω, thus Eq.(2.69) is impossible to achieve when all the three waves are ordinary or extraordinary waves. The phase-matching condition only can be satisfied when there is, at least, one extraordinary wave and one ordinary wave. If we use n_a and n_b to express the two eigen refractive indices for a wave vector at a given propagation direction, and let $n_a < n_b$, $\omega_3 > \omega_2 \geq \omega_1$, then there are three possible phase-matching geometries which are as follows:

$$n_a^{\omega_3} \bullet \omega_3 = n_b^{\omega_2} \bullet \omega_2 + n_b^{\omega_1} \bullet \omega_1 \qquad (typeI) \tag{2.70}$$

$$n_a^{\omega_3} \bullet \omega_3 = n_b^{\omega_2} \bullet \omega_2 + n_a^{\omega_1} \bullet \omega_1 \qquad (typeII) \tag{2.71}$$

$$n_a^{\omega_3} \bullet \omega_3 = n_a^{\omega_2} \bullet \omega_2 + n_b^{\omega_1} \bullet \omega_1 \qquad (typeIII) \tag{2.72}$$

All three phase-matching geometries can be achieved either by angular tuning or temperature tuning of the crystal.

2.3.1 Angle phase-matching

When a wave with a wave-vector **k** propagates through an anisotropic medium, its refractive index must obey the Fresnel equation:

$$\frac{k_x^2}{n^2 - n_x^2} + \frac{k_y^2}{n^2 - n_y^2} + \frac{k_z^2}{n^2 - n_z^2} = \frac{1}{n^2} \tag{2.73}$$

For a uniaxial crystal, where $n_x = n_y = n_o$, and $n_z = n_e$; the two eigen solutions of refractive index are

$$\begin{aligned} n' &= n_o \\ n'' &= n_e(\theta) = n_o n_e \left[n_o^2 \sin^2\theta + n_e^2 \cos^2\theta\right]^{-\frac{1}{2}} \end{aligned} \tag{2.74}$$

The eigen wave experiencing refractive index n_o is in response to the ordinary polarization, and the other eigen wave experiencing refractive index $n_e(\theta)$ is in response to the extraordinary polarization. Angle phase-matching can be achieved by altering the phase-matching angle, θ. For example, the eigen refractive indices for type II SHG in a negative uniaxial crystal ($n_e < n_o$) are: $n_a = n_e(\theta)$, and $n_b = n_o$; the phase-matching condition, Eq.(2.69) then becomes

$$n_e^{2\omega}(\theta) = [n_o^\omega + n_e^\omega(\theta)]/2$$

or

$$\frac{n_o^{2\omega} n_e^{2\omega}}{\sqrt{(n_o^{2\omega})^2 \sin^2\theta + (n_e^{2\omega})^2 \cos^2\theta}} = \frac{1}{2}\left[n_o^\omega + \frac{n_o^\omega n_e^\omega}{\sqrt{(n_o^\omega)^2 \sin^2\theta + (n_e^\omega)^2 \cos^2\theta}}\right] \tag{2.75}$$

For a biaxial crystal, where $n_x < n_y < n_z$, the two eigen refractive indices can be written in the well known forms [19]:

$$\begin{aligned} n_a &= \frac{\sqrt{2}}{\sqrt{-B+\sqrt{B^2-4C}}} \\ n_b &= \frac{\sqrt{2}}{\sqrt{-B-\sqrt{B^2-4C}}} \end{aligned} \tag{2.76}$$

where:

$$B = -\left[k_x^2\left(n_y^{-2} + n_z^{-2}\right) + k_y^2\left(n_x^{-2} + n_z^{-2}\right) + k_z^2\left(n_x^{-2} + n_y^{-2}\right)\right]$$

$$C = [k_x/(n_y n_z)]^2 + [k_y/(n_x n_z)]^2 + [k_z/(n_x n_y)]^2$$

As it has been mentioned previously, normally only the three principal planes of a crystal are used for phase-matching. In such a case, one eigen refractive index must be equal to a principal refractive index, this is similar to the case of using a uniaxial crystal, but the other eigen refractive index is a function of both angles θ and ϕ. The angle phase-matching will be achieved by tuning θ or ϕ depending which principal plane is used. Again, as an example, for type II SHG in a biaxial crystal, the phase-matching angles θ and ϕ can be found out by replacing Eq.(2.82) into Eq.(2.71), when we have

$$\frac{\sqrt{2}}{\sqrt{-B^{2\omega}+\sqrt{(B^{2\omega})^2-4C^{2\omega}}}}=\frac{1}{2}\left[\frac{\sqrt{2}}{\sqrt{-B^{\omega}+\sqrt{(B^{\omega})^2-4C^{\omega}}}}+\frac{\sqrt{2}}{\sqrt{-B^{\omega}-\sqrt{(B^{\omega})^2-4C^{\omega}}}}\right] \tag{2.77}$$

Very often, the result from Eqs. (2.75) and (2.77) is a continuous phase-matching curve over a range of values of (θ_{pm}, ϕ_{pm}). Along the curve, the **optimum phase-match** is defined as the point at which the d-effective coefficient takes its maximum value.

2.3.2 Temperature phase-matching

There is a major drawback with angle tuning, namely the double refraction effect in the case where the wave propagation direction is not parallel to any principal axis. For some crystals, such as lithium niobate and lithium triborate, birefringence is strongly temperature-dependent. Therefore, it is possible to change the birefringence of those crystal by changing the temperature to achieve non-critical phase-matching condition, where d_{eff} goes to a maximum, and the walk-off angle is zero.

2.3.3 Acceptance parameters

In real cases, some factors, such as the laser beam divergence and disturbances in the temperature, will result in wave vector $\mathbf{k}$ deviating from the perfect phase-matching condition $(\theta_{pm}, \phi_{pm}, T_{pm})$ by amounts of $\Delta\theta$, $\Delta\phi$, and ΔT.

Since all the phase-matching parameters θ, ϕ, and T only vary by small amounts from θ_{pm}, ϕ_{pm}, and T_{pm}, the resulting phase mismatching, Δk, can be expanded as a Taylor series which is a function of these variations, *i.e.*

$$\Delta k = \Delta k\,|_{\xi=\xi_{PM}} + \frac{\delta\Delta k}{\delta\xi}\,|_{\xi=\xi_{PM}}\,\Delta\xi + \frac{1}{2}\frac{\delta^2\Delta k}{\delta\xi^2}\,|_{\xi=\xi_{PM}}\,(\Delta\xi)^2 + \cdots \tag{2.78}$$

where ξ expresses one or another of these phase-matching parameter, θ, ϕ, or T. The acceptance bandwidth of these parameters is dependent on the maximum allowed phase mismatching for effective nonlinear interaction. Normally, two definitions of phase-matching bandwidth have been used. In the first, it is defined as the full width at half maximum amplitude (FWHM) of the parametric interaction gain profile (see Fig. 2.6), so that the bandwidth of phase mismatching is determined from:

$$\frac{\Delta k L_c}{2} = arc\left[sinc^2(1/2)\right]. \tag{2.79}$$

In the second, it is defined as the first zero of the phase-matching range spanned, so that the bandwidth of phase mismatching is determined from:

$$\frac{\Delta k L_c}{2} = \pi. \tag{2.80}$$

We will use the latter definition. Substituting Eq.(2.80) into Eq.(2.78), we then have

$$\frac{\delta \Delta k}{\delta \xi} \mid_{\xi=\xi_{PM}} \Delta\xi + \frac{1}{2}\frac{\delta^2 \Delta k}{\delta \xi^2} \mid_{\xi=\xi_{PM}} (\Delta\xi)^2 \approx \pm\frac{2\pi}{L} \tag{2.81}$$

where $\Delta k \mid_{\xi=\xi_{PM}} = 0$. Hence the acceptance parameter, $\Delta\xi$, is derived to be

$$\Delta\xi = \frac{-\frac{\delta\Delta k}{\delta\xi} \pm \left[\left(\frac{\delta\Delta k}{\delta\xi}\right)^2 + 4\frac{\delta^2\Delta k}{\delta\xi^2}\frac{\pi}{L}\right]^{\frac{1}{2}}}{\frac{\delta^2\Delta k}{\delta\xi^2}} \tag{2.82}$$

Eq.(2.82) has been used through all of this thesis for acceptance parameters calculation.

Angle acceptance

For a wave vector specified at (θ_{pm}, ϕ_{pm}), there are two angular acceptance parameters $\Delta\theta$, and $\Delta\phi$. According to the commonly used definitions of phase-matching angles θ, and ϕ, it is easy to understand that $\Delta\theta$ is the angular acceptance which is defined in the $z-\mathrm{k}$ plane, and $\Delta\phi$ is the angular acceptance which is defined in the $x-y$ plane. Because the values for $\frac{\delta\Delta k}{\delta\theta}$ and $\frac{\delta\Delta k}{\delta\phi}$, $\frac{\delta^2\Delta k}{\delta\theta^2}$ and $\frac{\delta^2\Delta k}{\delta\phi^2}$ are usually quite different, so that one of $\Delta\theta$ or $\Delta\phi$ is often one much bigger than another. For instance, when k is in the $x-z$ plane and at a angle θ from z, it can easily be shown by calculation that $\Delta\theta \ll \Delta\phi$. A useful conclusion here is: the angular acceptance along the ordinary wave polarization direction is much larger than the angular acceptance along the extraordinary wave polarization direction.

Temperature acceptance

To simplify the calculation of temperature acceptance, we often take the first-order approximation of the equation (2.81), *e.g.*,

$$\Delta k = 2\pi \left[\frac{1}{\lambda_3} \frac{\delta n(\omega_3)}{\delta T} - \frac{1}{\lambda_2} \frac{\delta n(\omega_2)}{\delta T} - \frac{1}{\lambda_1} \frac{\delta n(\omega_1)}{\delta T} \right] \Delta T$$

and hence

$$(\Delta T)\, L_c = \left[\frac{1}{\lambda_3} \frac{\delta n(\omega_3)}{\delta T} - \frac{1}{\lambda_2} \frac{\delta n(\omega_2)}{\delta T} - \frac{1}{\lambda_1} \frac{\delta n(\omega_1)}{\delta T} \right]^{-1} \tag{2.83}$$

where the $\delta n(\omega_i)/\delta T$'s are often given in a form of polynomial.

However, as we know, tight focusing is often used for a nonlinear frequency conversion process. The beam divergence in such a case will result in an non-negligible amount of phase mismatching Δk, and hence the temperature acceptance is smaller than that determined from the Eq.(2.83).

2.4 Theory of singly-resonant OPO

As shown in Fig. 2.3 for a typical optical parametric oscillator, when a nonlinear crystal is placed within an optical resonator that provides resonance for the signal or idler waves (or both), the parametric gain will, at some threshold pumping intensity, cause simultaneous amplification at both the signal and idler frequencies. The threshold for this oscillation corresponds to the point at which the parametric gain just balances the losses of the signal and idler waves. This is the physical basis of the optical parametric oscillator.

Basically, there are two configurations that optical parametric oscillators take. In one, feedback is provided for both the signal and idler; this type is called the doubly-resonant oscillator (DRO). In the second one, feedback is provided for either the signal or idler but not both; this type of oscillator is called the singly-resonant oscillator (SRO). In our work, only the SRO is considered.

2.4.1 Gain and pump threshold

In any oscillator, some form of gain is required to overcome losses and produce oscillation. In a laser, gain is provided by population inversion between atomic or molecular levels. In a parametric oscillator, gain is produced by the interaction between electromagnetic

fields in a nonlinear medium, where a strong, high-frequency electromagnetic wave of frequency ω_p interacts via the nonlinear response of the medium with two lower-frequency electromagnetic waves of frequencies ω_s and ω_i ($\omega_s \geq \omega_i$) to produce amplification at these two lower frequencies. ω_p is called the pump frequency, ω_s the signal frequency, and ω_i the idler frequency. The three frequencies are connected by the relation, $\omega_p = \omega_s + \omega_i$.

Physically, the gain mechanism can be viewed as follows: the signal and pump fields mix via the nonlinear response of the medium to generate a polarization wave with frequency $\omega_i = \omega_p - \omega_s$, propagating as $\exp[i(k_p - k_s)z]$. This polarization wave in turn generates an electromagnetic field δE_i at the frequency ω_i. On a similar manner, this idler field then mixes with the pump field generate a polarization at $\omega_s = \omega_p - \omega_i$, which generates an incremental field δE_s. Provided that the fields are phased properly, the incremental signal and idler fields will add constructively to the existing fields, resulting in growth.

An effective radiation of signal field is achieved only when the round-trip gain experienced by the resonated wave exceeds the round-trip loss, this is the oscillation threshold condition.

Below threshold, and even without a resonator to provide feedback, there is spontaneously emitted radiation at the signal and idler. This radiation is variously referred to as spontaneous parametric emission, optical parametric noise, or parametric fluorescence. Viewed quantum-mechanically, this effect results from the spontaneous annihilation of a pump photon and the creation of a signal and idler photon. Spontaneous parametric emission is proportional to the parametric gain, and hence displays the $\sin^2(\Delta kL/2)/(\Delta kL/2)^2$ dependence. The peak of the spontaneous parametric emission occurs when $\Delta k = 0$.

Above threshold, the signal and idler fields build up and deplete the pump as it passes through the crystal. Saturation occurs when the pump intensity is reduced to the point where single-pass gain equals single-pass loss.

Pump threshold of single-pass-pumped SRO

We first consider the pump threshold for the case of single-pass-pump, which is the basic pump geometry for the optical parametric oscillator. The threshold calculation of this pump configuration will be discussed for both the cases of a plane wave and a focused Gaussian wave.

(1) Pump threshold for plane wave: From the small signal plane wave solutions Eq.(2.40) and Eq.(2.41) where the pump field is assumed to be constant, and the initial field of idler at $z = 0$ is

$$E_i(0) = 0$$

and according to the definition of parametric amplification gain as

$$G = \frac{I_s(L) - I_s(0)}{I_s(0)} \tag{2.84}$$

where

$$I_s(z) = \frac{1}{2}\sqrt{\frac{\varepsilon_s}{\mu_0}} E_s^*(z) E_s(z) \tag{2.85}$$

we have

$$G = (\frac{\gamma_0}{g})^2 \sinh^2(gL) \tag{2.86}$$

where γ_0, g have been defined in Eq.(2.42) and Eq.(2.43), *e.g.*,

$$g = \sqrt{\gamma_0^2 - (\frac{\Delta k}{2})^2} \tag{2.87}$$

$$\gamma_0^2 = K_i K_s E_p^*(z) E_p(z) \tag{2.88}$$

For the case of $(\Delta k L)^2 / 4 \gg (\gamma_0 L)^2$ and small $\gamma_0 L$, the gain is then

$$G \simeq (\gamma_0 L)^2 \frac{\sin^2(\Delta k L/2)}{(\Delta k L/2)^2} \tag{2.89}$$

Eq.(2.89) shows the same relation between gain and phase mismatch as appeared in Eq.(2.38) for the SFG analysis. If we let

$$\frac{dG}{d(\Delta k)} = 0 \tag{2.90}$$

then the maximum G is achieved at $\Delta k = 0$, and is

$$G_{max} = \sinh^2(\gamma_0 L) \tag{2.91}$$

For the case of $\gamma_0 L \ll 1$, we then have

$$G_{max} = \gamma_0^2 L^2 = 2(\frac{\mu_0}{\varepsilon_0})^{\frac{3}{2}} \frac{\omega_i \omega_s d_{eff}^2 L^2}{n_i n_s n_p} I_p(0) \tag{2.92}$$

This result shows that the small signal gain for parametric amplification is proportional to pump intensity, d_{eff}^2 and L^2. If we take $\Delta k = 0$, and assume that r_i and r_s are the

amplitude reflection coefficients for mirrors M_1 and M_2, then using (2.40) and (2.41), the threshold condition for resonance can be derived to be

$$r_s^2[E_s(0)\cosh(\gamma_0 z) - i\frac{1}{\gamma_0}K_s E_p(0)E_i^*(0)\sinh(\gamma_0 z)] = E_s(0) \tag{2.93}$$

$$r_i^2[E_i(0)\cosh(\gamma_0 z) - i\frac{1}{\gamma_0}K_i E_p(0)E_s^*(0)\sinh(\gamma_0 z)] = E_i(0) \tag{2.94}$$

Again, assuming $\gamma_0 L \ll 1$, we have

$$(\gamma_0 L)^2 = \frac{2(1-r_s^2)(1-r_i^2)}{r_s^2 + r_i^2} \tag{2.95}$$

For a doubly-resonant OPO (DRO), $r_s^2 \simeq 1$, and $r_i^2 \simeq 1$, hence we have

$$(\gamma_0 L)^2_{DRO} = (1-r_s^2)(1-r_i^2) \tag{2.96}$$

and according to (2.92), the threshold pump intensity for the DRO is

$$[I_p^{th}]_{DRO} = \frac{1}{2}(\frac{\mu_0}{\varepsilon_0})^{\frac{3}{2}}\frac{n_i n_s n_p}{\omega_i \omega_s d_{eff}^2 L^2}(1-r_s^2)(1-r_i^2) \tag{2.97}$$

For a singly-resonant OPO (SRO), $r_s^2 \simeq 1$, but $r_i^2 \simeq 0$, hence we have

$$(\gamma_0 L)^2_{SRO} = 2(1-r_s^2) \tag{2.98}$$

and the threshold of the SRO is then

$$[I_p^{th}]_{SRO} = (\frac{\mu_0}{\varepsilon_0})^{\frac{3}{2}}\frac{n_i n_s n_p}{\omega_i \omega_s d_{eff}^2 L^2}(1-r_s^2) \tag{2.99}$$

Eq.(2.99) straightforwardly shows the relation between pump threshold and the relevant parameters. Also, a comparison of Eq.(2.99) and Eq.(2.97) indicates that the pump threshold of singly-resonant OPOs is $2/(1-r_i^2)$ times higher than that of doubly-resonant OPOs.

The above plane wave consideration is only suitable for the case of loose focusing. However, tight focusing may often require to be used to reduce pump threshold and increase conversion efficiency.

(2) Pump threshold for focused Gaussian beam: The theory of optical parametric oscillator threshold for finite beams with Gaussian spatial dependence has been considered by a number of authors, these are Boyd and Kleinman [3], Bjorkholm [20], Brosnan and Byer [21], Fischer [22], and Guha [23].

In 1968, for a doubly-resonant parametric oscillator (DRO), Boyd and Kleinman [3] first studied the effects of beam focusing and double refraction. They defined the degree of beam focusing by a parameter ξ, given by

$$\xi = \frac{L_c}{b}$$

while the effect of beam walkoff due to double refraction is characterised by a parameter B, defined by

$$B = \frac{\alpha}{2}\sqrt{L_c k_o n_p / n_o}$$

where k_o and n_o are the wave propagation constant and refractive index at degeneracy, i.e. $\omega_s = \omega_i = \omega_o = \omega_p/2$, and α is the double refraction angle for the extraordinary pump wave. A parameter $h_m(\xi, B)$ then was introduced as a dimensionless quantity dependent on the double refraction parameter B and the degree of focusing characterised by the parameter ξ. The threshold of the OPO can be described by the value of $h_m(\xi, B)$ as a function of the two parameters, ξ and B. Following the Boyd and Kleinman theory, in 1977 Fischer *et al.* [22] first theoretically derived the threshold condition for singly-resonant OPO's with tightly focused pump. However, their derivations were restricted to the pump and signal sharing the same confocal parameters. In 1982, Guha, Wu and Falk extended the Boyd and Kleinman theory and derived threshold formulae for singly-resonant and doubly-resonant OPOs with no restrictions for the beam sizes of pump, signal, and idler where they adopted a Green's function approach and allowed for diffraction, walk-off and focusing[23]. Therefore, Guha's model is preferable for our case. However, they considered a type I phase-matching case where the pump wave is an extraordinary wave, and the signal and idler are ordinary waves. To enable Guha's model to be used in a more general case, we have extended Guha's theory to be suitable for any type of phase-matching. We write the fields of the pump wave and the resonated signal wave in the form

$$E_{p,s} = \frac{E_{op,s}}{1 + i\tau_{p,s}} \exp(ik_{p,s}z) \exp\left[-\frac{[x - \alpha_{p,s}(z - L/2)]^2 + y^2}{\omega_{op,s}^2 (1 + i\tau_{p,s})}\right] \tag{2.100}$$

where the double refraction angle α can be zero or non-zero to indicate an ordinary or extraordinary wave. For the non-resonant idler wave, the Green's function can be written in the same way as given by Guha[23], namely

$$G_i(r, r') = \frac{\omega_i}{2\pi i c} \frac{\exp[ik_i(z - z')]}{z - z'} \times \exp\left\{ik_i \frac{[x - \alpha_i(L - z') - x']^2 + (y - y')^2}{2(z - z')}\right\} \tag{2.101}$$

Using the idler polarization as a source term in the Maxwell wave equation with a Green's function approach, the idler electric field can be derived from

$$E_i(r) = \frac{2\pi i\omega_i}{c}\int P_i(r')G_e(r,r')dr' \tag{2.102}$$

and the resultant idler field is then

$$E_i(x,y,z) = \pi K_1 \exp(ik_i z)\int \frac{\exp(i\Delta k z')}{(1+i\tau_p')(1-i\tau_s')(z-z')ib}\exp\left[a_3(x^2+y2)\right]$$

$$\times \exp\left\{2x\left[a_{4s}\alpha_s + a_{4p}\alpha_p - a_3(L-z')\alpha_i\right] + a_3\alpha_i^2(L-z')_{4s}^2 - a_{5s}\alpha_s^2 - a_{5p}\alpha_p^2\right\}$$

$$\times \exp\left[2\alpha_i(L-z')(\alpha_s a_{4s} + \alpha_p a_{4p}) + 2a_{sp}\alpha_p\alpha_s\right]dz'$$

where, all notations used here without explicit definition are to be understood as in Ref.[23]; and

$$a_{4s} = -\frac{i2k_i(z'-L/2)}{(z-z')c_s'^* 4ib}$$

$$a_{4p} = -\frac{i2k_i(z'-L/2)}{(z-z')c_p' 4ib}$$

$$a_{5s} = (z'-L/2)^2\left[\frac{1}{c_s'^*} - \frac{1}{ib(c_s'^*)^2}\right]$$

$$a_{5p} = (z'-L/2)^2\left[\frac{1}{c_p'} - \frac{1}{ib(c_p')^2}\right]$$

$$a_{sp} = \frac{(z'-L/2)^2}{ibc_p'c_s'^*}$$

Substituting the signal polarization field and the signal field [given by Eq.(2.100)] into:

$$\Delta P_s = -\frac{1}{2}\omega_s Im\int E_s^* P_s dxdydz, \tag{2.103}$$

and integrating over the crystal, the incremental power of the signal during a forward-going trip is then:

$$\Delta P_s = K_2\cdot I_m\left\{-\frac{i\pi b_p^2 b_s^2}{4k_i^2(b_p+b_i-b_s)}\mathbf{I}_1\right\} \tag{2.104}$$

where

$$\mathbf{I}_1 = \int_0^1\int_0^{z_2}\frac{\exp\left[i\Delta kL(z_1-z_2)\right]}{(z_1+A_s)(z_2+A_s^*)+C_s}dz_1dz_2$$

$$\times \exp\left(-\alpha_p^2 f_p - \alpha_s^2 f_s + \alpha_i^2 f_i + \alpha_s\alpha_p f_{sp} + 2\alpha_p\alpha_i f_{pi} + 2\alpha_s\alpha_i f_{si}\right) \tag{2.105}$$

and

$$
\begin{aligned}
f_p &= a_{5p}^* + \tfrac{(z-L/2)^2}{c_p} - \left(\tfrac{z-L/2}{c_p} + a_{4p}^*\right)^2 \tfrac{1}{ib_1} \\
f_s &= a_{5s}^* + \tfrac{(z-L/2)^2}{c_s^*} - \left(\tfrac{z-L/2}{c_s^*} + a_{4s}^*\right)^2 \tfrac{1}{ib_1} \\
f_i &= (L-z')^2 \left(a_3^* + \tfrac{(a_3^*)^2}{ib_1}\right) \\
f_{si} &= (L-z') \left[a_{4s}^* \left(1 + \tfrac{a_3^*}{ib_1}\right) + \tfrac{(z-L/2)a_3^*}{c_s^* ib_1}\right] \\
f_{pi} &= (L-z') \left[a_{4p}^* \left(1 + \tfrac{a_3^*}{ib_1}\right) + \tfrac{(z-L/2)a_3^*}{c_p ib_1}\right] \\
f_{sp} &= a_{sp}^* + \left[a_{4s}^* + \tfrac{(z-L/2)}{c_s^*}\right] \left[a_{4p}^* + \tfrac{(z-L/2)}{c_p}\right] \tfrac{1}{ib_1}
\end{aligned}
\tag{2.106}
$$

The pump power threshold P_{pt} can be determined by equating the signal gain to the round trip loss. If $\epsilon_s/2$ denotes the fractional loss per pass then

$$\Delta P_s = \epsilon_s P_s$$

which gives

$$\epsilon_s P_s = K_3 P_s P_p h_s$$

$$h_s = \frac{1}{4} \frac{(1+k)}{\xi_p + k\xi_s} R_e \mathbf{I}_1 \tag{2.107}$$

so that

$$P_{pt} = \epsilon_s / (K_3 h_s) \tag{2.108}$$

where the parameter h_s is similar to the parameter h_m as mentioned before, it encompasses all spatial effects and is optimizable. The expression for P_{pt} must be evaluated numerically. It should be mentioned that under plane wave assumption, the calculated minimum value of threshold occurs at $\Delta k = 0$, but it is not true when focused Gaussian beam is considered, the Δk should slightly move from zero. This is because, at a tight focus, the mixing of the noncollinear components of the signal and idler fields requires slightly longer k vectors than does the collinear mixing.

Pump threshold of double-pass-pumped SRO

The high pump threshold in a single-pass-pump SRO can be possibly improved by non-resonantly reflecting the pump wave back through the nonlinear medium. Such a pump

configuration is named "double-pass-pump" in this thesis. For a SRO in the double-pass-pump, the output mirror is high reflecting at ω_p, and both mirrors are high transmitting for the non-resonant wave. Hence as it has been pointed out by Bjorkholm *et al.* [24], the phase of the non-resonant wave at the entrance face of the crystal is determined by the phases of the pump and the resonant wave at that point, so that the phases of the forward-going pump and resonant waves at entrance and of the backward-going pump and resonant waves at exit are not important. The pump threshold in such a pump configuration can be also discussed for both plane wave and focused Gaussian wave assumption.

(1) Pump threshold for plane wave: As has been reported by Bjorkholm *et al.* [24] for the plane wave case, the pump threshold in a double-pass-pumped SRO can be expressed by means of the pump threshold of a single-pass-pumped SRO as:

$$I_t(R_p) = I_t(0)/(1 + R_p) \tag{2.109}$$

where $I_t(0)$ is the threshold pump intensity for a single-pass SRO [see Eq.(2.99)]. This equation shows clearly that the pump threshold of a double-pass SRO can be up to a factor of **2** lower than that of a single-pass SRO. A detail derivation with a similar result to the Eq.(2.109) can be seen in Ref.[25]. However, this conclusion may not be quite right if one considers the case of a focused Gaussian beam, and particularly in the presence of tight focusing or Poynting vector walk-off.

(2) Pump threshold for focused Gaussian wave: To calculate the pump threshold for a double pass pumped SRO, we made the second theoretical extension from Guha's theory. The details are given as follows.

With the low-gain assumption that P_p, P_s and P_i are all constant during a round trip of the pump, the gain of the signal is then

$$\Delta P_s = \Delta P_s^+ + \Delta P_s^-$$

where ΔP_s^+, and ΔP_s^- are the forward-going and backward-going power gains respectively. The gain of the forward-going ΔP_s^+ can be calculated from Eq.(2.104). In determining the backward-going gain, we use z^- to differ from z where $z = z^- + L$. Only an interaction where the pump and signal are ordinary waves and the idler is an extraordinary wave, is considered here. We write the backward-going pump field as:

$$E_p^- = \frac{r_p E_{op}}{1 + i\tau_p^-} \exp\left[ik_p\left(z^- + L\right)\right] \exp\left[-\frac{x^2 + y^2}{\omega_{op}^2\left(1 + i\tau_p^-\right)}\right] \tag{2.110}$$

and the resonated signal field as:

$$E_s^- = \frac{E_{os}}{1+i\tau_s^-}\exp(ik_s z^-)\exp\left[-\frac{x^2+y^2}{\omega_{os}^2\left(1+i\tau_s^-\right)}\right] \tag{2.111}$$

where r_p is the amplitude reflection coefficient of the pump wave for the output mirror of the OPO; $\tau_p^- = 2(z^- + L/2)/b_p$, and $\tau_s^- = 2(z^- - L/2)/b_s$.

An important difference arises when the backward-going pump is a divergent-wave, but the signal is a resonantly constrained-wave. The Green function used to determine the backward-going idler field for the extraordinary case can be written in the same form as the forward-going, and is:

$$G_e^-(z^-, z^{-'}) = \frac{\omega_i}{2\pi ic}\frac{\exp[ik_i(z^- - z^{-'})]}{z^- - z^{-'}}\exp\left\{ik_i\frac{[x-x'-\alpha_i(L-z^{-'})]^2+(y-y')^2}{2(z^- - z^{-'})}\right\} \tag{2.112}$$

and the idler field is then derived to be:

$$E_i^- = \pi K_1^- \exp[i(k_i z^- + k_p L)]\int \frac{\exp(i\Delta K z^{-'})}{(1+\tau_p^{-'})(1-\tau_s^{-'})(z^- - z^{-'})ib^-} \tag{2.113}$$

$$\exp[a_3^-(x^2+y^2) - 2xa_3^-(L-z^{-'})\alpha_i + a_3^-\alpha_i^2(L-z^{-'})^2]dz^{-'}$$

where

$$K_1^- = \frac{r_p d\omega_i^2 E_{op}E_{os}^*}{c^2}$$

The signal gain in a backward-going direction can be determined from the same equation as described in Eq.(2.103). To evaluate h_s^- while avoiding complex mathematical processing, a simple way is substituting the integral results from Eq.(2.103) into the following relation:

$$\Delta P_s^- = R_p K_3 P_s P_t h_s^- \tag{2.114}$$

where, $R_p = r_p^2$, and K_3 is a factor depending on material parameters and wavelengths,

$$K_3 = \frac{128\omega_s\omega_i d^2\pi^2 l_c}{n_p n_s n_i c^3}\frac{k_s k_p}{k_s + k_p} \tag{2.115}$$

Hence, the h_s^- function for a backward-going wave can be determined numerically, and the signal gain for one round trip under the conditions of double-pass-pumping and idler wave walk-off is then

$$\Delta P_s = \Delta P_s^+ + \Delta P_s^- = K_3 P_s P_p(h_s^+ + R_p h_s^-) \tag{2.116}$$

Equating the signal gain to the round trip loss, then the steady state threshold pump power is given by:

$$P_{pt} = \frac{\epsilon_s}{K_3(h_s^+ + R_p h_s^-)} \tag{2.117}$$

In particular cases as we will present at Chapter 5, one can find that h_s^- might be larger than h_s^+ depending on the phase-matching and focusing conditions. Hence, unlike it has been reported by Bjorkholm [24] for the plane-wave consideration, the pump threshold of double-pass-pump for focused Gaussian-wave might be reduced by **more than the factor of 2.**

2.4.2 Conversion efficiency

It is well know that with the availability of several newly developed nonlinear materials, the research in nonlinear frequency conversion has been re-invigorated. The higher optical damage thresholds and higher nonlinear coefficients of these materials result in an increased energy conversion efficiency in either sum-frequency mixing, difference-frequency mixing or optical parametric oscillation processes. Therefore, the widely used theoretical treatments with the assumption of negligible pump or fundamental beam depletion are no long suitable for most real cases. However, the exact plane wave solution does allow numerical modelling with the effects of depletion, walk-off and arbitrary mirror reflectivity included.

To calculate the conversion efficiency of the Q-switched laser-pumped SRO, using Eq.(2.22), we have built a model with the following assumptions:

1. The intensity distribution is uniform across each beam.

2. The OPO mirrors have perfect transmission at the wavelength of the non-resonant wave.

3. Crystal absorption is taken into account as part of the round trip loss.

4. Zero phase-mismatch, $\Delta k=0$, is assumed.

5. A Gaussian temporal profile for the pump is assumed, namely

$$P_p = P_{p0} \exp\left[-(2t/\tau_p)^2\right]$$

where τ_p is the $1/e^2$ intensity half-width. The actual temporal profile of a Q-switched pulse might be slightly different, but not substantially so.

6. The pump pulse duration is divided into sub-intervals Δt, each of which has the duration of a signal-wave round trip, *i.e.*

$$\Delta t = 2\left[l + (n_s - 1)l_c\right]/c$$

where l is cavity length of the OPO, and n_s is refractive index of the medium for the signal wave. The amplitude of the pump within each sub-interval is assumed to be constant.

7. The generated signal wave is amplified as it makes m cavity transits from initial parametric noise. The initial conditions for the signal (as well as the idler) can be determined from the quantum approach [15], in which the mean value of the electrical field vanishes in the 0-photon state and the mean square deviation is different from zero. As a consequence when no photon is present in the signal cavity mode ω_s, it corresponds to a finite energy density given by:

$$U = \frac{\hbar\omega_s}{2V}$$

where $\hbar\omega_s/2$=Energy of the $0 - photon\ state$ for the mode ω_s, V is the mode volume in the OPO cavity, $V = \pi w_o^2 l$. The initial field of the signal and idler are then given by

$$E_j(0) = \sqrt{\frac{n_j c}{\pi w_o^2 l}}, \qquad j = s, i.$$

For a given OPO cavity and pump beam, the beam waist and therefore the beam intensity of signal and pump are known. Hence the boundary condition for the photon flux of the pump at each round trip can be determined by: [see Eq.(2.47)]

$$u_p^2(0) = \frac{I_p \cos^2 \alpha_p}{\omega_p W}$$

where I_p is the intensity of the pump at the beginning of the pass through the crystal, W=I_p+I_s+I_i, and α_p is the double refraction angle of the pump (for a ordinary wave, α_p=0.).

For a singly-resonant OPO, the boundary condition for the photon flux of the idler at each round trip is

$$u_i^2(0) \approx 0$$

therefore, the term of the integration constant Γ [see Eq.(2.54)] which contains the initial phase difference of the three waves is equal to zero, and causing

$$\Gamma = \frac{1}{2}\Delta S u_p^2(0)$$

This shows that the initial phase of the three waves is not of consequence for the SRO operation.

For a single-pass-pump configuration, the initial value of signal photon flux at the input surface of the crystal for the (n+1)th signal round trip is determined from the nth round trip for a single-pass-pump configuration, *e.g.*

$$u_s^2(0)_{n+1} = T_s u_s^2(0)_n$$

where T_s is signal transmission of the output mirror.

For a double-pass-pumped case, the initial conditions of the three waves can be determined in a similar way as described above, but the sub-interval Δt has to take the duration of half signal-wave round trip.

With the further approxmation[3] of Δk=0, we have

$$\Delta S = 0$$
$$\Gamma = 0$$

and the simplified solutions for the denominator polynomial [see Eq.(2.55)] are then

$$u_{3a} = 0$$

$$u_{3b} = m_1 = u_p(0)$$
$$u_{3c} = m_2 = \sqrt{u_s^2(0) + u_p^2(0)}$$

According to Eq.(2.56), we know that $y(0)$=1, and the elliptic integral $F[\sin^{-1} y(0), \gamma]$ becomes:

$$\mathbf{F}(\pi/2, \gamma) = \mathbf{K}(\gamma)$$

where $\mathbf{K}(\gamma)$ is a complete elliptic integral of the first kind, and consequently

$$\xi_0 = \mathbf{K}(\gamma)/u_{3c}$$

The identity $sn[u + 2K(\gamma), \gamma]$=$sn(u, \gamma)$ transforms Eqs.(2.59)-(2.61) to be:

$$u_p^2(\xi) = u_p^2(0) \times sn^2\left[\sqrt{u_p^2(0)}(\xi + \xi_0)/\gamma, \gamma\right] \tag{2.118}$$

$$u_s^2(\xi) = u_s^2(0) + u_p^2(0) - u_p^2(\xi) \tag{2.119}$$

$$u_i^2(\xi) = u_p^2(0) - u_p^2(\xi) \tag{2.120}$$

[3] As noted by Bey and Tang [9], without the assumption of zero phase-mismatch, it was found difficult to numerical solve the cubic polynomial in the region of small pump depletion.

where

$$\gamma^2 = u_p^2(0)/(u_s^2(0) + u_p^2(0)) \tag{2.121}$$

and the associated intensity solutions for the three beams are:

$$\mathbf{I}_j(\xi) = \frac{u_i^2(\xi)\omega_i W}{\cos^2 \alpha_i} \qquad j = p, s, i. \tag{2.122}$$

Integrating intensity $\mathbf{I}_{sj}(\ j = 1, 2, ...n,)$ over each time interval, the output energy of signal can be determined from

$$E_s = \sum_0^n T_s \mathbf{I}_{sj} \pi w_{os}^2 \Delta t \tag{2.123}$$

where T_s is the output mirror's transmission at signal wavelength, and w_{os} is the signal beam waist determined by the OPO cavity.

The overall conversion efficiency can be found from the given pump energy and the predicted signal output energy, namely

$$\eta_{opo} = \frac{E_s}{E_p} \tag{2.124}$$

A similar treatment to simulate the process of SRO can be seen from Ref.[15].

2.4.3 OPO linewidth

For a SRO, the gain linewidth is limited by the bandwidth of phase-mismatching, (*i.e.*, Δk $l_c/2{=}\pm\pi$). Therefore, the linewidth of a OPO can be predicted in a similar way to determining the acceptance parameters. We expand the phase-mismatching due to a shift in the signal (or idler) wavelength in a Taylor series, and then the signal (or idler) linewidth of an OPO can be described as [see Eq.(2.82)]:

$$\Delta\omega_s = \frac{-\frac{\delta\Delta k}{\delta\omega_s} \pm \sqrt{\left(\frac{\delta\Delta k}{\delta\omega_s}\right)^2 + \frac{4\pi}{L}\frac{\delta^2\Delta k}{\delta\omega_s^2}}}{\frac{\delta^2\Delta k}{\delta\omega_s^2}} \tag{2.125}$$

Further assuming that the pump wavelength is constant, then the shift in ω_s will result in a shift in ω_i with a simple relation, $\Delta\omega_s = -\Delta\omega_i$, and the terms in the Taylor series in Eq.(2.125) can be written as :

$$\frac{\delta\Delta k}{\delta\omega_s} = \frac{1}{c}\left[n_i - n_s + \frac{\delta n_i}{\delta\omega_i}\omega_i - \frac{\delta n_s}{\delta\omega_s}\omega_s\right]$$

$$\frac{\delta^2\Delta k}{\delta\omega_s^2} = -\frac{1}{c}\left[2\left(\frac{\delta n_i}{\delta\omega_i} + \frac{\delta n_s}{\delta\omega_s}\right) + \frac{\delta^2 n_i}{\delta\omega_i^2}\omega_i + \frac{\delta^2 n_s}{\delta\omega_s^2}\omega_s\right]$$

In most cases, the first order in the expansion is larger than the second[26]. If the first order term dominates, we find that:

$$\Delta\omega_s \approx \frac{2\pi c}{l_c}\frac{1}{\Delta n}$$

where Δn is the birefringence. Thus, it shows clearly that the spectral bandwidth depends inversely on the birefringence and crystal length.

2.5 Theory of sum-frequency generation

Sum-frequency generation (SFG) is a frequency up-conversion process, in which radiation of frequency ω_1 and radiation of frequency ω_2 ($\omega_2 \geq \omega_1$) are mixed to generate high frequency radiation of $\omega_3 = \omega_1 + \omega_2$. The harmonic generations, such as frequency doubling, tripling and quadrupling, are special cases of sum-frequency generation, in which the input radiations are from one fundamental laser source. However, for general SFG the input radiations are from two laser sources and according to the condition of photon energy conservation, the intensity ratio of the two fields should be adjusted in proportion to the ratio of the frequencies, *i.e.* $I(\omega_2)/I(\omega_1) \propto \omega_2/\omega_1$.

Theoretically, harmonic generation, particularly second harmonic generation, has been studied extensively [27, 28], but SFG has not received a great deal of attention until recently when effective OPOs became available [29]. In this section, two questions will be discussed briefly, namely what are the optimum focusing conditions and associated conversion efficiency calculations for SFG.

2.5.1 Optimum focusing

In the same way as with SHG, the basic consideration for SFG is the optimum focusing condition to achieve maximum efficiency. A question here is: what is the optimum input beam overlap, is it equal beam spot size or equal confocal parameter? Again, the answer has been given by Guha and Falk [30]. With the approach of either the Green function or Fourier transform, they demonstrated for SFG that maximum efficiency occurs at $b_1 = b_2 = l_c/2.84$ in the absence of Poynting vector walk-off, and at $b_1 \neq b_2$ in the presence of walk-off, where b is the confocal parameter, $b_i = w_o^2/k_i$, i=1, 2.

2.5.2 Conversion efficiency

With the small signal approximation, the intensity of the sum-frequency generated in SFG is described by Eq.(2.38), from which we can see that the conversion efficiency of SFG is proportional to the square of d_{eff} and crystal length.

However to take factors such as depletion and walk-off into account in the calculation, the exact solution of plane wave theory has to be used. Essentially, the model is built in the same way as that for the SRO case, but the time sub-interval can be chosen arbitrarily.

If the process of SFG is described by the frequency conditions: $\omega_3 = \omega_2 + \omega_1$, and $\omega_3 \geq \omega_2 \geq \omega_1$; then the boundary condition for the exact plane wave solution is:

$$u_3^2(0) = 0 \tag{2.126}$$

this leads to:

$$\Gamma = 0, \quad \text{and} \quad u_{3a}^2 = 0. \tag{2.127}$$

and therefore

$$y_0 = \frac{u_3(0)}{u_{3b}} = 0$$

$$\xi_0 = \frac{\mathbf{F}\left(\sin^{-1}\left[y(0)\right], \gamma\right)}{u_3}$$

$$= \frac{1}{u_3}\int_0^{\sin(0)} \frac{dx}{(1-x^2)(1-\gamma^2 x^2)} = 0$$

From the given beam waist, pulse profile and energy of the two input beams, the boundary condition of photon fluxes can be determined by

$$u_i^2(0) = \frac{I_i \cos^2 \alpha_i}{\omega_i W}$$

where I_i,(i=1, 2.) is the intensity of input beam at the beginning of the pass through the crystal, W=I_1+I_2, and α_i is the double refraction of the input wave (for ordinary wave, $\alpha_i = 0.$).

The other two roots of the denominator polynomial Eq.(2.93), u_{3b}^2 and u_{3c}^2, can be derived from:

$$u_3^2\left(m_2 - u_3^2\right)\left(m_1 - u_3^2\right) - \left(\frac{1}{2}\Delta S u_3^2\right)^2 = 0 \tag{2.128}$$

which are

$$u_{3b}^2 = \frac{1}{2}(m_1 + m_2 + \frac{1}{4}\Delta S^2) - \sqrt{\left(m_1 + m_2 + \frac{1}{4}\Delta S^2\right)^2 - 4m_1 m_2} \tag{2.129}$$

$$u_{3c}^2 = \frac{1}{2}(m_1 + m_2 + \frac{1}{4}\Delta S^2) + \sqrt{\left(m_1 + m_2 + \frac{1}{4}\Delta S^2\right)^2 - 4m_1 m_2} \tag{2.130}$$

where $m_1 = u_1(0)^2$, and $m_2 = u_2(0)^2$. Thus, the normalised solutions for the process of SFG are given by

$$u_3^2(\xi) = u_{3b}^2 \times sn^2[u_{3c}\xi, \gamma]$$

$$u_2^2(\xi) = u_2^2(0) - u_3^2(\xi) \tag{2.131}$$

$$u_2^2(\xi) = u_2^2(0) - u_3^2(\xi)$$

where:

$$\gamma = \frac{u_{3b}}{u_{3c}}.$$

Inverting Eq.(2.131) into intensity solutions by using Eq.(2.47), then

$$\mathbf{I}_i(\xi) = \frac{u_i^2(\xi)\omega_i W}{\cos^2 \alpha_i} \qquad i = 1, 2, 3. \tag{2.132}$$

Integrating intensity $\mathbf{I}_{3j}$($j = 1, 2, ...n$,) over each time interval, the output energy of the sum-frequency wave can be determined from

$$E_3 = \sum_0^n \mathbf{I}_{3j} \pi w_{o3}^2 \Delta t$$

where w_{o3} is the beam waist generated, assumed to be equal to the smallest waist of the input beams.

The overall conversion efficiency then can be determined from the energies of the input waves and the predicted energy of the sum-frequency wave, namely:

$$\eta_{opo} = \frac{E_3}{E_1 + E_2}$$

Bibliography

[1] Malcolm H. Dunn, *Introduction to Nonlinear Optics*, University of St Andrews, Scotland, July 1985.

[2] R. W. Boyd, *Nonlinear Optics*, Academic Press Inc. 1992.

[3] G. D. Boyd and D. A. Kleinman, *J. Appl. Phys.* **39**, 3597 (1968).

[4] M. Born and E. Wolf, *Principles of Optics*, Oxford University Press, New York, 1970.

[5] V. G. Dmitriev, G. G. Gurzadyan, and D. N. Nikogosyan, *handbook of Nonlinear Optical Crystals*, springer-Verlag Berlin Heidelberg, 1991.

[6] F. Brehat and B. Wyncke, *J. Phys. B: At. Mol. Opt. Phys.* **22**, 1891-1898 (1989).

[7] J. A. Armstrong, N. Bloembergen, J. Ducuing, and P. S. Pershan, *Phys. Rev.* **127**, 1918 (1962).

[8] R. A. Baumgartner and R. L. Byer, *IEEE J. Quantum Electron.* **QE-15**, 432 (1979).

[9] P. P. Bey, and C. L. Tang, *IEEE J. Quantum Electron.* **QE-8**, 361 (1972).

[10] A. Yariv and P. Yeh, *Optical Waves in Crystals*, New York: Wiley, 1984.

[11] J. M. Manley and H. E. Rowe, Proc. IRI, **44**, 904 (1956).

[12] P. F. Byrd and M. D. Friedman, *Handbook of Elliptic Integrals for Engineers and Scientists*, 2nd ed. New York: Springer, 1971.

[13] R. E. Scraton, *Basic Numerical Methods*, Edward Arnold Ltd, 1985.

[14] H. J. Bakker, *Phys. Rev. A***45**, 5126 (1992).

[15] J. M. Breteau, C. Jourdain, T. Lepine and F. Simon, OSA Proceedings on Advanced Solid-State Lasers, **15**, 137 (1993).

[16] A. V. Smith, W. J. Alford, and T. D. Raymond, *J. Opt. Soc. Am. B* **12**, 2253 (1995).

[17] A. V. Smith and M. S. Bowers, *J. Opt. Soc. Am. B* **19**, 1520 (1994).

[18] L. P. Yuan, Chinese air force, pub 23-134, Taibei 106, Taiwan.

[19] J. Q. Yao and T. S. Fahlen, *J. Appl. Phys.* **55**, 65 (1984).

[20] J. E. Bjorkholm, *IEEE J. Quantum Electron.* **QE-7**, 109 (1971).

[21] S. J. Brosnan and R. L. Byer, *IEEE J. Quantum Electron.* **QE-15**, 415 (1979).

[22] R. Fischer, C. Tranba, and L. W. Wieczorek, *Sov. J. Quantum Electron.* **7**, 1455 (1977).

[23] S. Guha, F. J. Wu, and J. Falk, *IEEE J. Quantum Electron.* **QE-18**, 907 (1982).

[24] J. E. Bjorkholm, A. Ashkin, and R. G. Smith, *IEEE J. Quantum Electron.* **QE-6**, 797 (1970).

[25] S. T. Yang, R. C. Eckardt, and R. L. Byer, *J. Opt. Soc. Am. B* **10**, 1684 (1993).

[26] Norman P. Barnes and Vincent J. Corcoran, *Appl. Opt.* **15**, 696 (1976).

[27] D. A. Kleinman, A. Ashkin, and G. D. Boyd, *Phys. Rev.* **145**, 338 (1966).

[28] David Einerl, *IEEE J. Quantum Electron.* **QE-23**, 575 (1987).

[29] Gerald T. Moore and Karl Koch, *IEEE J. Quantum Electron.* **QE-29**, 2334 (1995).

[30] Shekhar Guha and Joel Falk, *J. Appl. Phys.* **51**, 50-60 (1980).

Chapter 3

Nonlinear material

Although there is now considerable choice in selecting nonlinear materials as a result of recent developments in the growing and availability of new crystals, striking a balance between the physical limitation of a crystal and the demands of a particular application is, however, still a very important task.

Basically a material must satisfy four criteria if it is to be useful for frequency conversion, and these are adequate nonlinearity, wide optical transparency, significant birefringence for phase-matching, and a sufficiently high damage threshold.

The nonlinear materials that can meet the above requirements and hence are currently widely used for OPOs and SFG are the **niobates**, such as $LiNbO_3$, $LiIO_3$, and $KNbO_3$; **borates**, such as LiB_3O_5 and BaB_2O_4 (BBO); and the **KTP isomorphs**, such as $KTiOPO_4$ (KTP), $KTiOAsO_4$ (KTA), $CsTiAsO_4$ (CTA), and $RbTiOAsO_4$ (RTA).

KTP and LBO are the two crystals which have been used in this research. Before summarizing the properties of the two crystals, a brief review on other crystals (as mentioned above) may be very useful for comparison.

3.1 A review on some useful crystals

3.1.1 Lithium niobate ($LiNbO_3$) and Lithium iodate ($LiIO_3$)

$LiNbO_3$ is a uniaxial ferroelectric crystal of point group 3m. The main advantages of this crystal are its large nonlinearity (5.44 pm/V) and the capability of non-critical phase-

matching. A later discovery was that the addition of MgO to $LiNbO_3$ greatly reduces the photo-refractive induced damage and leads to uniform high-quality large-sized single crystals being available. At the standard doping level of 5% MgO, the threshold of damage has been reported to increase by two orders of magnitude [1]. Damage thresholds of 610 and 340 $MWcm^{-2}$ were reported for 1.064 and 0.532 μm radiation respectively for doped $LiNbO_3$[2, 3]. However, a damage threshold of approximately 30 to 50 $MWcm^{-2}$ was also reported due to a two-photon absorption process. The absorption in lithium niobate is low in the region of 1 μm (0.001/cm), while increasing significantly by the time the wavelength falls to 0.532 μm (0.02/cm). Type I phase-matching with the scheme of $\omega_3^e = \omega_1^o + \omega_2^o$ is the only effective geometry in $LiNbO_3$. In this geometry, the effective nonlinear coefficient[4] is:

$$d_{eff} = d_{15} \sin\theta - d_{22} \cos\theta \sin 3\phi \tag{3.1}$$

We must choose ϕ and θ correctly so that the d_{15} and d_{22} add and not subtract for $\theta \neq 90^o$. As shown in Fig. 3.1, the calculated maximum d_{eff} of $LiNbO_3$ from the above formula and using the data presented in [4], is 6.09 pm/V, corresponding to an angle θ of 63^o, and obviously to maximise d_{eff} requires that $\phi = 30^o$.

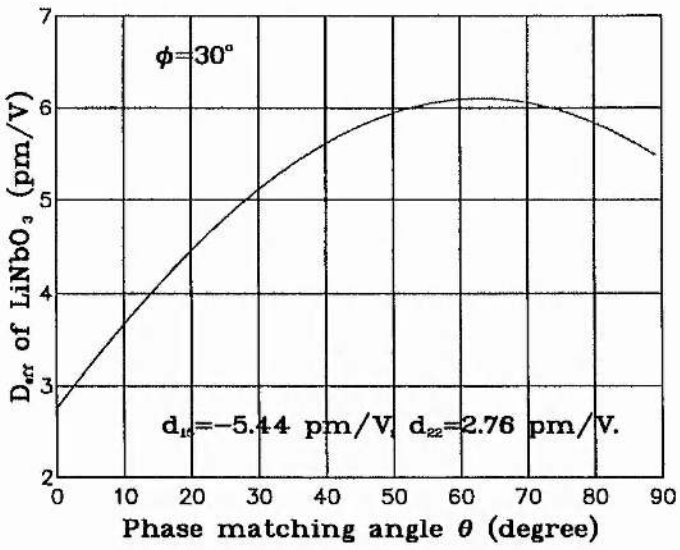

Figure 3.1: The effective nonlinear coefficient of $LiNbO_3$.

An important application of $LiNbO_3$ is in temperature-tuned type I non-critically phase-matched OPOs with a pump wavelength around 0.5 μm, or in reverse, the non-critically

phase-matched frequency-doubling of 1 μm radiation. Fig. 3.2 shows the tuning curve versus operating temperature for a range of pump wavelengths in the range 0.5-0.6 μm. Using the data given in Ref.[4], the calculated d_{eff} of this OPO geometry is 5.44 pm/V. The range of pump wavelengths is limited by the maximum safe operating temperature, and the idler wave can be tuned to reach only about 2 μm, which is much less than the transparency range of the material (5 μm).

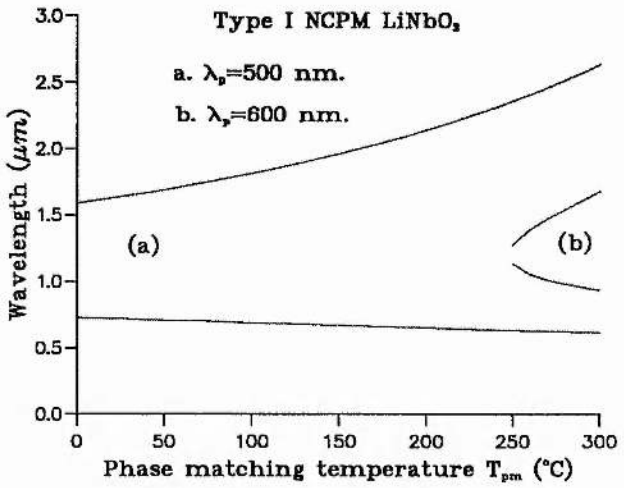

Figure 3.2: Tuning curves of $LiNbO_3$ OPO in type I NCPM geometry for pump wavelengths range 0.5-0.6 μm.

If radiation of wavelength 1 μm is used to pump a $LiNbO_3$ OPO, as shown in Fig. 3.3 (I), the tuning can be extended to 5 μm. In this geometry, the calculated d_{eff} is still around 5 pm/V and for a 10 mm long crystal, the acceptance angle is 1.4 milli-radian, and the walk-off angle is 2^o. An interesting question is whether the OPO performance can be improved by temperature tuning? The answer is yes. Fig. 3.3 (II) illustrates the possibility of temperature tuning the type I critically phase-matched OPO pumped at 1 μm. This geometry, we believe, has the following advantages: (1) the "Fresnel" loss due to angular tuning is avoided; (2) the tuning can cover the whole range from 1.35-5 μm, and there is more flexibility in wavelength range selecting from the combination of both angle and temperature tuning; (3) the phase-matchable angle can be increased by increasing the temperature, and this will lead to slightly large d_{eff} (see Fig. 3.1) and acceptance angle, and smaller walk-off angle.

If $LiNbO_3$ did not suffer from optical damage, it would be the ideal material for OPOs in

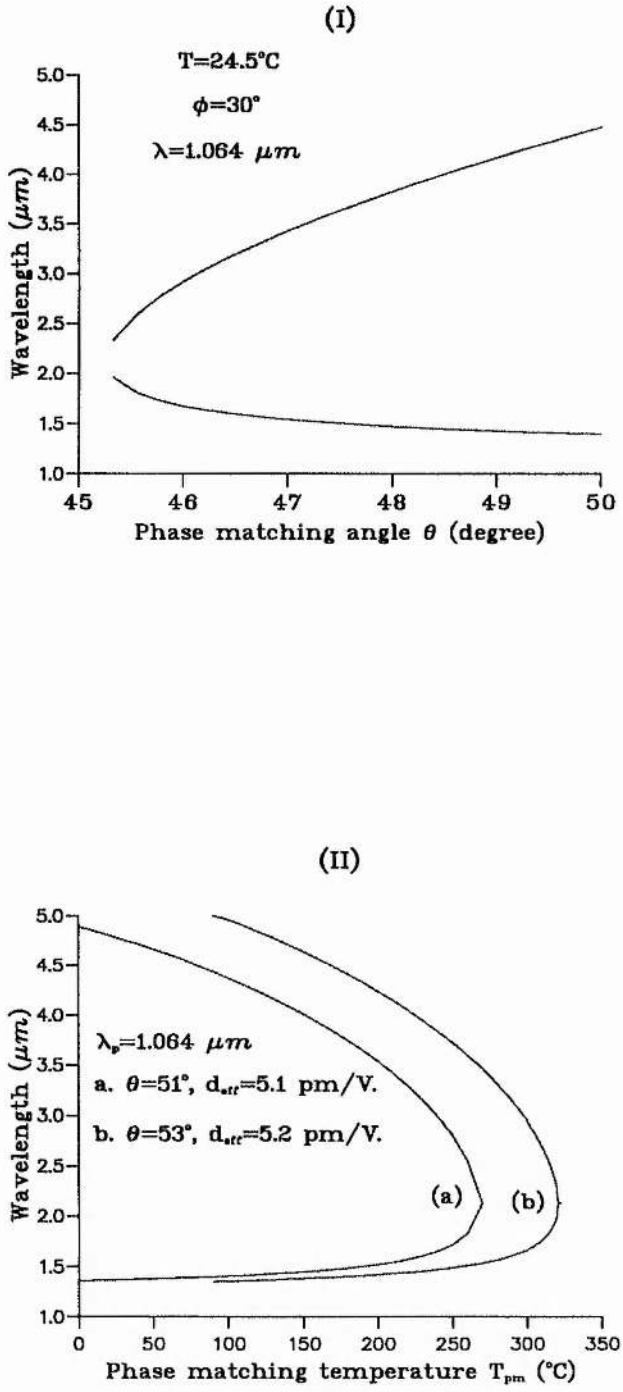

Figure 3.3: Tuning curves of $LiNbO_3$ OPO in type I CPM geometry with pump wavelength of 1.064 μm. I. by angular tuning; II. by temperature tuning.

the infrared region.

In contrast with $LiNbO_3$, lithium iodate ($LiIO_3$) is another crystal which has a large transparency range from 0.3 to 5.5 μm and high nonlinearity (d_{15}=5.5 pm/V). It is a negative uniaxial crystal with point group 6. It can be grown in large high quality single crystals (15 mm aperture, 60 mm length), which have proven efficient for frequency doubling of Nd:YAG and ruby. Because of its low intrinsic optical absorption in the visible and near-infrared, and its relatively low cost per unit volume, $LiIO_3$ is potentially attractive for frequency conversion in large aperture, high average power lasers.

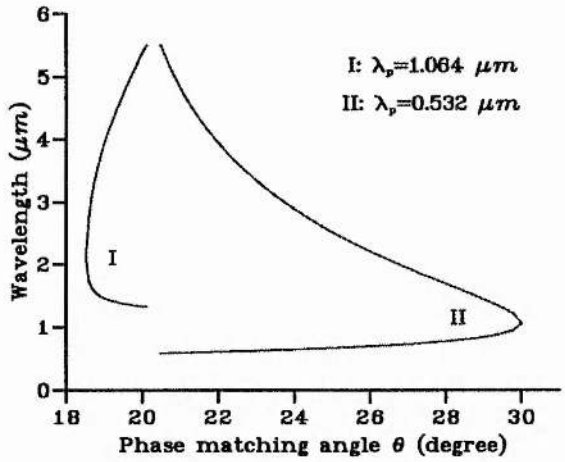

Figure 3.4: Tuning curves of type I phase-matched $LiIO_3$ OPO for pump wavelength of 1.064 μm (I) and 0.532 μm (II).

As with $LiNbO_3$, type I phase-matching with the scheme $\omega_3^e = \omega_1^o + \omega_2^o$ also is the only effective geometry for $LiIO_3$, but it is temperature insensitive. In this geometry, the effective nonlinear coefficient[4] can be calculated from:

$$d_{eff} = d_{15} \sin\theta \tag{3.2}$$

Since there is no non-critical phase-matching geometry, this formula shows that d_{eff} is always less than d_{15} and is independent of angle ϕ. The $LiIO_3$ can be used for OPOs pumped at 0.532 and 1.064 μm, as shown in Fig. 3.4. The tuning range, when pumping with 0.532 μm radiation, is from 0.6 to 4.7 μm. Using 1 μm radiation as pump, the idler can reach to 5.37 μm, with a very sharp tuning rate as shown in Fig. 3.4.

$LiIO_3$ has several drawbacks which limit its application. One is its high birefringence

($\Delta n/n = 8.2\%$ at 0.532 μm), and this has led to a large walk-off angle and small acceptance angle in frequency conversion. For example, in the $LiIO_3$ based type I OPO pumped at 0.532 μm, its walk-off angle is 4^o, which is two times higher than that in $LiNbO_3$ based OPO, and the acceptance angle for a 10 mm long crystal is 0.5 milli-radian which is much smaller than beam divergences associated with most pump lasers. Another significant disadvantage is the prohibitively low damage threshold (50 $MWcm^{-2}$), and this has limited the use of high intensity sources.

3.1.2 Potassium niobate ($KNbO_3$)

In the temperature range T=-50°C to +223°, $KNbO_3$ is orthorhombic with point group symmetry mm2. Its transparency range extends from 0.4 to 5 μm with absorption loss< 0.01 /cm at 1.064 μm. It has a much higher nonlinear coefficient than that of KTP (d_{32}=-18.3 pm/V and d_{31}=-15.8 pm/V). However, the overall conversion efficiency of $KNbO_3$ is limited by the rather small angular acceptance widths. $KNbO_3$ can be used for optical second harmonic generation of near infrared laser light using its large nonlinear coefficients d_{32} and d_{31}. Temperature tuning of the birefringence allows non-critical type I phase-matching in the wavelength ranges from 838 nm at T=-36°C to 946 nm at T=185 °C [5, 6] (d_{32}), and from 986 nm at T= 22 °C to 1064 nm at T=188°C[5](d_{31}). $KNbO_3$ also can be used for OPOs when pumped by neodymium lasers at either the fundamental or the second-harmonic wavelength, producing tunable radiation in the near-infrared spectral region between 0.7 and 3 μm. However, complete and sufficiently accurate Sellmeier equations of $KNbO_3$ were not known until 1992, when Zysset *et al.* completed the measurement of the refractive index for the wavelength range 400−3400 nm with temperatures between 22°C and 180°C[7]. They have also presented an overview of important phase-matching configurations for SHG, SFG, and OPOs[8]. We have noted that there is a large range of temperature phase-matching conditions for SFG with one 1 μm beam and one red beam (around 670 nm −800 nm). However, temperature phase-matched OPOs, are only possible when the pump wavelength is around 0.532 μm. Experimentally, the 0.532 μm pumped temperature phase-matched $KNbO_3$ OPO has been demonstrated by Kato, in which, the wavelength tuning range was 0.86−1.35 μm for a temperature variation of 184 −220°C[9]. Using 100 ps pulse, the measured damage threshold of $KNbO_3$ was 100 GW/cm^2, as reported by Zysset *et al.* [8].

3.1.3 Betabarium borate (BBO)

Barium borate, BBO was discovered in 1984 by Chen and his group[10]. It is a negative uniaxial crystal with a large birefringence and a relatively small dispersion. The main advantages of this crystal are its moderate nonlinearity (d_{22}= 2.2 pm/V), the high transparency in uv spectral region and relative high damage threshold ($\sim$ 10 GW/cm^2). Its transmission region extends from 189 nm to 3500 nm (to half maximum transmission, the range is 198-2600 nm.)[11]. The linear absorption coefficient of BBO is $\sim$ 0.01 /cm at λ=532 nm and $\sim$ 0.5 /cm at λ=2.55 μm. The major disadvantage with BBO is the large walk-off over the majority of its tuning range. BBO is especially suitable for frequency conversion of laser radiation with high peak or high mean power.

The shortest wavelength which can be generated from BBO by SHG is 205 nm, and by SFG is 190 nm. As we have described in the introduction chapter, BBO also is one of the most widely used materials for OPOs in near uv, visible and the near infrared regions.

There has been some confusion in determining the effective nonlinear coefficient of BBO. The problem was due to BBO being assigned to both point group 3 and point group 3m. The d_{ij} tensor for point group 3 is

$$\begin{pmatrix} d_{11} & -d_{11} & 0 & d_{14} & d_{15} & -d_{22} \\ -d_{22} & d_{22} & 0 & d_{15} & -d_{14} & -d_{11} \\ d_{31} & d_{32} & d_{33} & 0 & 0 & 0 \end{pmatrix} \tag{3.3}$$

but for a crystal in point group 3m, its d_{ij} tensor is

$$\begin{pmatrix} 0 & 0 & 0 & 0 & d_{15} & -d_{22} \\ -d_{22} & d_{22} & 0 & d_{15} & 0 & 0 \\ d_{31} & d_{32} & d_{33} & 0 & 0 & 0 \end{pmatrix} \tag{3.4}$$

Finally, Eimerl *et al.* have proved that BBO belongs to the point group 3m[11, 12], and the expressions for d_{eff} should therefore be:

$$\begin{aligned} d_{eff}^{ooe} &= d_{15}\sin\theta - d_{22}\cos\theta\sin 3\phi \\ d_{eff}^{eoe} &= d_{eff}^{oee} = d_{22}\cos^2\theta\cos 3\phi \end{aligned} \tag{3.5}$$

where $d_{11} = 0$.

However, with the erroneous assignment of BBO, the formulae then used for the d_{eff}

calculation were:

$$d_{eff}^{ooe} = d_{15}\sin\theta - \cos\theta(d_{11}\cos 3\phi - d_{22}\sin 3\phi)$$
$$d_{eff}^{eoe} = d_{eff}^{oee} = (d_{11}\sin 3\phi - d_{22}\cos 3\phi)\cos^2\theta \tag{3.6}$$

where $d_{11} \neq 0$.

3.2 Potassium titanyl phosphate and its isomorphs

This section summarises the properties of Potassium titanyl phosphate (KTP) that are relevant to its use as the gain medium in the infrared OPO. In addition, the properties of some KTP isomorphs, such as KTA, CTA, and RTA, are also presented. These crystals are highly promising alternatives for KTP in the further development of this work.

3.2.1 KTP

KTP has been studied and used for its optical quadratic nonlinearity since 1976[13, 14]. It has many desirable properties, such as the large nonlinear coefficient, relatively high damage threshold, wide angular bandwidth and small walk-off angle, high thermal and chemical stability, and wide temperature bandwidth for angle tuned phase-matching.

Crystallographic structure KTP is an orthorhombic biaxial material with point group mm2. The mutually orthogonal principal axes x, y, z (ordered according to increasing refractive index $n_x < n_y < n_z$) correspond to the crystallographic a, b, c.

Transmission Optically, the transparency of KTP extends from 350 nm in the near uv to 4.5 μm in the mid infrared. However, there are some absorption peaks in the region between 2.5-4.5 μm. Kato[15] and Jacco[16] have reported the measured transmission curve for this region. One absorption peak is centred around 3550 /cm (2.8 μm), this is due to the presence of OH^- in the material. Another absorption peak is centred at 3000 cm^{-1} (3.3 μm) as reported by Jacco[16]. This is due to the second overtone of the phosphate fundamental vibration. From the presented transmission curve either by Kato or Jacco, it can be seen that the absorption at 3.3 μm has led to the rapid fall off of the transmission beyond 3.1 μm, and this therefore limits the utility of this compound as a parametric oscillator material at wavelengths longer than 3.3 μm. . The absorption

coefficient in the range 3550 cm^{-1} (2.8 μm) to 4000 cm^{-1} (2.5 μm) is estimated to be 0.069/cm according to the curve given by Kato, and 0.045/cm according to the curve given by Jacco. The absorption coefficient in the near infrared (1.06 - 1.32 μm) tends to be, at least, ten times lower than that in the region around 2.5 μm, which was reported by Gettemy *et al.* [17].

Effective nonlinear coefficient As an orthorhombic biaxial material with point group mm2, its nonlinear susceptibility tensor is of the form:

$$\begin{pmatrix} 0 & 0 & 0 & 0 & d_{15} & 0 \\ 0 & 0 & 0 & d_{24} & 0 & 0 \\ d_{31} & d_{32} & d_{33} & 0 & 0 & 0 \end{pmatrix} \tag{3.7}$$

where the non zero coefficients are d_{15}, d_{24}, d_{31}, d_{32}, and d_{33}. The magnitudes of those nonlinear coefficients were first measured by Zumsteg *et al.* on some fairly small, poor-quality single crystals[13]. However, due to lower than expected efficiency for second harmonic generation, these value have been remeasured by several other researchers and found to be approximately half those originally reported. These include the report from Eckardt *et al.* [18], who found $d_{eff} = 3.18$ pm/V for type II SHG of 1.064 μm, and report from Desalvo *et al.* [19], who had experimentally obtained the same value as reported by Eckardt. Other measurements include the effective d coefficient obtained by Vanherzeele[20] from type II optical parametric fluorescence and parametric amplification conversion efficiencies, and by Brown *et al.* [21] from high energy type II SHG of 1.064 μm. Both confirmed that the value of the effective d coefficient at 1.064 μm was about 3 pm/V. The values determined by Vanherzeele *et al.*, are the most recent, and have found wide spread acceptance in the literature. They are (in pm/V) $d_{15} = 1.91$, $d_{24} = 3.64$, $d_{31} = 2.54$, $d_{32} = 4.35$, and $d_{33} = 16.9$. For a biaxial crystal, the expressions for the effective nonlinear coefficients are much more complicated than a uniaxial crystal, although the d_{eff} can be calculated by using the exact general expressions as given in Chapter 2 [see Eq.(2.23)]. For KTP, under the conditions of the large difference between n_z and n_x or n_y and the small difference between n_x and n_y, the expressions for d_{eff} can be simplified for analysis to (see Refs.[22, 23]):

$$d_{eff}^{I} = \frac{1}{2}(d_{15} - d_{24}) \sin 2\theta \sin 2\phi \tag{3.8}$$

$$d_{eff}^{II/III} = (d_{24} - d_{15}) \sin 2\theta \sin 2\phi - (d_{15} \sin^2 \phi + d_{24} \cos^2 \phi) \sin \theta \tag{3.9}$$

It is obvious that d_{eff} for a type I geometry is much smaller than that for type II/III.

The value of d_{eff} for type II/III is maximised at θ=90°, ϕ=0°, where d_{eff}=d_{24}; at θ=90°, ϕ=90°, it is d_{eff}=d_{15}.

Sellmeier equations In recent years, several sets of Sellmeier equations for both flux-grown and hydrothermally grown KTP have been reported, see Refs.[24, 25, 26, 27]. The two sets of Sellmeier equations reported in Ref.[26, 27] were constructed from a fit to observed phase-matching data for flux-grown KTP and for both flux-grown and hydrothermally grown KTP respectively. The Sellmeier equations reported in Ref.[25] and Ref.[24] were obtained from index measurement by using the minimum deviation method. However, in Ref.[25] only 16 wavelengths between 0.4047 μm and 1.064 μm were utilised, so that the equations can not be used to predict phase matching beyond 1 μm accurately. Although the measurements given in Ref.[24] were based on hydrothermally grown KTP, a good fit between the predictions from their equations and our experiments, based on flux grown KTP, has been found over the range 1.5-3.3 μm[28]. Hence, we have adopted the Sellmeier equations given by Ref.[24] in our work, which are in the form of:

$$n^2 = A + \frac{B}{1-(C/\lambda)^2} - D\lambda^2. \tag{3.10}$$

where λ is the vacuum wavelength in micrometers and the values of A, B, C, and D are listed in Table 3.1.

Phase-matchable regions The calculated wavelength phase-matchable regions for SFG using KTP are plotted in Fig. 3.5 for type II phase-matching, and in Fig. 3.6 for type III phase-matching, where the calculation was under the condition of non-zero d_{eff} and the interaction of

$$\frac{1}{\lambda_3} = \frac{1}{\lambda_1} + \frac{1}{\lambda_2}$$

The figures are symmetrical about the diagonal line. The isopleths of λ_3 show the possible pump wavelength range and OPOs tuning range. Although KTP is also phase-matchable for type I SFG, the low effective nonlinear coefficient (~0.1 pm/V) of this geometry has made it useless. Hence, practically, only type II and type III phase-matched KTP have been used. As shown in Fig. 3.5, KTP offers a large wavelength phase-matchable range for the type II geometry, with an allowed pump wavelength range in this geometry of 0.5 $\mu m \leq \lambda_p \leq$1.7 μm. In contrast, the wavelength phase-matchable range for type III is much smaller, as shown in Fig. 3.6. The shortest phase-matchable wavelength for type III SFG is around 1 μm, therefore, it is not suitable to use with 0.532 μm pumping of OPOs.

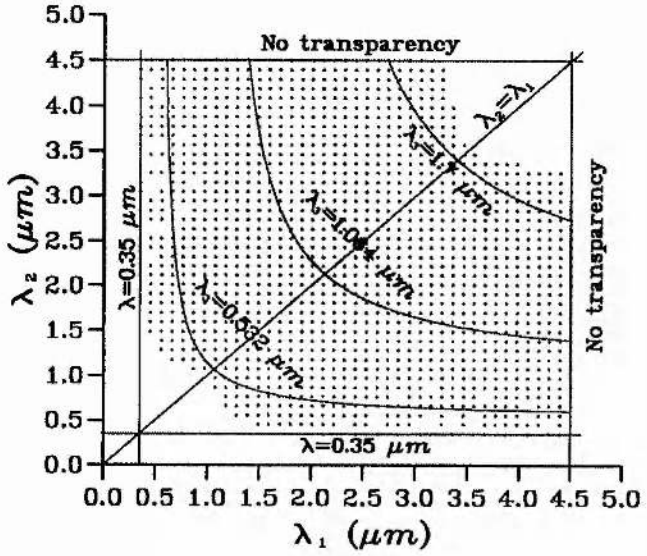

Figure 3.5: Phase-matchable region of TYPE II SFG in KTP.

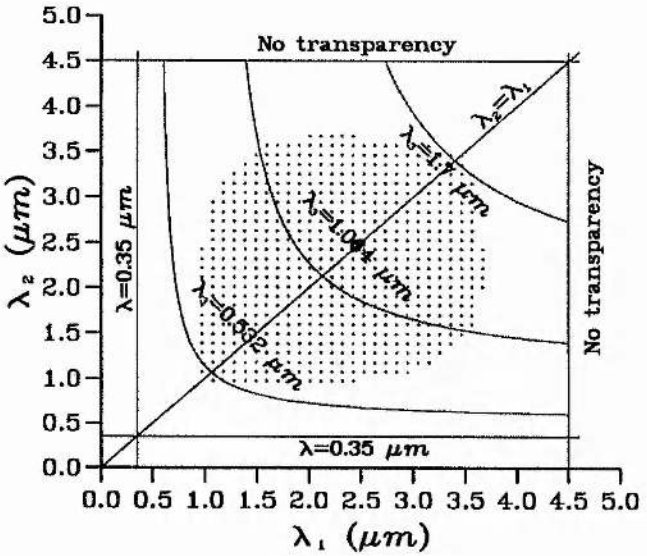

Figure 3.6: Phase-matchable region of TYPE III SFG in KTP.

Thermal behaviour The birefringence of KTP is very insensitive to temperature. A temperature acceptance bandwidth of 24°C cm^{-1} was measured by Fan and Byer[25] for type II SHG of 1.064 μm. The variations of the index of refraction with temperature of KTP at four wavelengths between 0.532μm and 1.32 μm were measured by Gettemy *et al.* [17].

Damage threshold The damage threshold of KTP has been reported in several papers. It has been realised that there are several mechanisms causing KTP damage, which can be crystal inclusion, quality, thermal absorption, and so on. Therefore, the reported damage thresholds are quite different. For instance, Driscoll *et al.* [29], have observed that in one crystal, a bulk damage appeared at an intensity of 650 MW/cm^2 after several repeated hits on the damage site. However in another one, darkening of the interior of the crystal happened at an intensity of 150 MW/cm^2[29]. In our work, it has been found that the intensity of either pump or signal wave has to be limited below to 600 MW/cm^2 to avoid crystal surface damage.

3.2.2 Isomorphs of KTP

In recent years, some isomorphs of KTP, namely $KTiOAsO_4$ (KTA), $CsTiAsO_4$ (CTA), and $RbTiOPO_4$ (RTA), have become available as optical-quality crystals. These crystals are similar in many ways to KTP, but their transparency ranges are extended out to 5 μm and have no significant absorptions out to 3.7 μm. All the three crystals have emerged as new materials for OPOs [30, 31, 32] with the use of non-critical phase-matching and Ti:sapphire femto-second laser pumping in most cases.

The coefficients of Sellmeier equations as given by Eq.(3.10) for KTP and the three isomorphs are listed in Table 3.1. The values of the nonlinear coefficients of these crystals are summarised in Table 3.2.

The simplified expressions of the effective nonlinear coefficient as given by Eq.(3.8) and Eq.(3.9), are also suitable for the three isomorphs. For KTA and CTA OPOs, d_{eff} is maximised at θ=90°, ϕ=0°, with values: $d_{eff}(\max)=d_{24}$=4.5 pm/V in KTA; and $d_{eff}(\max)=d_{24} \simeq d_{32}$=3.4 pm/V in CTA. For RTA OPOs, d_{eff} is maximised at θ=90°, ϕ=90°, with value: $d_{eff}(\max)=d_{15} \simeq d_{31}$=4.1 pm/V.

Figs. 3.7-3.10 illustrate the tuning properties of OPOs based on KTP and the three

Table 3.1: Sellmeier Equation Coefficients of KTP Isomorphs

	KTP[24]	KTA[34]	CTA[35]	RTA[36]
A_x	2.1146	2.1106	2.34498	2.22681
B_x	0.89188	1.0318	1.04863	0.99616
C_x	0.20861	0.2109	0.22044	0.21423
D_x	0.01320	0.0106	0.01483	0.01369
A_y	2.1518	2.3889	2.7444	1.97756
B_y	0.87862	0.7790	0.70733	1.25726
C_y	0.21801	0.2378	0.26033	0.20448
D_y	0.01327	0.0150	0.01526	0.00865
A_z	2.3136	2.3472	2.53666	2.28779
B_z	1.00012	1.1011	1.10600	1.20629
C_z	0.23831	0.2402	0.24988	0.23484
D_z	0.01679	0.0174	0.01711	0.01583

Table 3.2: Nonlinear Optical Coefficients of KTP Isomorphs

	KTP[33]	KTA[34, 37]	CTA[35]	RTA[32]
d_{31} (pm/V)	2.54	2.8	2.1	4.1
d_{32} (pm/V)	4.35	4.2	3.4	1.7
d_{33} (pm/V)	16.9	16.2	18.1	13.7
d_{15} (pm/V)	1.91	2.51	*	*
d_{24} (pm/V)	3.64	4.5	*	*

isomorphs with commonly used pump wavelengths, such as 1.064 μm, 0.532 μm of Nd:YAG laser and 0.8 μm of Ti:sapphire laser.

It can be seen from these figures that the three isomorphs share similar phase-matching properties when used with OPOs.

The tuning characteristics of KTA OPOs are very similar to KTP OPOs. When pumped at $\lambda_p = 1.047 \mu m$ with the use of type III non-critical phase-matching geometry (θ=90°, ϕ=0°), the signal wavelength of the KTA OPO is also around the eye safe region, which is 1.57μm, but the *d*-effective coefficient is 20% larger than that of the KTP OPO as we have mentioned above. Therefore, KTA has been regarded as a ideal alternative to KTP. However, as reported by Power *et al.* [38], the relatively lower output from KTA OPOs than KTP OPOs appears to be a common problem. For example, in a comparison given by Power *et al.* [38], the conversion efficiency of the KTA OPO was 10-15% while it was 30% for the KTP OPO. The possible defects of KTA are optical inhomogeneities due to the inclusion of the indium dopant in the flux, and crystal imperfections as it is a new crystal and its growth technology is still being perfected.

CTA OPOs offer a quite different tuning behaviour from those of KTP and KTA OPOs, as shown in Fig. 3.8. A particular interesting tuning characteristic of CTA OPOs is the degenerate output at the important 1.55 μm spectral wavelength from a non-critically phase-matched geometry.

The tuning curves of RTA OPOs are similar to KTA OPOs, but because its largest phase-matchable nonlinear coefficient is d_{15}, so the most useful principal plane for RTA OPOs is the y-z plane. At $\theta = 90^o$, $\phi = 90^o$ and with a pump wavelength of 1.047 μm, the signal wavelength is 1.56 μm, and this provides another way to achieve effective eye safe radiation.

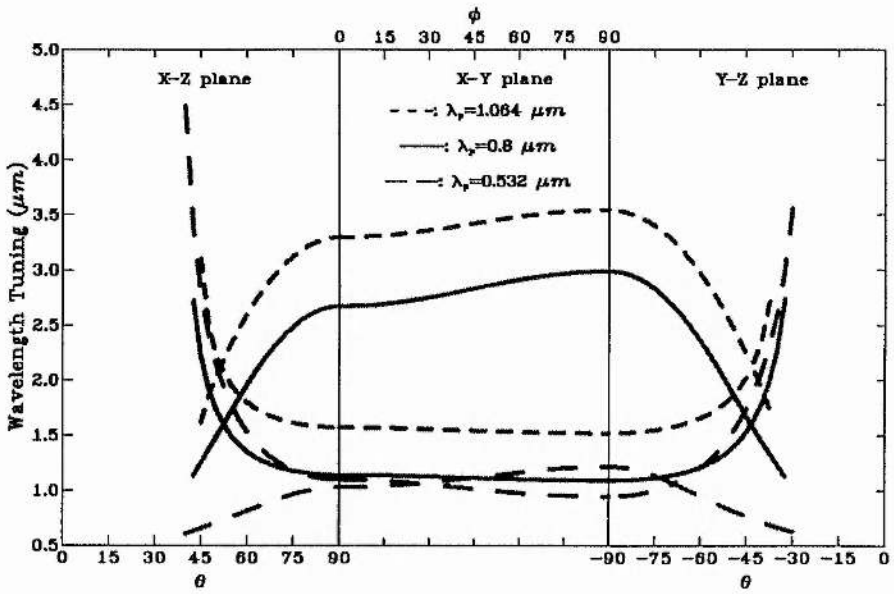

Figure 3.7: Wavelength tuning of KTP OPOs.

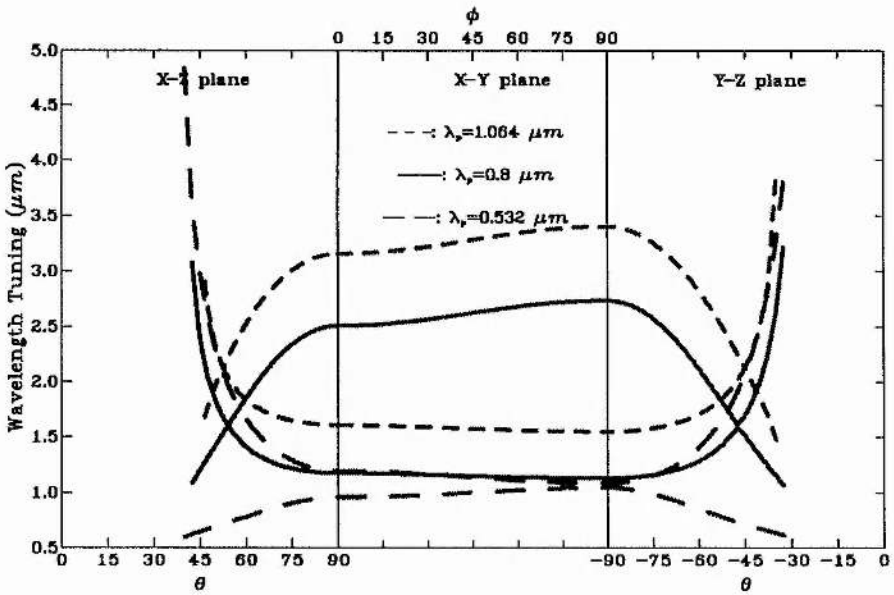

Figure 3.8: Wavelength tuning of KTA OPOs.

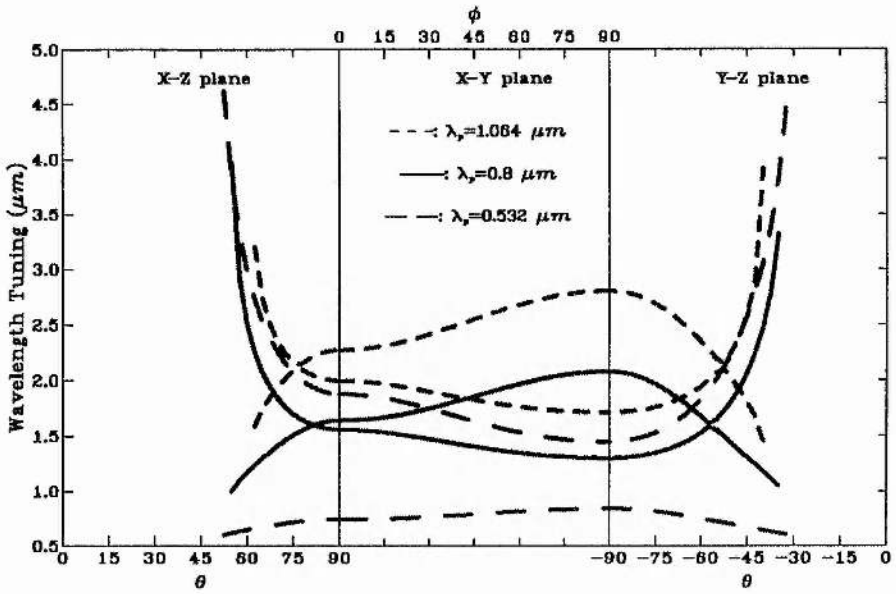

Figure 3.9: Wavelength tuning of CTA OPOs.

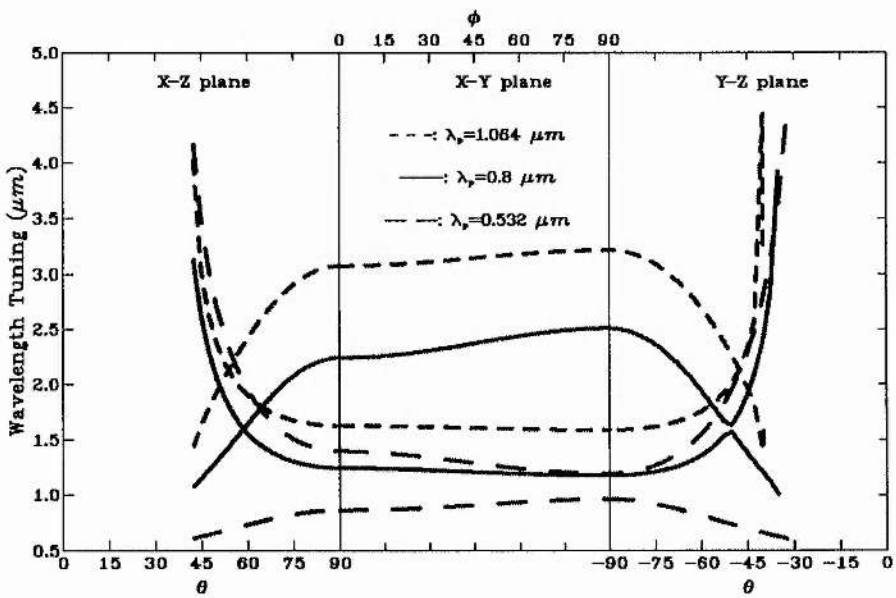

Figure 3.10: Wavelength tuning of RTA OPOs.

3.3 Lithium triborate (LBO)

As one of the most useful nonlinear materials, lithium triborate has displayed many excellent properties, such as high transparency in the near-infrared, visible and uv spectral regions, high optical damage threshold, and moderate nonlinear coefficients. In particular, the transparency out to 0.16 μm and the possibility of frequency up-conversion by non-critical temperature phase-matching over a large spectral range through deep uv to near infrared have opened up prospects for the development of highly efficient frequency up-converters by the use of LBO. To more accurately predict the phase-matching temperatures of LBO for applications, we have measured its thermo-optical coefficients, and the details of the measurement and predictions of some useful non-critical temperature phase-matching geometries are presented in Chapter 6. This section summarises the general properties and angular phase-matching behaviours of LBO.

Crystallographic structure LBO is a biaxial nonlinear optical crystal belonging to the orthorhombic system with point group mm2. The mutually orthogonal principal axes x, y, z (ordered according to increasing refractive index $n_x<n_y<n_z$) correspond to the crystallographic axes a, c, b. The calculated optical angle is 54.6^o at 0.532 μm which defines LBO as a negative crystal [39].

Transmission Optically, the transparency of LBO extends from 160 nm in the ultraviolet region to 2.6 μm in the near infrared region. The absorption coefficients[4] were found to be 0.015/cm and 0.02/cm at wavelengths of λ=1.064 μm and λ=0.355 μm, respectively.

Effective nonlinear coefficient In the piezoelectric axis system, the five non-zero nonlinear optical coefficients of LBO are d_{31}, d_{32}, d_{33}, d_{15}, and d_{24}. Transferring those coefficients into the optical axis system, then the nonlinear susceptibility tensor of LBO with the five coefficients is of the form:

$$\begin{pmatrix} 0 & 0 & 0 & 0 & 0 & d_{15} \\ d_{31} & d_{33} & d_{32} & 0 & 0 & 0 \\ 0 & 0 & 0 & d_{24} & 0 & 0 \end{pmatrix} \tag{3.11}$$

Chen *et al.* have first determined the above five non-zero coefficients for LBO by using the Maker fringe technique[40], and these are (in pm/V): $d_{15} = 0.89$, $d_{24} = 0.98$, $d_{31} = 0.98$,

Table 3.3: The simplified expressions of d_{eff} in LBO

d_{eff} (pm/V)	x-z $0 \leq \theta \leq \Omega$	x-z $\Omega \leq \theta \leq 90^o$	y-z	x-y
d_{eff}(I)	$d_{31}\cos^2\theta + d_{32}\sin^2\theta$	0	0	$d_{32}\cos\phi$
d_{eff}(II/III)	$d_{15}\cos^2\theta + d_{24}\sin^2\theta$	0	$d_{15}\cos\theta$	0

$d_{32} = 1.05$, and $d_{33} = 0.06$. The simplified expressions of d_{eff} for LBO oriented in the three principal planes are summarised in Table 3.3.

Sellmeier equations and thermal dependence of principal refractive indices In early times, a set of Sellmier equations was measured by Chen *et al.*[41], using the least angle deflection method, they measured the three principal refractive indices at 16 wavelengths from λ=1.064 μm to λ=0.2537 μm, but the crystal temperature was not mentioned. Shortly thereafter, a number of Sellmeier equations for LBO were published, and those can be seen in Refs. [43, 42, 44]. Among them, the Sellmeier equations published by Chen[42], and by Kato[44] have been regarded as being in good agreement with experimental results. In particular for short wavelength generation ($\geq$240 nm), the Sellmeier equations presented by Kato[44] gives more accurate predictions than others[45]. To have a set of Sellmeier equations suitable for the deep uv spectral region, Chen *et al.* have made further modifications based on their sum-frequency mixing experiments down to the shortest wavelength of 187.7 nm[42]. In our work, we have adopted the Sellmeier equations given in Ref.[42] through all of the phase-matching calculations.

The birefringence of LBO is very sensitive to temperature. However, the thermal dependencies of the principal refractive indices of LBO was only reported by Velsko *et al.* [43], and their measurements were limited to the temperature range of 20-65°C. To improve this situation we have remeasured these coefficients over a much more extensive temperature range of 20-200°C with a Michelson interferometer. The resulting three formulae of the thermal dependence of the principal refractive indices of LBO from our measurements are given in Chapter 6.

Damage threshold High damage threshold is one of the attractive advantages for LBO. Generally, the damage threshold of LBO is regarded to be 20-25 GW/cm^2 as reported by Chen *et al.* [41], this is more than ten times higher than the damage threshold of KTP.

Phase-matchable regions The calculated wavelength phase-matchable regions for SFG using LBO are plotted in Figs. 3.11-3.13 for type I, II, and III phase-matching geometries respectively. Where the calculation is for the condition of non-zero d_{eff} and with

$$\frac{1}{\lambda_3} = \frac{1}{\lambda_1} + \frac{1}{\lambda_2}.$$

The figures are symmetrical about the diagonal line ($\lambda_2 = \lambda_1$). The isopleths of λ_3 show the possible pump wavelength range and the tuning range of OPOs. For both type I and type II geometries, as shown in Figs. 3.11 and 3.12, there are very large phase-matchable ranges, particular for the type I case, the phase-matchable region nearly covers the whole transparency region. However, because of the small birefringence, the shortest fundamental wavelengths for second-harmonic generation are limited to 0.555 μm in type I phase-matching geometry, and 0.795 μm in type II and type III phase-matching geometries.

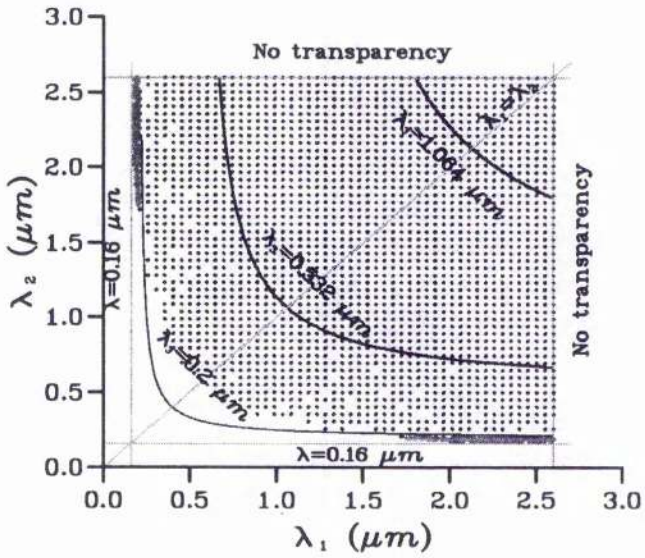

Figure 3.11: Phase-matchable region of TYPE I SFG in LBO.

The dark coloured areas in Figs. 3.11 and 3.12, indicate the possible range of sum-frequency generation in uv and deep uv regions, for which the required input radiations have to be one in the uv region and the other in the infrared. The generated shortest wavelength can be extended to the LBO transmission cut-off, 0.16 μm.

As examples of uv radiation generation, the predicted phase-matching parameters for sum-frequency mixing of the fifth harmonic of Nd:YLF laser (0.213 μm) and the infrared radiation in the range of 1.7-2.6 μm for both the type I and type II phase-matching

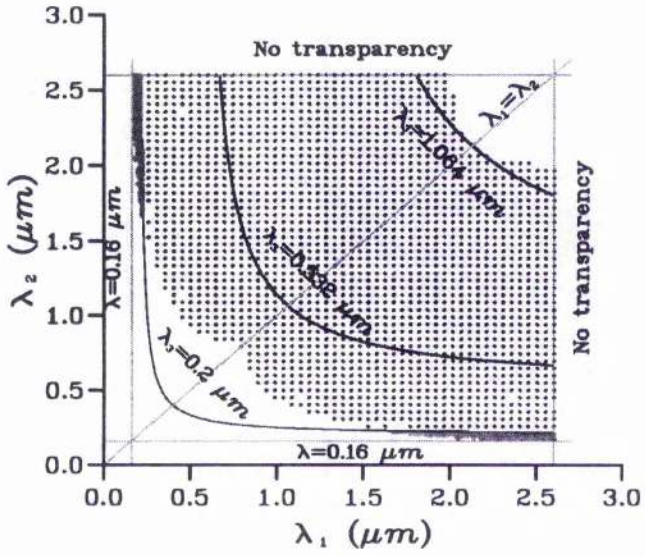

Figure 3.12: Phase-matchable region of TYPE II SFG in LBO.

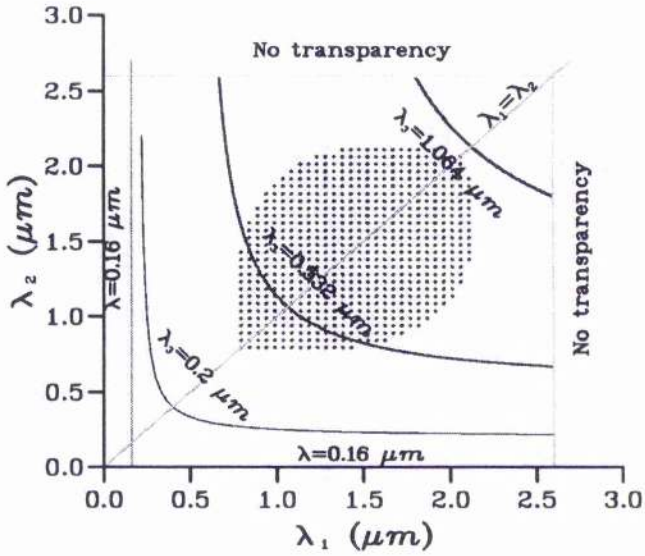

Figure 3.13: Phase-matchable region of TYPE III SFG in LBO.

geometries are given in Figs. 3.14 and 3.15 respectively. We can seen that, with the fixed wavelength λ_1, the tuning range of λ_3 is limited at the short wavelength side by the phase-matching angle of ϕ=90° (*i.e.* where d_{eff}=0) for type I, and by the phase-matching angle of θ=90° (*i.e.* where d_{eff}=0) for type II.

In contrast with the type I phase-matching, the type II phase-matching geometry for uv generation is more attractive because its shows a non-critical phase-matching condition and therefore a relatively high d_{eff}, as shown in Fig. 3.15.

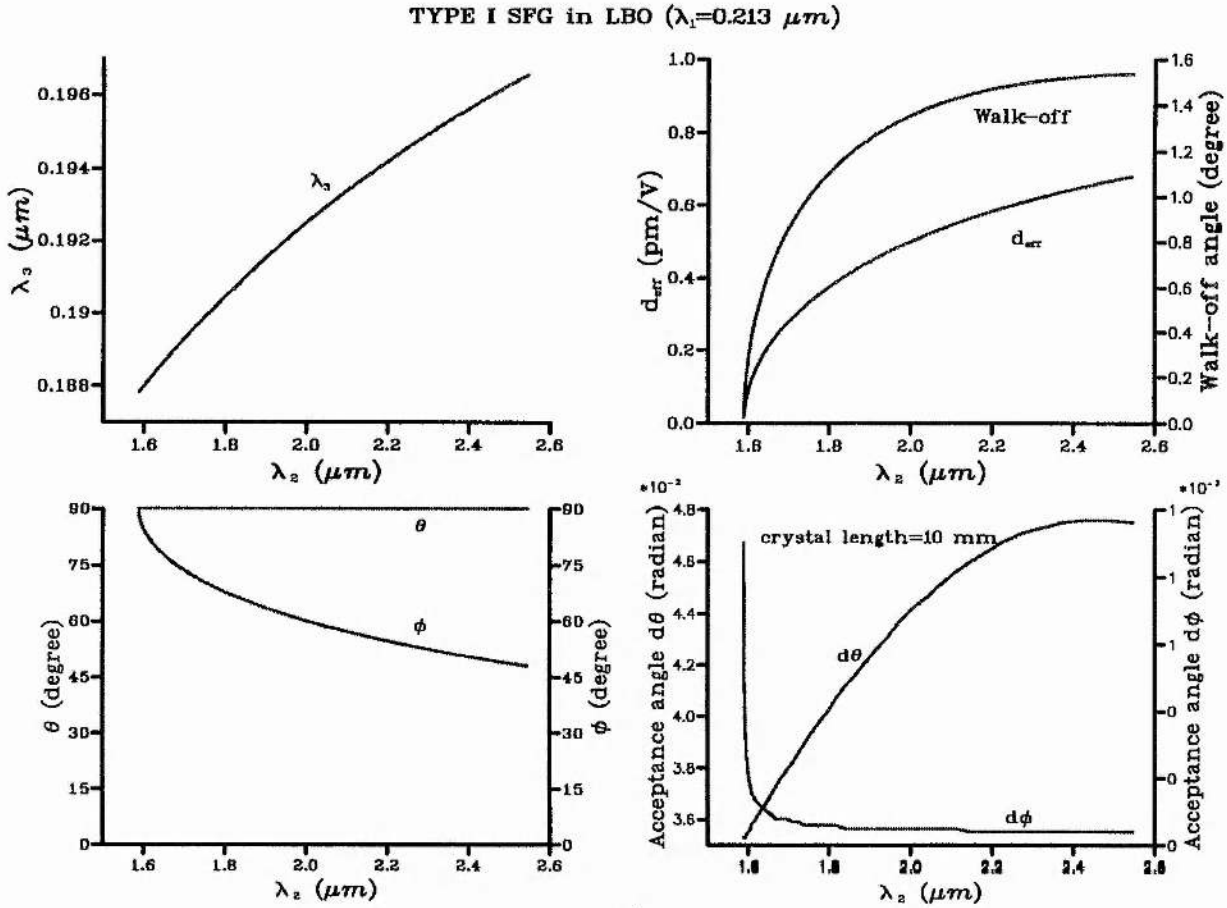

Figure 3.14: Phase-matching properties of TYPE I sum-frequency mixing of 0.213 μm and infrared radiation.

Non-critical phase-matching is one of the important features of LBO. Figs. 3.16-3.18 illustrate the possibilities for type I, type II and type III non-critical phase-matching in LBO at room temperature, where the restriction of $\lambda_1 \geq \lambda_2$ was used in plotting the figures. For type I NCPM SFG in LBO, the beam propagation direction is along the

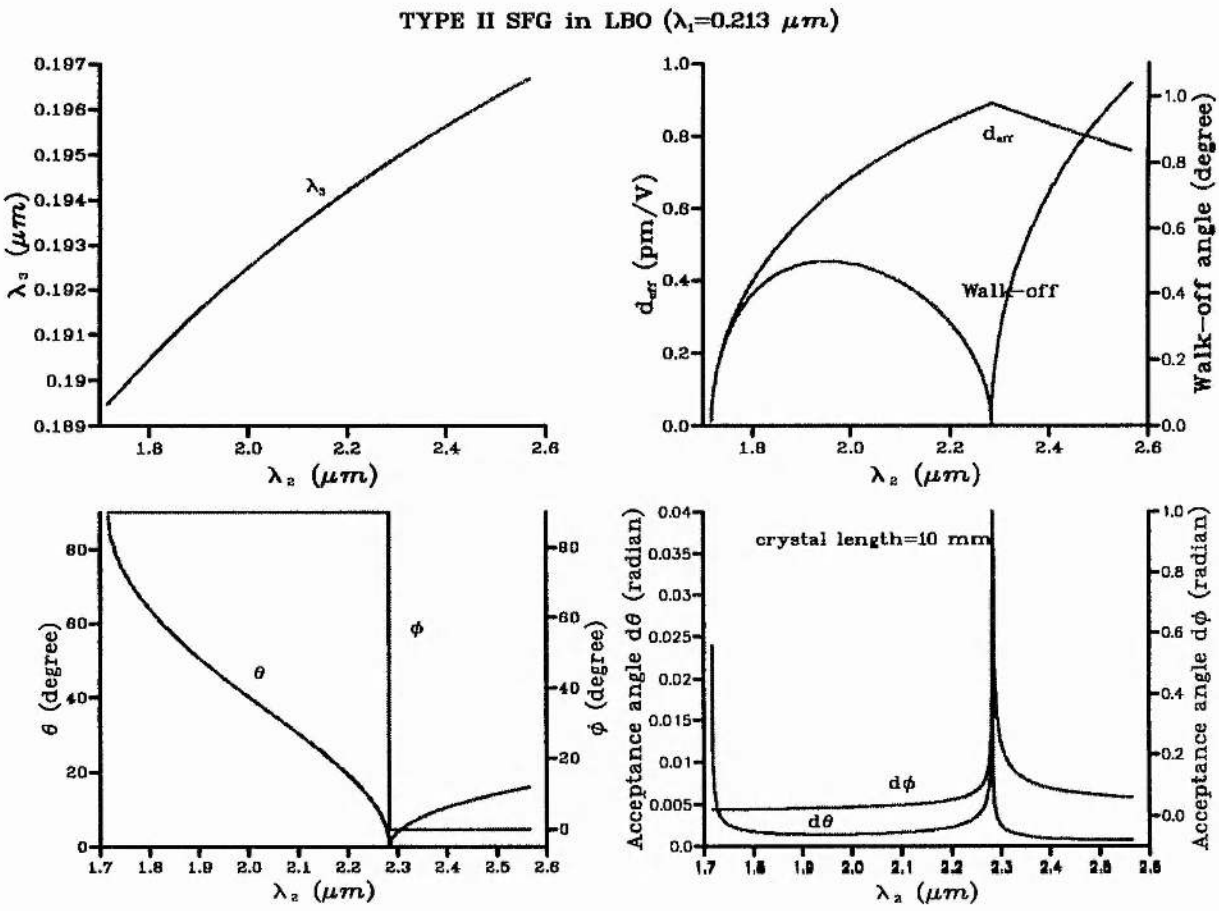

Figure 3.15: Phase-matching properties of TYPE II sum-frequency mixing of 0.213 μm and infrared radiation.

x-axis of the crystal (*e.g.* θ=90°, ϕ=0°.); the polarizations of the input fields are parallel to the z-axis; and the polarisation of the generated field is parallel to the y-axis. In this phase-matching geometry, the allowed wavelength range for λ_1 is 1.19-1.74 μm; and for λ_2 is 0.96-1.417 μm. For type II NCPM SFG in LBO, the beam propagation direction is along the z-axis (*e.g.* θ=0°.); the polarizations of the input field with the longer wavelength and the generated field are parallel to the x-axis; and the polarisation of the second input field is parallel to the y-axis. In this phase-matching geometry, the allowed wavelength range for λ_1 is 1.13-2.6 μm; and for λ_2 it is 0.16-1.49 μm. An attractive feature of the type II NCPM geometry is the possibility of generating radiation at short wavelength. LBO also offers, for type III non-critical phase-matching at θ=0°, when the polarizations of the input field with the shorter wavelength and the generated field are parallel to the x-axis and the polarisation of the other input field is parallel to the y-axis. However, as shown in Fig. 3.18, the phase-matchable range is limited to a small region (1.197-1.404 μm) with the wavelength condition of $\lambda_1 \simeq \lambda_2$.

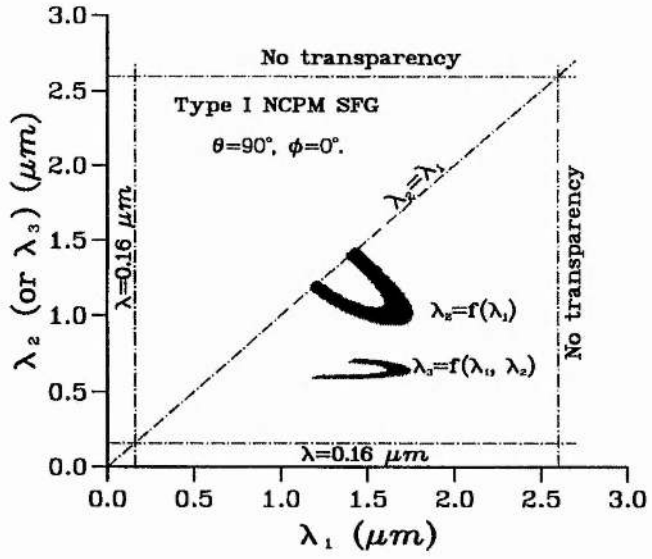

Figure 3.16: Predicted type I non-critical phase-matching in LBO for sum-frequency mixing

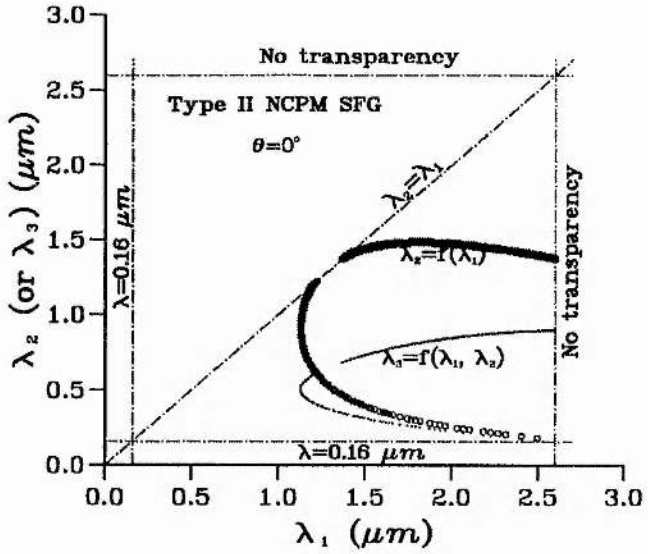

Figure 3.17: Predicted type II non-critical phase-matching in LBO for sum-frequency mixing

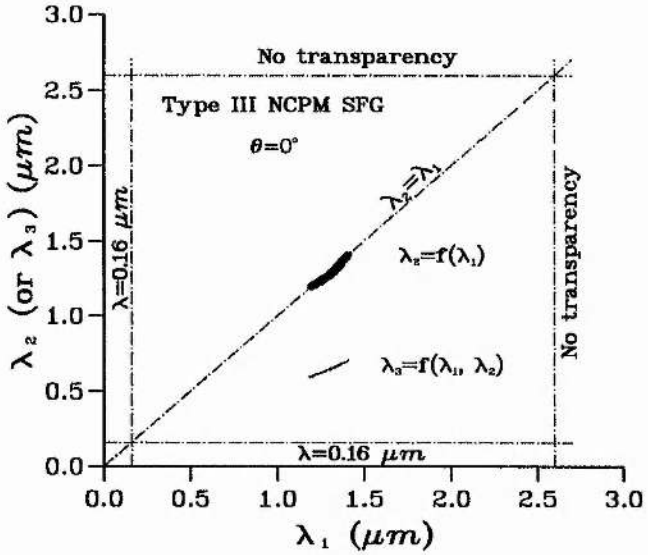

Figure 3.18: Predicted type III non-critical phase-matching in LBO for sum-frequency mixing

Bibliography

[1] D. A. Bryan, R. R. Rice, R. Gerson, H. E. Tomaschke, K. L. Sweeney, and L. E. Halliburton. *Opt. Eng.* **24**, 138 (1985).

[2] D. A. Bryan, R. Gerson and H. E. Tomaschke, *Appl. Phys. Lett.* **44** 847 (1984).

[3] J. L. Nightingale, W. J. Silva, G. E. Reade and A. Rybicki, *SPIE* **681**, 20 (1986).

[4] V. G. Dmitriev, G. G. Gurzadyan, and D. N. Nikogosyan, *handbook of Nonlinear Optical Crystals*, springer-Verlag Berlin Heidelberg 1991.

[5] J. C. Baumert, J. Hoffnagle and P. Gunter, *Proc. SPIE*, **492**, 374 (1985).

[6] G. J. Dixon, Z. M. Zhang, R. S. F. Chang and N. Djeu, *Opt. Lett.* **13**, 137 (1988).

[7] B. Zysset, I. Biaggio and P. Gunter, *J. Opt. Soc. Am. B* **9**, 380-386 (1992).

[8] I. Biaggio, P. Kerkoc, L. S. Wu, and P. Gunter, *J. Opt. Soc. Am. B* **9**, 507-517 (1992).

[9] K. Kato, *IEEE J. Quantum Electron.* **QE-18**, 451 (1982).

[10] C. Chen, B. Wu, A. Jiang, G. You, *Sci. Sin., Ser. B.* **28**, 235 (1985).

[11] D. N. Nikogosyan, *Appl. Phys. A* **52**, 359-368 (1991).

[12] D. Eimerl, L. Davis, S. Welsko, E. K. Graham, A. Zalkin, J. *Appl. Phys.* **62**, 1968 (1987).

[13] F. C. Zumsteg, J. D. Bierlein, and T. E. Gier, *J. Appl. Phys.* **47**, 4980-4985 (1976).

[14] B. Boulanger, J. P. Feve, G. Marnier, B. Menaert, and X. Cabirol, *J. Opt. Soc. Am. B* **11**, 750-756 (1994).

[15] K. Kato, *IEEE J. Quantum Electron.* **QE-27**, 1137 (1991).

[16] J. C. Jacco, G. M. Loiacono, *Appl. Phys. Lett.* **58**, 560 (1991).

[17] D. J. Gettemy, W. C. Harker, G. Lindholm, and N. P. Barnes, *IEEE J. Quantum Electron.* **QE-24**, 2231 (1988).

[18] R. C. Eckardt , H. Masuda, Y. X. Fan, and R. L. Byer, *IEEE J. Quantum Electron.* **QE-26**, 922 (1990).

[19] R. DeSalvo, D. J. Hagan, M. Sheik-bahae, G. Stegeman, E. W. Van Stryland, and H. Vanherzeele, *Opt. Lett.* **17**, 28 (1992).

[20] H. Vanherzeele, *Proc. Soc. Photo-Opt. Instrum. Eng.* **1104**, 44 (1989).

[21] A. J. Brown, M. S. Bowers, K. W. Kangas, and C. H. Fisher, *Opt. Lett.* **17**, 109 (1992).

[22] H. Ito, H. Naito, and H. Inaba, *J. Appl. Phys.* **46**, 3992-3998 (1975). There are typographical errors in the expressions of d_{eff}^{typeI} and d_{eff}^{typeII} for point symmetry $mm2$. The correct fomulare are given in [23].

[23] D. N. Nikogosyan and G. G. Gurzadyan, *Sov. J. Quantum Electron.* **17**, 970-977 (1987).

[24] H. Vanherzeele, J. D. Bierlein, and F. C. Zumsteg, *Appl. Opt.* **27**, 3314 (1988).

[25] T. Y. Fan, C. E. Huang, B. Q. Hu, R. C. Eckardt, Y. X. Fan, R. L. Byer, and R. S. Feigelson, *Appl. Opt.* **26**, 2390 (1987).

[26] K. Kato, *IEEE J. Quantum Electron.* **QE-24**, 3 (1988).

[27] D. W. Anthon and C. D. Crowder, *Appl. Opt.* **27**, 2650 (1988).

[28] J. A. C. Terry, Y. Cui, Y. Tang, W. Sibbett, and M. H. Dunn, *J. Opt. Soc. Am. B* **11**, 758 (1994).

[29] T. A. Driscoll, H. J. Hoffman, R. E. Stone, and P. E. Perkins, *J. Opt. Soc. Am. B* **3**, 683 (1986).

[30] P. E. Powers, S. Ramakrishna, C. L. Tang, and L. K. Cheng, *Opt. Lett.* **18**, 1171 (1993).

[31] P. E. Powers, C. L. Tang, and L. K. Cheng, *Opt. Lett.* **19**, 37 (1994).

[32] D. T. Reid, M. Ebrahimzadeh, and W. Sibbett, *J. Opt. Soc. Am. B* **12**, 1157 (1995).

[33] Herman Vanherzeele and John D. Bierlein, *Opt. Lett.* **14**, 982 (1992).

[34] L. K. Cheng, L. T. Cheng, J. D. Bierlein, and F. C. Zumsteg, *Appl. Phys. Lett.* **62**, 346 (1993).

[35] L. T. Cheng, L. K. Cheng, J. D. Bierlein, and F. C. Zumsteg, *Appl. Phys. Lett.* **63**, 2618 (1993).

[36] L. K. Cheng, L. T. Cheng, and J. D. Bierlein, *Proc. SPIE* **1863**, 43-53 (1993).

[37] K. Kato, *IEEE J. Quantum Electron.* **QE-30**, 881 (1994).

[38] P. E. Powers, S. Ramakrishna, and C. L. Tang, *Opt. Lett.* **18**, 1171-1173 (1993).

[39] J. T. Lin, J. L. Montgomery, and K. Kato, *Opt. Commun.* **80**, 159 (1990).

[40] S. Lin, Z. Sun, B. Wu, and C. Chen, *J. Appl. Phys.* **67**, 634 (1990).

[41] C. Chen, and Y. Wu et al, *J. Opt. Soc. Am. B* **6**, 616 (1989).

[42] B. Wu, N. Chen, C. Chen, D. Deng, and Z. Xu, *Opt. Lett.* **14**, 1080 (1989).

[43] S. P. Velsko, M. Webb, L. Davis, and C. Huang, *IEEE J. Quantum Electron.* **QE-27**, 2182 (1991).

[44] K. Kato, *IEEE J. Quantum Electron.* **QE-26**, 1173 (1990).

[45] A. Borsutzky, R. Bringer, and R. Wallenstein, *Appl. Phys.* **B52**, 380-384 (1991).

Chapter 4

Pump source

In this work, two diode-pumped Q-switched Nd:YLF lasers were used for the experiments. The first one was an electro-optically (EO) Q-switched Nd:YLF pulsed laser; and the second one was an acousto-optically (AO) Q-switched slab-geometry Nd:YLF *cw* laser. Both lasers were developed in this group, and developing a second version of the acousto-optically (AO) Q-switched end-pumped Nd:YLF laser was a specific part of this research program. In this chapter, we describe the operation of the two pump lasers and the design considerations of the second AO Q-switched laser.

Q-switch: Since the efficiency of parametric interaction is strongly dependent on the pump intensity, normally a SRO requires a Q-switched laser as the pump source, in which the laser is switched rapidly from a lossy state to a low loss state, whilst the laser medium is being continuously excited. This has the effect of storing energy in the lossy state, and releasing the energy in a short, high energy pulse when the loss is removed. There are several methods for switching cavity loss, among them, EO Q-switching for pulsed lasers and AO Q-switching for *cw* lasers are the most commonly used techniques.

Nd:YLF: Nd:YLF is the best choice for Q-switched neodymium lasers. This is primarily because Nd:YLF has a longer energy storage time, which is 0.48 msec, twice as long as the 0.24 msec of Nd:YAG. With a constant amount of energy coming into the laser material, the material that can store energy for the longest time will be the one with the most energy in the pulse. For instance, Grossman *et al.* [1] has reported that approximately twice the pulse energy can be obtained from a Q-switched Nd:YLF laser than from a Q-switched

Nd:YAG laser, due to the difference in the fluorescence lifetime for these media. A drawback of Nd:YLF is its low thermal conductivity, it is approximately a factor of two lower than that of Nd:YAG. Hence the thermal fracture will be a problem for the Nd:YLF laser when pumped at high power. In addition, Nd:YLF is also slightly harder to handle and fabricate than Nd:YAG and is only available in small sizes. As we know, diode-pumped lasers do not need big pieces of anything and provide moderate energy for pumping, so that Nd:YLF is superior to Nd:YAG for diode-pumping in almost all applications where its natural birefringence is not a problem.

Diode-pump laser: Over the last ten years, the technique of diode-pumping lasers has become very important, particular in the laboratory because it enables the development of solid-state lasers that are more efficient, compact, and have good beam quality. In the report given by Fan[2], the advantages of diode-pumped lasers compared to lamp-pumped lasers can be summarised as follows:

1. Much more efficient utilisation of the pump radiation can be achieved because that diode lasers have narrow band spectral output and can be tuned directly onto an absorption feature.
2. Less heating from the diode-pumped laser because the average pump photon has a higher energy in lamp pumping than in diode pumping.
3. The output of the diode laser can be focused to a small cross sectional area to produce a high pumping density.

4.1 The electro-optically (EO) Q-switched Nd:YLF laser

A schematic of the EO Q-switched Nd:YLF laser system is depicted in Fig. 4.1. The laser was formed symmetrically by two quasi-*cw* diode lasers and two a-cut Nd:YLF rods. Each diode laser is capable of delivering a maximum energy of 72 mJ in a pulse of 400 μs.

Basically, the diode light was collimated by a combination of rod and cylindrical lenses and then focused to a spot at a short distance inside the Nd:YLF crystal by using an aspherical condenser lens. Using this lens combination, a 85% pump light transmission into an elliptically focused spot have been reported[3].

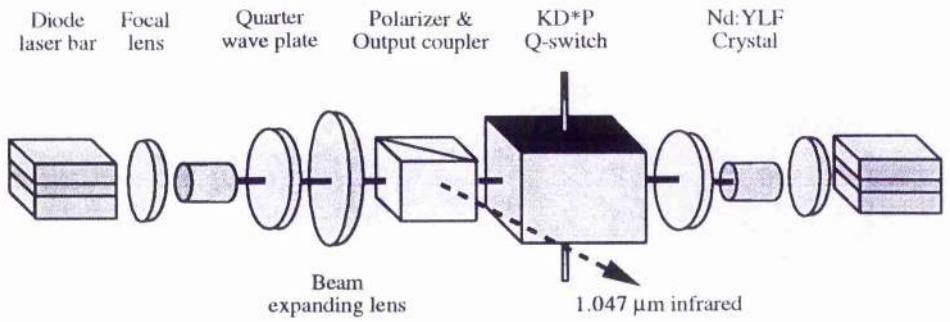

Figure 4.1: Schematic diagram of the EO Q-switched Nd:YLF laser

The Nd dopant density was 1% at.wt, which gives a peak absorption coefficient of $\geq$6.5 cm^{-1} at 797 nm, when the crystal was pumped with the diode light polarized along the crystallographic c axis. The Q-switching operation with 14 Hz repetition rate was achieved through the use of a lithium niobate electro-optical crystal in conjunction with an air-spaced cube polarizer, the Q of the cavity being switched from low to high by removing the $\lambda/4$ field (1.6 kV) applied to the crystal during the pump pulse.

This laser could provide a maximum of 6 mJ output in a 10 ns pulse width, when the corresponding peak power was 600 kW. This was sufficient power to carry out all experiments for the first stage of the KTP OPOs. The measured output pulse energy and pulse width of this laser as a function of diode current are plotted in Fig. 4.2.

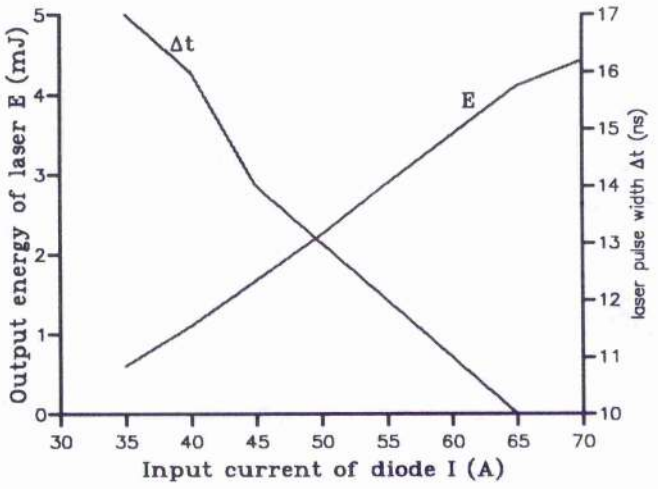

Figure 4.2: The output energy and pulse width of the EO Q-switched Nd:YLF laser.

The temporal pulse profile was measured by using a vacuum photo-diode and the pulse

width was found to be dependent on the current through the laser diode. For instance, at the full maximum current (70A), the laser pulse width was 10 ns, but it was 15 ns at the diode current of 45 A. The beam spatial profile was measured by a CCD camera and the beam quality was characterised by the factor M^2 (number of times the diffraction limit), and found[1] to be M^2=1.1.

4.2 The acousto-optically (AO) Q-switched Nd:YLF laser

A schematic of this laser system is depicted in Fig. 4.3. The laser contains a slab-like Nd:YLF crystal, two 20 W GaAlAs *cw* laser diodes, and the focusing optics.

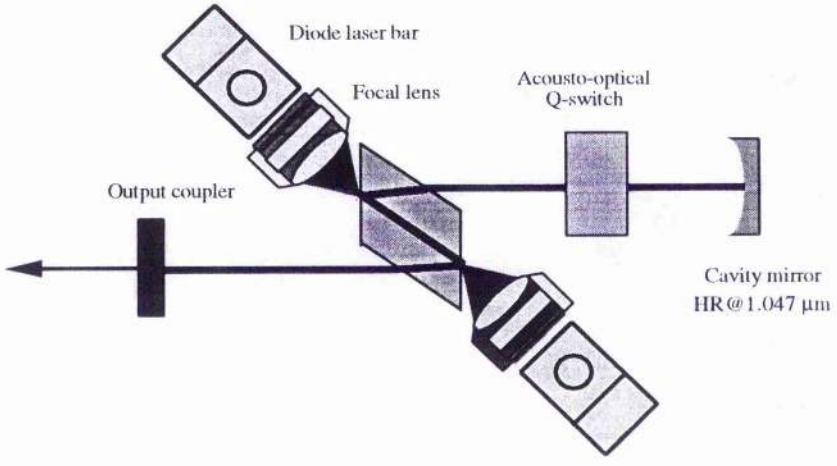

Figure 4.3: Schematic diagram of AO Q-switched Nd:YLF laser.

The slab-like pump configuration was initially reported by P. Albers, C. Pfistner and H. P. Weber [6, 7] for diode end-pumping of Nd:YAG lasers. Using Nd:YLF as the alternative laser medium, the first laser was developed in this group by Christian Rahlff. Fig. 4.4 illustrates the pump scheme of the slab-like geometry. The crystal was cut to allow its c-axis to be parallel to the surface of the slab, with the laser field propagating along the a-axis as shown in Fig. 4.4. Effective optical pumping is then possible, if the polarization of the pumping E-field is parallel to the crystal's c axis and the polarization of the laser field is also parallel to the $a-c$ plane. Another advantage of this pump scheme is the use of Brewster-angled entrance faces at the two sides of the Nd:YLF crystal which makes

[1]The method of M^2 measurement is[4, 5]: a waist was created, with the help of a converging lens, and its spot size w_1 is measured. A lens of focal length f was then placed after the waist and the beam spot size w_2 at the back focal plane of the lens was recorded. The beam quality is given then by $M^2 = \pi w_1 w_2/\lambda f$.

coating of the entrance surfaces unnecessary and results in a zero loss for the resonated electrical field component in the incident plane. The crystal dimensions were 7.2 mm × 6.7 mm × 1 mm, and the coatings on the two side faces (1 mm×6.7 mm faces) of the slab were specified as:

1. HR for 1047 nm at an angle of incidence of 27.9°.
2. HT for 798 nm at an angle of incidence of 43.4°.

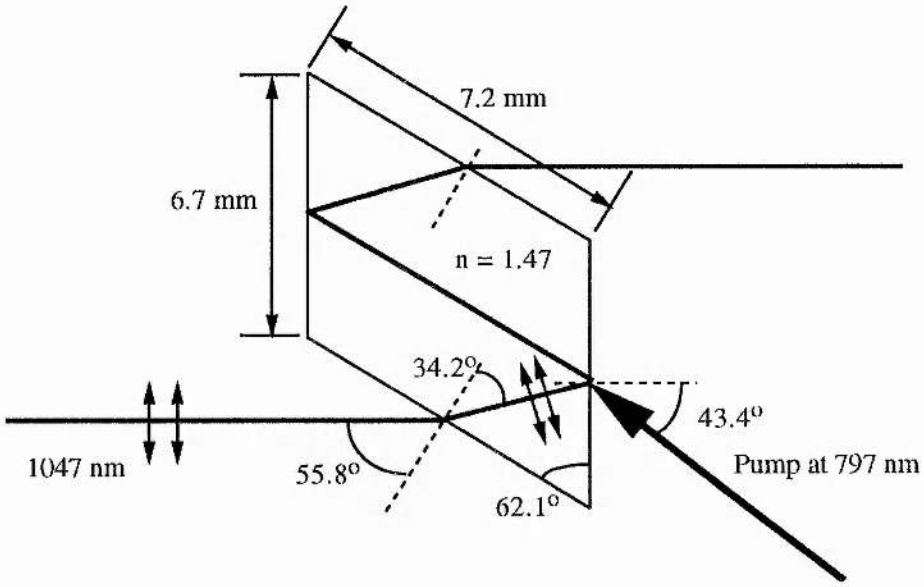

Figure 4.4: The slab-like geometry.

The performance of the first slab-like Nd:YLF laser showed several desirable features including highly efficient operation, good mode quality and ability to be Q-switched to produce high repetition rate pulses (up to ~20 kHz). In the case of *cw* operation, the maximum output power was reported to be 6.5 W in TEM_{00} spatial mode ($M^2 = 1.6$) when pumped at 20 W [8]. In the case of AO Q-switched operation, the maximum peak power reached can be 30 kW with 25 ns pulse width.

For the purpose of enhancing the nonlinear optical frequency conversion on this laser, it was decided to construct a second laser. Basically, the development of the second laser used the same pump geometry as the previous design, but to make it more compact and flexible to control and use, the cooling system and the whole mechanical structure of the laser were re-designed as given in the following sections.

4.2.1 Pump optics and pump module design

The diodes used for the second laser were supplied by OPTO POWER CORPORATION (OPC). The emitting aperture of the diode was 10 mm $\times$ 1μm, and the typically beam divergence were 30~40^o along the y axis, and 10^o along the x axis.

As reported by Kane [9], the maximum gain and efficiency will be achieved when the laser mode includes as much as possible of the region where the pump light is absorbed, and when both the pump beam and the laser mode have a small diameter in that region. The pump absorption region for Nd:YLF is 3 $\sim$ 4 mm long. However, as we know a tightly focused beam while very small at its focus diverges quickly compared to a weakly-focused beam which hardly diverges at all but is never focused to a small spot. So, the basis of the pump optics is to find the optimum trade-off between weak and tight focusing.

A pump light coupling technique presented by Shannon and Wallace[10] was found particular success for the diode-laser bar having the size of 10 mm $\times$ 1μm. In this pump scheme, diode light is collimated in the high-divergence plane by using a rod lens/cylindrical lens combination and then focused to a spot a short distance inside the Nd:YLF crystal by using an aspherical condenser lens (see[2] Fig. 4.5). This pump light coupling technique has been used in our laser system, where the diameter of the rod lens was chosen to be 1.2 mm, the focal lengths of the cylindrical lens and the aspherical lens were chosen to be 12.7 mm and 8.5 mm respectively.

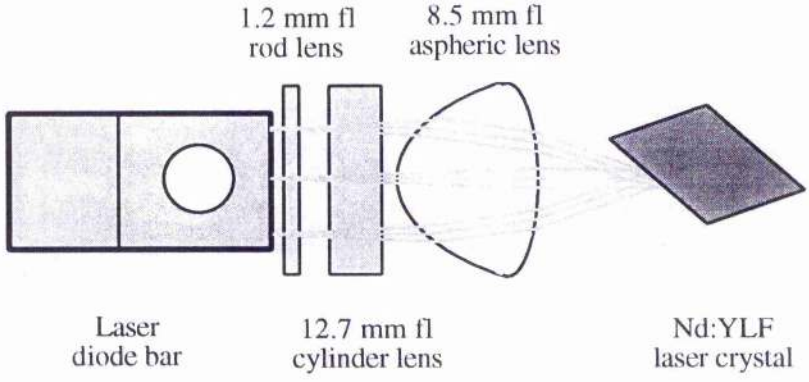

Figure 4.5: Pump optics.

The integrated fluorescence profile in the first laser was approximately 1.2 mm x 0.6 mm. However, much wider fluorescence profiles were found in the second laser. This, we believe, was due to the poor quality of the diodes supplied by OPC [the diodes used for the first

[2]where the aspherical lens is reversed from the way given by Shannon *et al.*

laser were supplied by Spectra Diode Labs (SDL)]. A subsequent change to using a diode supplied by SDL for the second laser has proved our suspicions. Even when only one diode was changed, much improvement in the integrated fluorescence profile with more output power and narrower pulse width was observed.

Moreover, another problem was found from the diode test, namely that the output wavelength of the diodes supplied by OPC was very sensitive to temperature and pump current particularly at low output power operation of the diode ($\leq$ 5 W). This will certainly affect the practical reliability of diode operation.

To improve the fluorescence profile in the Nd:YLF slab of the second laser, we tried to adjust the space in between the lenses and found the best placing of the three lenses given the restricted space condition to be the following:

1. Reasonable freedom distance between rod lens and diode laser aperture.
2. The optimum distance between rod lens and cylindrical lens is 1mm $\pm$ 0.5 mm.
3. The cylindrical lens and condenser lens should be as close as possible, the condenser lens is reversed from the way given by Shannon *et al.* as shown in Fig. 4.5.

A difficulty of this pump scheme was the restricted space. To avoid the folded resonator path being obscured by the pump module, we successful designed a compact assembly which was easy to control and to adjust precisely. The mechanical three dimensional view of this assembly is shown in Fig. 4.6, it has the following properties:

1. The optical focusing block is independently moveable in the vertical direction.
2. Placed on a Peltier cooling block, the diode is independently moveable in the forward and backward-going directions to fine adjust the gap between the diode and the optics which is very sensitive for coupling the diode radiation into the slab.
3. The assembly constructed with the optics and diode blocks is moveable in three dimensions relative to the pumping surface of the slab, *i.e.* the parallel, height and distance movements.

4.2.2 Cooling system improvement

The cooling block has been improved by changing to a Peltier cooler. For the *cw* 20 W diode bar, there was a large amount of heat to remove. However, the tight space of the

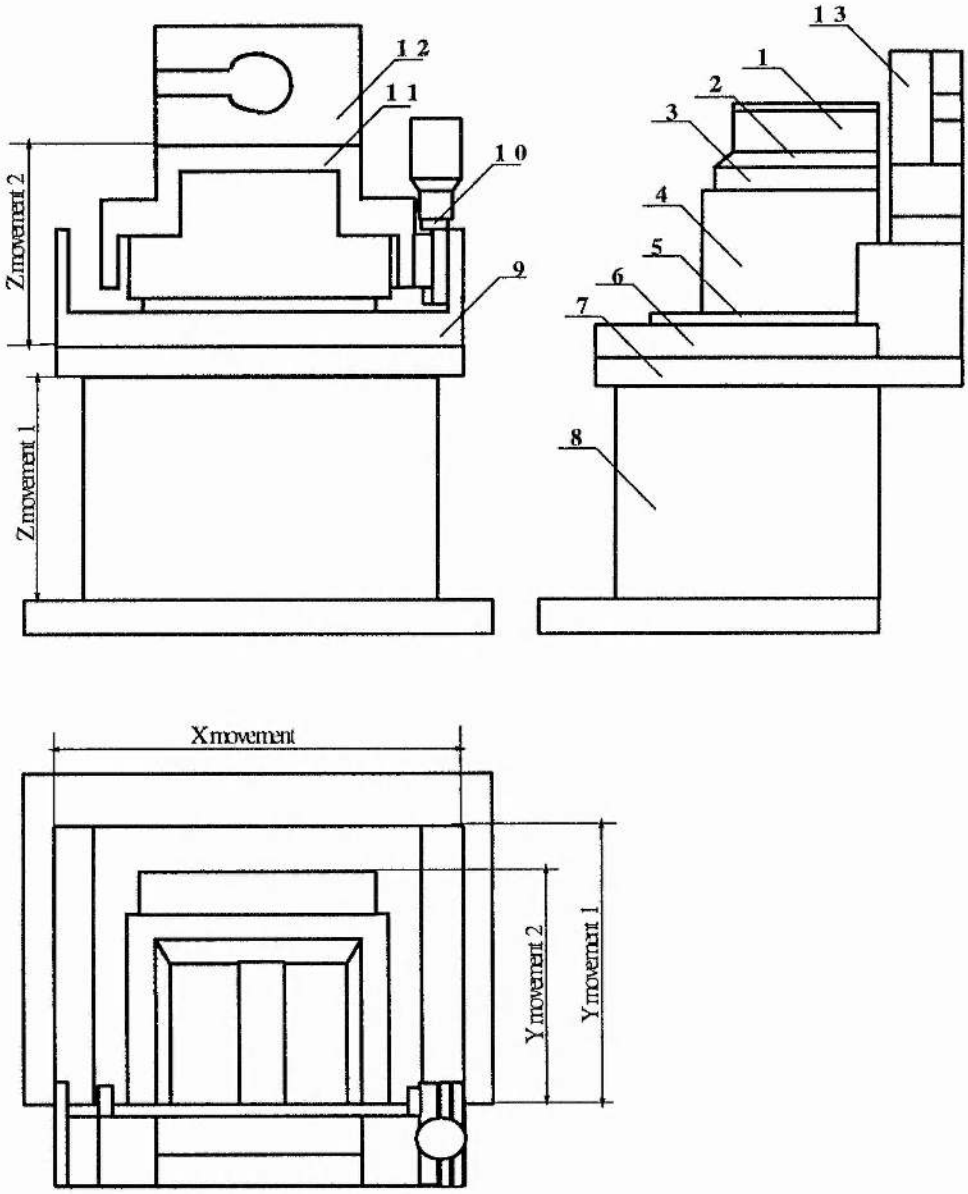

Figure 4.6: Assembly drawing of pump optics and diode laser mount, where: 1. Diode laser; 2. Cooling plate; 3. Peltier cooler; 4. Cooling block; 5. Plate I (for fixing purpose); 6. Y movement translation stage; 7. Plate II (for fixing purpose); 8. Three dimension translation stage; 9. Mount I; 10. Z movement translation stage; 11. Mount II; 12. Aspherical lens holder; 13. Cylindrical lens holder.

pump module as shown in Fig. 4.6, prevented using a large size Peltier. To increase the cooling ability while using a small size Peltier, we designed a special water cooling block, in which the cooling surface was increased by several fins. The temperature of the circulated cooling water was controlled to be constant within ± 0.1 °C. The size of the Peltier used in this system was 30 x 30 mm, which only required 5A maximum driver current. Even at maximum pump, the diodes can be maintained stable at their operation temperatures which were 25.6 °C and 19.5 °C respectively. The slab was cooled by tap water at 14 ^oC from a separate cooling tank.

4.2.3 Laser cavity

Two considerations should be addressed in cavity design:

1. Good mode overlap between the laser and pump beams inside the Nd:YLF slab.
2. Thermally-insensitive.

As reported by Christian Rahlff [11], an ideal cavity to meet the above requirements is a plano-concave one, where the plane mirror was used for the output, and the concave mirror was used for the rear end of the cavity. The cavity length was limited to a minimum of 200 mm. From cavity calculations for the case of using a 500 mm concave mirror, we know that the waist of the laser beam was ω_o=0.3 mm, located very close to the output end of the cavity.

4.2.4 Operational properties

The optimum output coupling for the first laser was found to be 30%. However for the second laser, it was found to be only 20%. Again, we believe, this was due to the poor fluorescence profile from the diodes supplied by OPC. When both sides were pumped at about 5 W, the typical output was a 45 ns pulse width and 1 W average power at the Q-switch repetition rate 2 kHz. The corresponding peak power was less than 8 kW. After change to use one diode supplied by Spectra-Physics, the optimum output coupling was found to be 30%. Much improvements of laser operation were observed in this case. For instance, with 5 watts pumping from both sides and with 1 kHz Q-switching repetition rate, the average output power was 0.5 watts, and the pulse width was observed to be 20 ns. The corresponding peak power was now more than 20 kW.

Bibliography

[1] Grossman W M, Gifford M and Wallace R W, *Opt. Lett.* **15**, 622 (1990).

[2] R. C. Eckardt, H. Masuda, Y. X. Fan, and R. L. Byer, *IEEE J. Quantum Electron.* **26**, 922 (1990).

[3] C. F. Rae, J. A. C. Terry, B. D. Sinclair, M. H. Dunn, and W. Sibbett, *Opt. lett.* **17**, 1673 1992.

[4] Giulio Cerullo, Sandro De Silvestri and Vittorio Magni, *Opt. Commun.* **93**, 77-81 (1992).

[5] M. W. Sasnett, *The physics and technology of laser resonators,* Adam Hilger, Bristol, 132-142 (1989).

[6] P. Albers, C. Pfistner, H. P. Weber, CMF4, CLEO'90.

[7] B. Neuenschwander, P. Albers, H. P. Weber, *Optical and Quantum Electron.* **24**, 363 (1992).

[8] C. Rahlff, M. H. Dunn, B. D. Sinclair, W. Sibbett, CThG4, CLEO'94.

[9] Thomas J. Kane, *Laser Diode-Pumped Solid-State Lasers*, Lightwave Electronics Corporation, Partial revisions, (1993).

[10] D. C. Shannon and R. W. Wallace, *Opt. Lett. 16*, 318 (1991).

[11] Christian P. Rahlff, *Design of a cw Nd:YLF laser*, RARDE report, 16, (1992).

Chapter 5

KTP OPO

The initial aim of this work was to explore the feasibility of developing KTP OPOs based on NCPM geometry, and which would operate at low pump energies and with high efficiency. A key to developing these devices in the NCPM geometry is that under these circumstances walk-off between the pump and generated waves is not present, so allowing long interaction lengths. The realisation however, that only the idler wave is extraordinary in the 1 μm pumped CPM KTP OPO, enabled this work to be extended to consider this geometry also, and to establish how the OPO performance would be affected by the walk-off. Theoretically, based on our extended models given in Chapter 2, we have numerically studied the detrimental effects of Poynting vector walk-off on pump threshold and conversion efficiency. We have also studied other factors influencing the conversion efficiency of the device and found output coupling in particular to be an optimizable parameter which must be well matched to the given pump intensity. Experimentally, to overcome the problem of high pump threshold in the CPM OPO, four pump configurations have been investigated, these were:

1. single-pass-pump.
2. double-pass-pump.
3. cylindrical focusing.
4. intracavity OPO.

Finally, the expected result of a low pump threshold ($\leq$0.6 mJ) with high efficiency ($\eta \approx$ 40%) and wide wavelength tunability was demonstrated with the use of the double-pass-pump configuration.

In the following sections we begin with a description of the design considerations, and then present experimental results using the four pump configurations.

5.1 Design considerations

In this section, we discuss some considerations on crystal design and focusing conditions for the pump and signal beams.

5.1.1 Crystal design

Crystal orientation: As has been discussed in Chapter 3, KTP is type II and type III angular phase-matchable over its three principal plane, *i.e.*, x-y, x-z and y-z planes. To illustrate the optimum phase-matching condition for the 1.047 μm pumped KTP OPOs, the predicted wavelength tuning curves, and the associated behaviours of the effective nonlinear coefficient, walk-off, acceptance angles and spectral linewidth are shown in Figure 5.1 (a)-(d).

As shown in Figure 5.1 (a) and (d), in the x-y plane, KTP offers type III phase-matching, with a slow tuning rate but narrow signal linewidth, and where the pump and signal are extraordinary waves, and the idler is an ordinary wave. These characteristics make the x-y plane less attractive than the other two, except when a narrow linewidth is required.

In both the x-z and y-z planes, KTP displays similar phase-matching behaviour where the degenerate point in each plane divides the phase-match geometry into two types. One is called type II phase-matching where the pump and idler are ordinary waves and the signal is extraordinary. The other one is called type III phase-matching, where the pump and signal are ordinary waves and the idler is extraordinary. The tuning rate near the degenerate point is ~67nm/degree.

(a)

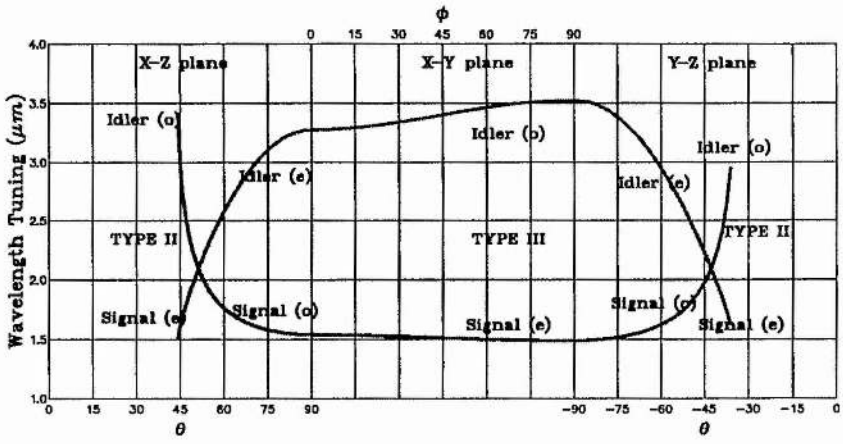
φ
X–Z plane
X–Y plane
Y–Z plane
Wavelength Tuning (μm)
Idler (o)
Idler (e)
Idler (b)
Idler (o)
Idler (e)
TYPE II
TYPE III
TYPE II
Signal (e)
Signal (o)
Signal (e)
Signal (o)
Signal (e)
θ
θ

(b)

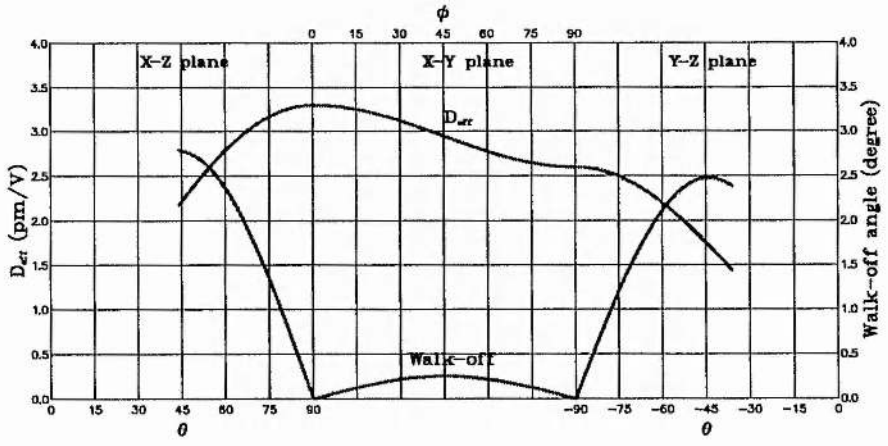
φ
X–Z plane
X–Y plane
Y–Z plane
D_{eff} (pm/V)
Walk–off angle (degree)
D_{eff}
Walk–off
θ
θ

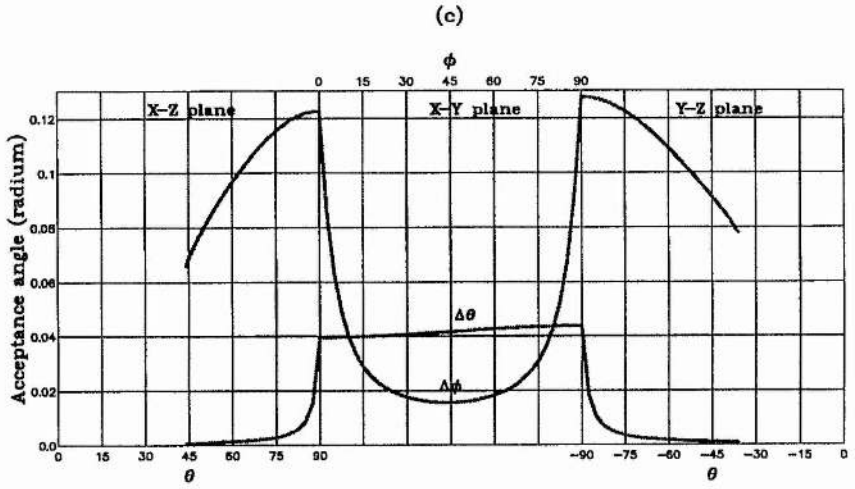

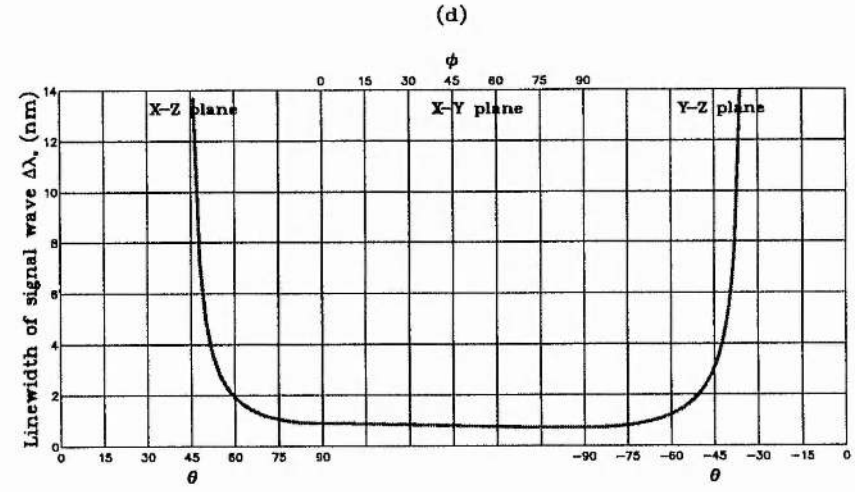

Figure 5.1: Phase-matching properties of the KTP based OPO pumped at 1 μm. (a) Wavelength tuning; (b) Effective nonlinear coefficients and walk-off angle; (c) Acceptance angles; (d) Line width of the signal wave.

Because, as shown in figure 5.1 (b), the effective nonlinear coefficient goes to a maximum at the point θ=90°, ϕ=0° (x axis), and has a relatively higher value in the x-z plane, we have therefore restricted our consideration to the x-z plane.

Table 5.1: Parameters of type III phase-matched KTP OPO

Parameter	NCPM KTP	CPM KTP
orientation (θ, ϕ)	(90^o, 0^o)	(63.4^o, 0^o)
phase-matching type	$\omega_p^o = \omega_s^o + \omega_i^e$	$\omega_p^o = \omega_s^o + \omega_i^t$
d_{eff} (pm/V)	3.3	2.89
Walk-off (degree)	0	2.18
$\Delta\theta$ (radian)	0.04	0.0016
$\Delta\phi$ (radian)	0.12	0.1
$\Delta\lambda_s$ (nm)	0.887	1.5
$\lambda_p(\mu m)/n_p$	1.0470/1.74805	1.0470/1.74805
$\lambda_s(\mu m)/n_s$	1.5388/1.73695	1.6976/1.73404
$\lambda_i(\mu m)/n_i$	3.2759/1.77168	2.7318/1.77061

Hence the KTP crystals used in this work were, one cut at θ=90^o, ϕ=0^o named the NCPM KTP; the other one cut at θ=63.4^o, ϕ=0^o named the CPM KTP. One purpose of the CPM KTP orientation was to achieve a signal output tunable around 1.7 μm, since this to be used in a further stage of sum-frequency mixing in LBO to generate tunable red light.

The calculated phase-matching parameters for both the CPM and NCPM KTP OPOs, which will be used frequently in the later analysis, include: d_{eff}, walk-off, acceptance angle, wavelengths of signal and idler pairs, and their refractive indices. They are listed in Table 5.1 for convenience.

Crystal length: The feature of zero walk-off in the NCPM KTP OPO, and only idler wave walk-off in the CPM KTP OPO, suggests using long crystals to increase gain to reduce pump threshold and increase efficiency. However, too long a crystal will induce back-conversion and small angular acceptance which in turn limits the beam focusing. To establish the optimum crystal length, the pump threshold curves as functions of crystal length and beam-size were calculated and are shown in Figure 5.2. Clearly, little advantage is to be gained in increasing the crystal length beyond 25 mm for the purpose of reducing pump threshold in both the NCPM and CPM OPO geometries. Therefore, both crystals were decided to be 25 mm long with aperture of 5×5 mm^2. The crystals used in our work were supplied by the Shandong University.

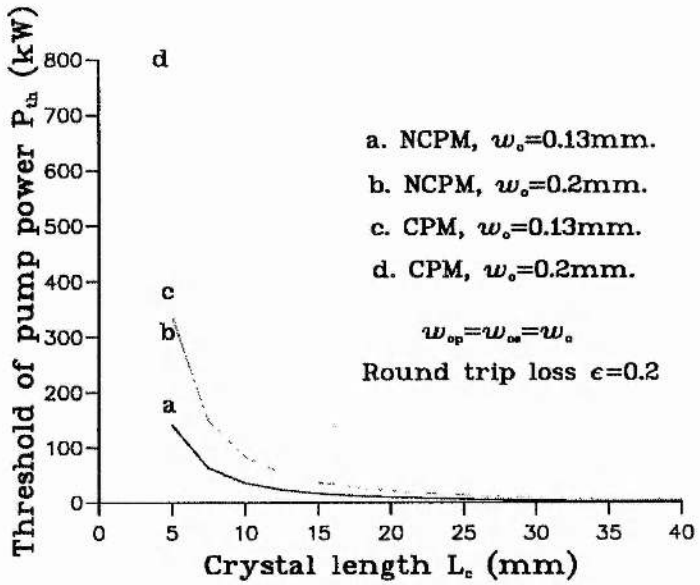

Figure 5.2: Pump threshold of KTP OPOs as a function of crystal length.

5.1.2 Beam focusing

Damage threshold and focusing limitation: The surface damage threshold of KTP is pulse duration dependent [1] as it has been mentioned in Chapter 3. For a high efficiency OPO, any surface damage to the KTP is in fact normally caused by the signal wave intensity rather than pump, due to resonant enhancement of the signal wave intensity inside the OPO cavity. For example, when an OPO is formed with a 20% output coupler, and operates at 30% conversion efficiency, then the circulating signal wave intensity inside the OPO will be 1.5 times higher than the pump intensity, if one assumes equal spot sizes of pump and signal beams. In practice, both beam intensities must be limited to below the damage threshold. From our experimental experience, the pump intensity should be kept below 600 MW/cm^2. Therefore, for the case of the EO Q-switched laser pumped OPO, (where the maximum output power is 6 mJ within a 10 ns pulse width, the corresponding peak power being 600 kW), the limitation on the focused pump waist size is **0.18mm**; and it is **0.04mm** for the case of using the AO Q-switched laser (where the maximum pump peak power is 30 kW).

Optimum focusing and $h_{sm}(\xi, B)$ function: The matching of the pump and signal beams to enable the greatest power transfer from the pump to the signal and idler waves

is very important in a parametric interaction process, and can be measured by the optimizable parameter h_s as introduced and described in Chapter 2. The parameter is a function of beam focusing and double refraction, and has a single maximum at the point of optimum focusing, ξ_m. The value of h_s can be numerically calculated from Eq.(2.107) for a forward-going pump and from Eq.(2.114) for a backward-going pump.

Figs. 5.3 and 5.4 show how the h_{sm}^{+} function in a KTP OPO varies as a function of beam focusing for the forward-going pump in both NCPM and CPM geometries, where the subscript m denotes that h_s has been maximized with respect to the phase-mismatch $\Delta k l_c$, where the crystal length l_c was chosen to be 25 mm; where ξ_s and ξ_p are focusing parameters of signal and pump waves, and B represents the walk-off parameter (B=0 in the NCPM KTP OPO, B=6.6 in the CPM KTP OPO.); and where k is the ratio of wave numbers, $k = k_p/k_s$ (k=1.487 in the NCPM KTP OPO, k=1.651 in the CPM KTP OPO.). For the NCPM KTP OPO, the maximum value of h_{sm}^{+} is 0.3, as shown in Fig. 5.2, which appears at $\xi_p \approx 2.8$, $\xi_s \approx 2.8$; the corresponding beam spot sizes for pump and signal are: $w_{op} = 0.029$ mm, $w_{os} = 0.035$ mm. For the CPM KTP OPO, the maximum value of h_{sm}^{+} is 0.0326, which is nearly a factor of 10 less than that of the NCPM case and, as shown in Fig. 5.3, it appears at $\xi_p \approx 1.0$, $\xi_s \approx 1.33$; the corresponding beam spot sizes are: $w_{op} = 0.049$ mm, $w_{os} = 0.054$ mm. Therefore, although the CPM KTP OPO allows the use of long crystal, the much lower h_{sm}^{+} means poor mode matching exists and therefore less power transfer from pump to signal. The difference between h_{sm}^{+} (NCPM) and h_{sm}^{+} (CPM) is reduced in the case of less tight focusing. For example, when $\xi_p = \xi_s = 0.1$, the value of h_{sm}^{+} is 0.048 in the NCPM KTP OPO, and it is 0.0146 in the CPM KTP OPO.

Similarly, the variation in h_{sm}^{-} as a function of focusing parameters in a backward-going pump for both the NCPM and CPM KTP OPOs, are shown in Figs. 5.5 and 5.6. The curves in the two figures show similar high values, indicating that h_{sm}^{-} is largely dependent on the divergent backward-going pump, and not the walk-off in the CPM KTP OPO. The maximum h_{sm}^{-} is around 0.2 (appears at $\xi_s \approx \xi_p \approx 1$), this value being less than that of the forward-going pump for the NCPM KTP OPO, but much larger than that of the forward-going pump for the CPM KTP OPO. According to Eq.(2.117) given in Chapter 2, (the expression for pump threshold of a double-pass-pumped OPO), the much larger value of h_{sm}^{-} in comparison with h_{sm}^{+} for the CPM KTP OPO, promises a more than factor of 2 reduction in pump threshold when double-pass-pump configuration is employed.

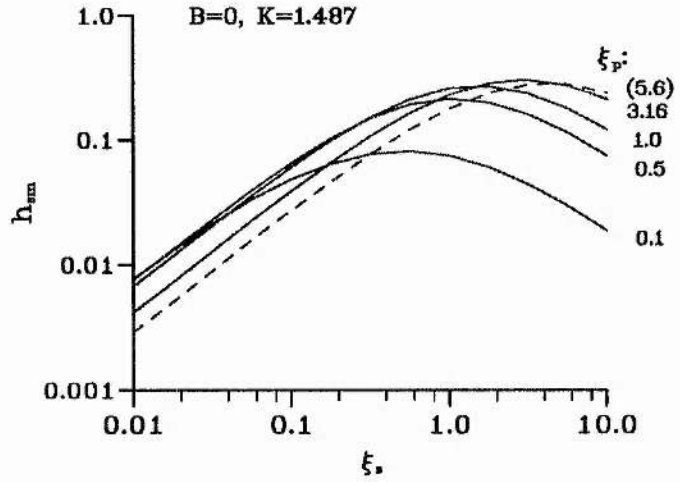

Figure 5.3: Variation of h^+_{sm} as a function of ξ_s and with the parameter of ξ_p for the NCPM KTP OPO and in a forward-going pump, where l_c=25 mm.

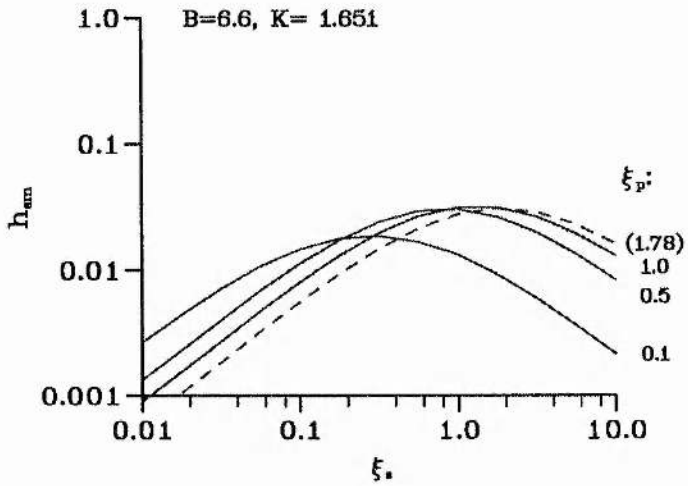

Figure 5.4: Variation of h^+_{sm} as a function of ξ_s and with the parameter of ξ_p for the CPM KTP OPO and a forward-going pump, where l_c=25 mm.

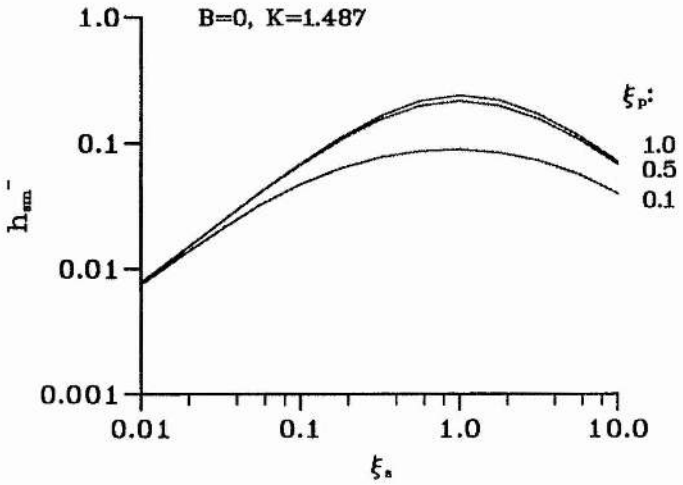

Figure 5.5: h_{sm}^- value of backward-going of NCPM KTP OPO

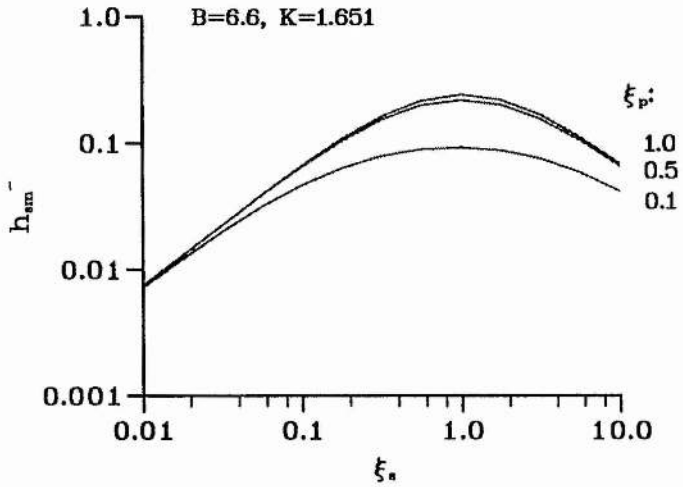

Figure 5.6: h_{sm}^- value of backward-going of CPM KTP OPO

5.2 Single-pass-pumped OPO

Single-pass-pumping is the simplest and most basic configuration of the four pump geometries considered (as mentioned previously in this chapter). Since the gain is only being produced in the forward-going direction in this pump configuration, the results obtained here are readily extended to the other three configurations.

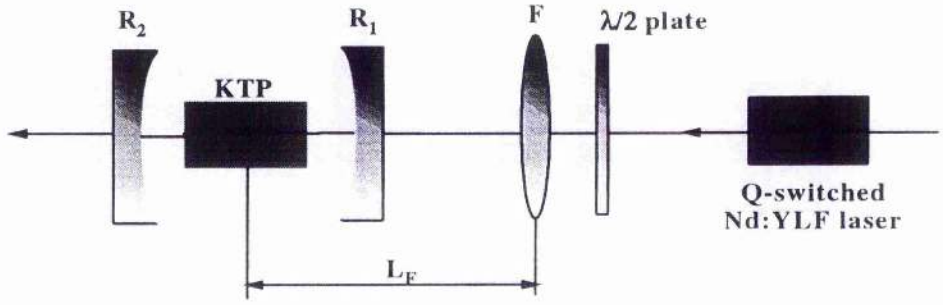

Figure 5.7: Experimental set-up of single-pass-pump OPO.

The experimental set-up used in this work is shown schematically in Fig. 5.7. The resonator was symmetrically structured with two concave mirrors having curvatures of either 500 mm or 100 mm. For convenience, we call the OPO cavity formed by the two 500 mm curvature mirrors as the 500 mm OPO cavity, and similarly also the 100 mm OPO cavity.

All mirrors were coated for high transmission at 1 μm, and the output mirrors were coated for 10% transmission at 1.54 μm; the rear mirrors were coated for high reflection ($R > 98\%$) at 1.54 μm. These mirrors were also used for the CPM OPOs to resonate the signal wave centred at 1.7 μm. Through a spectral scan system built by ourselves, the transmission of the output mirror at 1.7 μm was found to be 15%, and the reflection of the rear mirror at 1.7 μm was found to be 95%.

To achieve good mode overlap between pump and signal waves, two different combination between OPO cavity and focus lens were used for each pump laser, which were:

1. EO Q-switched laser + 400 mm focus lens + 500 mm OPO cavity.
2. AO Q-switched laser + 100 mm focus lens + 100 mm OPO cavity.

The size of the pump beam waist at the focal point was estimated by using heat-sensitive paper and then a CCD camera was used for further measurement. As a lot of filters were

Table 5.2: Summary of focusing parameters and h^+_{sm} for the single-pass-pumped KTP OPOs.

Phase-matching	NCPM	NCPM	CPM	CPM
OPO cavity	500 mm	100 mm	500 mm	100 mm
w_{op} (mm)	0.21	0.135	0.21	0.135
ξ_p	0.054	0.13	0.054	0.13
b_p (mm)	463	191	463	191
w_{os} (mm)	0.189	0.13	0.189	0.13
ξ_s	0.095	0.2	0.105	0.22
b_s (mm)	262	124	237	112
h^+_{sm}	0.0375	0.0773	0.0133	0.02

used in the measurement with the CCD camera, pump beam spot size estimated by this method may be smaller than real size. However, the results detected by heat-sensitive paper (intensity dependent) may give a bigger size than the real. In our analysis, the pump beam spot size was evaluated using both measurements. The pump beam waist of the EO Q-switched laser after a 400 mm focus lens then was evaluated to be 0.21 mm; and it was evaluated to be 0.135 mm for the AO Q-switched laser after a 100 mm focus lens. The focusing parameters relevant to the two experimental arrangements are listed in Table 5.2.

It is notable that the h^+_{sm} values of the 500 mm OPO cavity with the use of the EO Q-switched laser pump is nearly a factor of 2 less than that of the 100 mm OPO cavity with the use of the AO Q-switched laser. However, it is impossible to increase h^+_{sm} by further focusing down pump and signal beams, as seen in Table 5.2, since the signal beam waist was 0.189 mm in this case, which was already close to the focusing limitation of $w_o \geq 0.18$ mm.

The OPOs were easy to align by using the following procedures. We first place the KTP crystal at the position of the pump waist. With a specially designed crystal holder, the KTP crystal was moveable and rotatable along the vertical and horizontal directions. The two mirrors were then spaced as close as possible to reduce the round trip time, normally the space was 32 mm. All surfaces of the optical components were aligned to be perpendicular to the pump beam by placing a pinhole on the optical path. The polarization of pump wave was adjusted accurately by rotating a half wave plate.

In the experiment, the pump pulse was detected by a fast response silicon photo-diode,

and the signal pulse was detected by a germanium photo-diode.

5.2.1 Oscillation threshold

In modelling the OPO operation for the case of pulsed laser pumping, we have assumed a Gaussian time profile for the pump pulse in order to calculate thresholds. This is appropriate for the EO Q-switched laser. However, it is not so appropriate in the case of the AO Q-switched laser, since a typical pulse now has a fast rise time, and a long tail.

For a given crystal and OPO geometry, beam focusing and walk-off are important factors in determining pump threshold, and are treated through the h_{sm} parameter. We must point out that although the oscillation threshold is inversely proportional to the signal beam output coupling [see the relation described by Eq.(2.99) in Chapter 2], it is not always appropriate to reduce threshold by using lower output coupling. Lower output coupling can lead to lower conversion efficiency as has been observed in both our experiment and theoretical analysis. A further discussion will be given in the next section.

In this work, the pump threshold calculation for the case of single-pass-pump was based on equation (2.108) given in Chapter 2. To compare the theoretical modelling with experiments, the pump threshold was defined as that pump energy for which the signal energy reaches the minimum detectable level by the equipment after n round trips. For instance, assuming the minimum detectable power of the power meter is 0.1 mW, if the pulse repetition is 14 Hz, then the signal energy at the threshold point is 7 μJ; and if the repetition is 125 Hz, then the signal energy at threshold point is 0.8 μJ. Experimentally, the pump threshold was determined at a point where the signal spot just can be seen from a infrared display card.

Fig. 5.8 shows the pump threshold behaviour for the NCPM KTP OPOs. With two 10% output couplers forming the OPO cavity ($T_s \approx 20\%$), the typically pump energy threshold was 0.8-0.9 mJ for the case of using the 500 mm OPO cavity, when the corresponding pump peak power was 60 kW (pump pulse width=14 ns). It was to be 0.136 mJ for the case of the 100 mm OPO cavity, when the corresponding peak power was 5 kW (pump pulse width=20 ns). Clearly, the measured pump thresholds for the two cases are reasonably close to the theoretical predictions. According to the h_{sm} curves given in Fig. 5.3 for this OPO geometry, the pump threshold can be further reduced by focusing both pump and signal beams until $\xi_p = \xi_s = 2.8$.

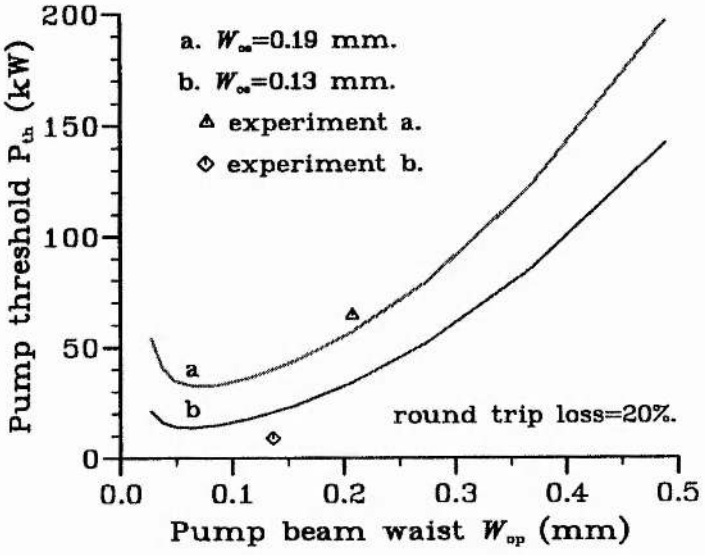

Figure 5.8: Pump threshold of single-pass-pumped NCPM KTP OPO.

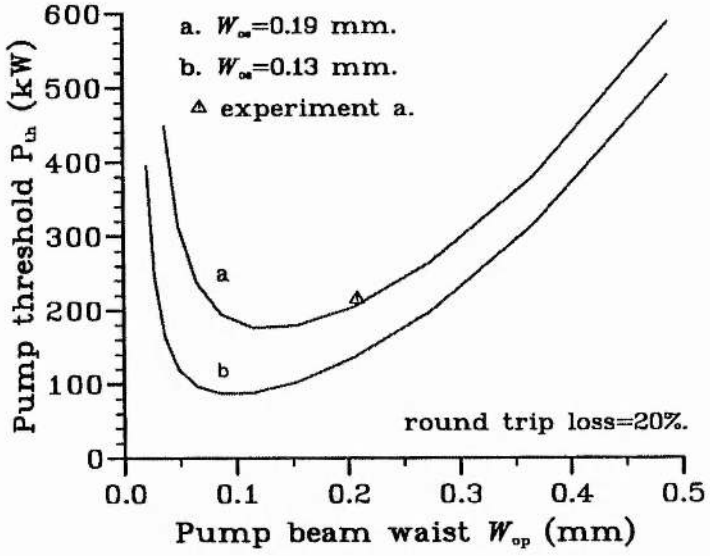

Figure 5.9: Pump threshold of single-pass-pumped CPM KTP OPO.

Table 5.3: Pump threshold of KTP OPOs in the single-pass-pump configuration.

Phase-matching	NCPM	NCPM	CPM	CPM
OPO cavity	500 mm	100 mm	500 mm	100 mm
w_{op} (mm)	0.21	0.13	0.21	0.13
Pump threshold energy (mJ)	0.8-0.9	0.136	2.5	*
Pump pulse width (ns)	14	20	12	*
Peak power of pump (kW)	60	6	210	*
Pump intensity (MW/mm^2)	0.45	0.1	1.5	*

Fig. 5.9 shows the pump threshold behaviour for the CPM KTP OPOs, where the OPO cavity was formed by one output coupler and one signal wave high reflector. The round trip loss of this cavity was estimated to be 20%. The measured pump energy threshold for the case of the 500 mm OPO cavity and with pumping by the EO Q-switched laser was 2.5 mJ. The device did not work when pumped by the AO Q-switched laser (the available maximum pump peak power from this laser was 20 kW at this time.). Obviously, the higher pump threshold of the CPM KTP OPO was due to the double refraction of the idler wave. The observed experimental phenomenon, *i.e.* a three times higher pump threshold for the CPM OPO than for the NCPM OPO when pumped by the EO Q-switched laser is, in fact, very much in agreement with the prediction given by the values of the h_{sm}^{+} parameter for the two OPO geometries as seen in Table 5.2. The reason that the CPM KTP OPO with the AO Q-switched laser pumping did not work can be also explained by the h_{sm} parameter. For the case of the 100 mm OPO cavity, the h_{sm} values listed in Table 5.2, for the NCPM OPO is h_{sm}(NCPM)=0.0773, but for the CPM OPO, it is h_{sm}(CPM)=0.02. The difference in the h_{sm} values for the two OPO geometries indicates at least a 3.4 times higher pump threshold, *e.g.*, 20 kW peak power was required for this CPM KTP OPO with the 100 mm OPO cavity.

In summary, the experimental results for the pump threshold of the KTP OPOs in the single-pass-pumped configuration are listed in Table 5.3.

5.2.2 Conversion efficiency

In this study, the conversion efficiency is defined as the external energy conversion efficiency from input pump energy to the output signal energy. Because the parametric interaction is an elementary three-photon process, there is no energy storage in the OPO cavity and

the pulse width of the signal is primarily determined by that of the pump, and normally it is slight narrower than the pump pulse due to the signal field build up time. The build up time in this configuration was found to be ~2 ns for the NCPM geometry and ~3 ns for the CPM geometry. Thus the peak power conversion efficiency, in fact, is higher than the energy conversion efficiency.

The signal output power was measured either after a 1 μm cut-off filter, or a prism. Because of the high absorptions of the idler wave in either the crystal or the substrates of the mirrors, the idler output was not detected for such an OPO geometry. To detect the idler wave, a folded cavity was used which will be described in a later section.

The theoretical calculation for conversion efficiency was based on the model given in Chapter 2. Because a plane wave theory was used here, the theoretical results were restricted to a uniform intensity distribution and therefore were useful for predicting some OPO parameters, such as crystal length, mirror reflectivity, and pump intensity; but were not suitable for analysing problems such as mode matching.

(1) NCPM KTP OPO

The experimentally achieved conversion efficiencies for the NCPM KTP OPOs with the use of the single-pass-pump configuration are summarised in Figures 5.10 and 5.11. A comparison of conversion efficiency with the 100 mm OPO cavity and the 500 mm OPO cavities is shown in Figure 5.10, where the output coupling used for both OPOs was 20%. To show the intensity dependency, as seen in this figure, the calculated conversion efficiency curves are plotted in respect of both pump energy (solid curve) and pump intensity (dashed curve).

Clearly, both the experimental data and the calculated curves[1] show that the conversion efficiency for the case of using the 100 mm OPO cavity is much higher than that of using the 500 mm OPO cavity. However, the two dashed curves indicate that the two OPOs, in fact, were operating in the same pump intensity region. For the same pump intensity, the higher conversion efficiency achieved in the case of using the 100 mm OPO cavity has again proved the benefit of using higher value of h_{sm}.

The fast pulse rise time of the AO Q-switched laser might be an additional contribution to the conversion efficiency. As has been pointed out by Marshall and Kaz[2], a sufficiently

[1]This calculation was based on plane wave theory and therefore the predicted conversion efficiency was intensity dependent. The achieved relative high peak for the case of 100 mm OPO cavity as shown in this figure was due to the assumed relative large signal waist in the calculation [see Eqs. (2.123) and (2.124)].

fast rise time to permit the OPO to exceed threshold before a significant amount of pump energy has passed through the crystal is very important for high conversion efficiency. They have demonstrated an increased conversion efficiency from 40% to 47% by tailoring the pump pulse.

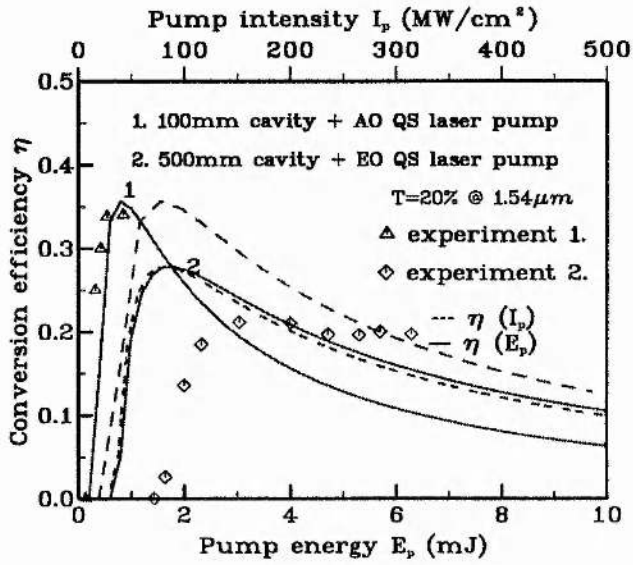

Figure 5.10: Conversion efficiency of single-pass-pumped NCPM KTP OPO, where the pump intensity dependence and the pump energy dependence of conversion efficiency are indiceted by the dashed and the solid curves respectively.

No optical damage was observed in the case of using the 100 mm OPO cavity although very tight focusing was used. This is not a surprise because maximum intensities of either the signal or pump beams were far from the damage threshold as shown in Fig. 5.10. However, the maximum pump energy in the case of using the 500 mm OPO cavity was limited by optical damage at the level of $\geq$ 5 mJ (When pump energy reached 5 mJ, the noise of surface damage was heard frequently.).

Fig. 5.11 illustrates the variation of the conversion efficiency when a 10% output coupler and a 20% output coupler were used for the NCPM OPO for the case of the 500 mm OPO cavity. Clearly as shown in this figure, the mirror's transmission is an important factor for OPO operation, and should be chosen to match a particular pump intensity. For instance, for the pump intensity region 50-100 MW/cm^2, T= 20% is the optimum value for maximum conversion efficiency, but when the pump intensity increases to 120-200 MW/cm^2, a more appropriate value is T=40%. Generally, a high conversion efficiency

OPO requires that one overcomes the problem of back conversion. Whether conversion is forward or backward depends largely on the ratio of the signal to the pump of the photon fluxes, but not so much on either signal or pump flux alone. This can be explained by using the exact plane wave solution for a SRO[3]. If one uses 'ρ' to express the ratio of photon fluxes, *i.e.*

$$\rho = \frac{u_s^2(0)}{u_p^2(0)},$$

and uses 'G' to express the signal net gain on a round trip, *i.e.*

$$G = R\frac{u_s^2(\xi)}{u_p^2(0)},$$

where R is the signal power loss coefficient on a round trip, then according to equations (2.118) and (2.119), the expression for G in terms of the ratio ρ is given as:

$$G(\rho) = R\frac{u_s^2(\xi)}{u_p^2(0)} = R(\rho + 1 - sn^2[u_p(0)(\xi + \xi_0)/\gamma, \gamma^2])$$

where ξ, ξ_0, and γ all depend on ρ as described in Chapter 2. Hence ρ is a control parameter. Obviously, for a high gain device, such as the KTP OPO, choosing the mirror reflectivity so as to keep the appropriate ratio of photon fluxes is very important to optimize OPO operation.

(2) CPM KTP OPO

The measured conversion efficiency for the CPM KTP OPO for the case of the 500 mm OPO cavity are compared with the calculated curve in Fig. 5.12. The measured maximum external conversion efficiency from pump to signal was 19%, which is close to the calculated value of 25%. The low conversion efficiency of this CPM KTP OPO was due to the double refraction of the idler wave. According to the curves given in Fig. 5.4, the h_{sm} value of this CPM KTP OPO can be increased by further focusing the signal and pump beams, leading to improved operation of this OPO. However, further focusing was limited by the damage threshold.

5.2.3 Wavelength tuning

In the wavelength measurements, the accuracy of the monochrometer was calibrated to be $\leq$0.3 nm at the pump wavelength 1.047 μm.

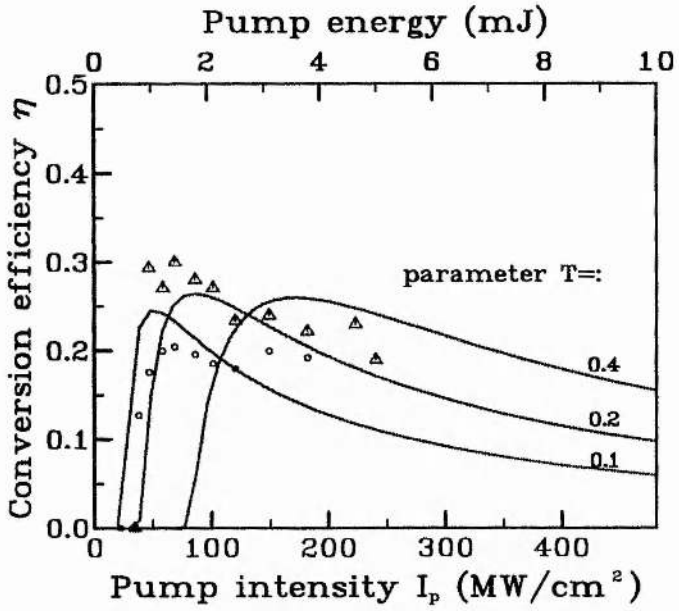

Figure 5.11: Conversion efficiency of single-pass-pumped NCPM KTP OPO with parameter of mirror transmission T, where W_{os}=0.19 mm, W_{op}=0.22 mm, pump pulse width Δt=14 ns; and where the triangles indicate the experimental data when T=20%, and the circles indicate the experimental data when T=10%.

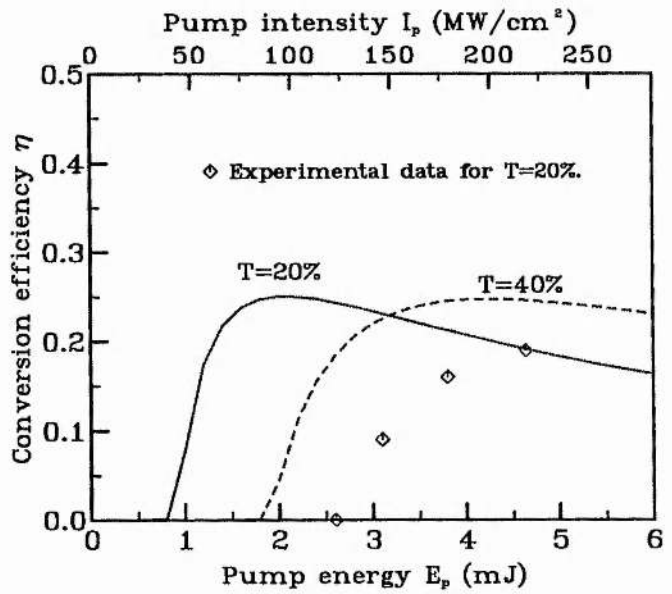

Figure 5.12: Conversion efficiency of single-pass-pumped CPM KTP OPO for the 500 mm cavity, where pump beam waist W_{op}=0.22 mm, signal beam waist W_{os}=0.19 mm, pump pulse width Δt=14 ns.

The measured signal wavelength from the NCPM KTP OPO was **1.538** μm, the corresponding idler wavelength was **3.28** μm.

The measured signal wavelength from the CPM KTP OPO was tunable from **1.654** μm to **1.736** μm, the corresponding idler wavelength tuning range was from **2.853** μm **to 2.638** μm.

As shown in Fig. 5.13, the experimental results are in good agreement with the calculated tuning curve, where the calculation was based on Vanherzeele's Sellmeier equation[4].

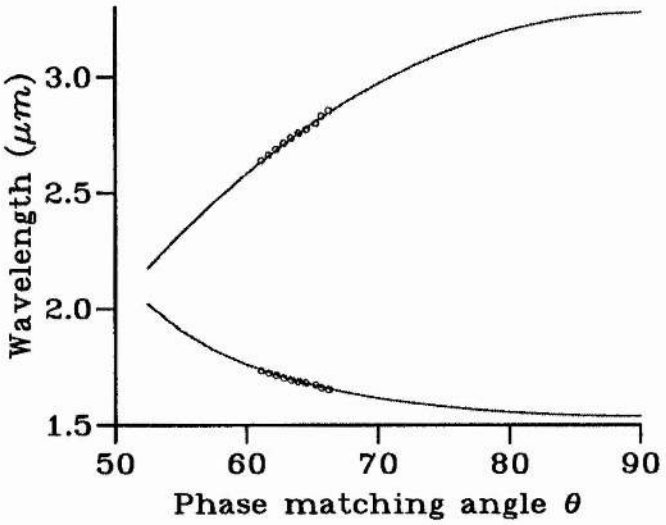

Figure 5.13: Wavelength tuning of single-pass-pumped CPM KTP OPO.

5.2.4 Transverse mode

Occasionally, the signal wave appeared as a circular mode (close to TEM_{oo}), particularly after a new coating was applied to the surfaces of the KTP. However, in most cases a ring structure was observed on the signal wave. We even inserted a tiny pinhole to limit the resonant mode, but the ring structure was still there. The same phenomena were observed by Jonathan Terry [5]. Up to now, we cannot give a clearly explanation since our analysis is limited to the plane wave approximation. We believe, this phenomena can be numerically simulated in further analysis using the Gaussian beam approach. Unlike the NCPM OPO case, the transversal mode of the signal in the CPM OPO appeared to be less clearly a ring structure, but it was not a circular mode either.

5.3 Double-pass-pumped OPO

Because of the high pump threshold of the single-pass-pumped CPM OPO, it was decided to study the double-pass-pumped OPO scheme. A schematic of the double-pass-pumped OPO is shown in Fig. 5.14.

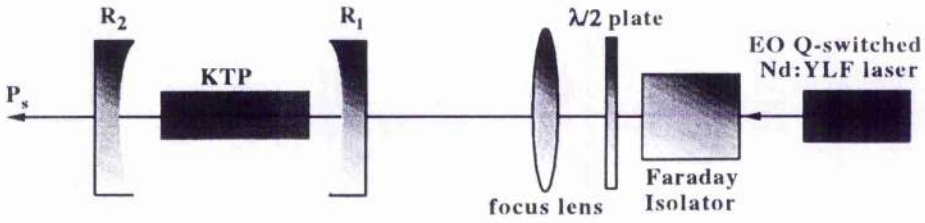

Figure 5.14: Experimental set-up of the double-pass-pumped OPO.

Basically, the arrangement was similar to the single-pass-pumped configuration. The OPO was formed symmetrically with a pair of concave mirrors, the non-resonant pump beam was highly reflected from the signal wave output mirror R_2 and passed back through the crystal to produce additional gain. To prevent the pump beam going back to the laser cavity, a Faraday isolator was installed in the system.

Since the AO Q-switched laser was not available at this time, all the experiments on the double-pass-pumped KTP OPOs were completed with the EO Q-switched laser. The output mirrors used were coated for high reflectivity at 1 μm, and have partial reflectivities of 10%, 20%, and 30% at the NCPM KTP OPO signal wavelength, 1.54 μm. These mirrors were also used for the CPM KTP OPOs. Their signal wave reflectivity at 1.7 μm, the central signal wavelength of the CPM KTP OPO, was found to be 38%.

In Table 5.4, we summarise the h_{sm} values for both the forward going and backward going trips for the case of the 500 mm OPO cavity. Clearly, since the value of the h_{sm}^{-} for the case of the 500 mm OPO cavity is nearly equal to that of the h_{sm}^{+} in the NCPM KTP OPO, and is about 2.5 times higher than that of the h_{sm}^{+} in the CPM KTP OPO, the performances of the KTP OPOs were expected to be improved dramatically by using the double-pass-pump configuration.

5.3.1 Oscillation threshold

The main purpose of this study was to examine how the pump threshold could be reduced using the increased value of h_{sm}^{-} during the backward-going pump.

Table 5.4: Summary of h_{sm} values for the double-pass-pumped KTP OPO with the 500 mm cavity.

Phase-matching	NCPM	CPM
w_{op} (mm)	0.21	0.21
w_{os} (mm)	0.19	0.19
ξ_p	0.054	0.054
ξ_s	0.095	0.105
h_{sm}^{+}	0.0375	0.0133
h_{sm}^{-}	0.0360	0.0343

(1) NCPM geometry As expected from the above analysis the pump threshold energy of the NCPM KTP OPO in the case of using the double-pass-pump configuration was observed to be 0.46 mJ. The pump pulse width in this case was 15 ns, so the corresponding peak power was 33 kW. Therefore, this result showed a factor of 2 lower pump threshold than that achieved in the case of using the single-pass-pump. Moreover, the output mirror's transmission used in this case was 30%, but it was 20% used in the case of the single-pass-pump.

The calculated pump threshold curves as a function of pump beam waist for the 500 mm OPO cavity and the 100 mm OPO cavity are shown comparatively in Fig. 5.15. To illustrate the improvement with the use of the double-pass-pump configuration, the calculated pump threshold curve for the case of the 500 mm OPO cavity using the single-pass-pump is also plotted in this figure as shown by the dashed curve.

(2) CPM geometry The measured oscillation threshold energy for the case of the CPM KTP OPO with the use of the 500 mm cavity in a double-pass-pump configuration was 0.64 mJ. Comparing this with the case of the single-pass-pump (Pump threshold was 2.5 mJ in this case for T_s=20%.), it can be seen that the pump threshold was reduced by a factor of 3.8 using the double-pass-pump configuration (for which T_s=38%.).

Fig. 5.16 shows the experimental results and predictions of this study. Although the low peak power AO Q-switched laser was not used in this experiment, the theoretical curve *b* indicates that the peak power pump threshold is possibly as low as 20 kW for the case of T_s=38%; and that it can be further reduced to ~10 kW by reducing the mirror's transmission to be T_s=20%.

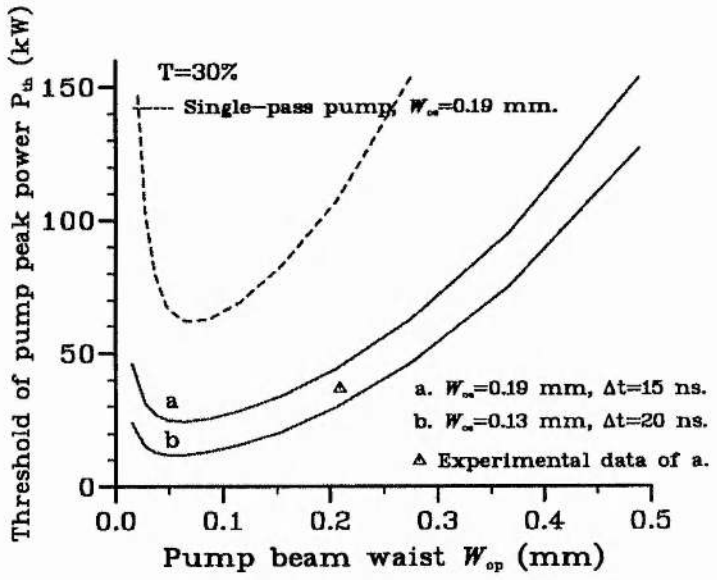

Figure 5.15: Pump threshold of double-pass-pumped NCPM KTP OPO.

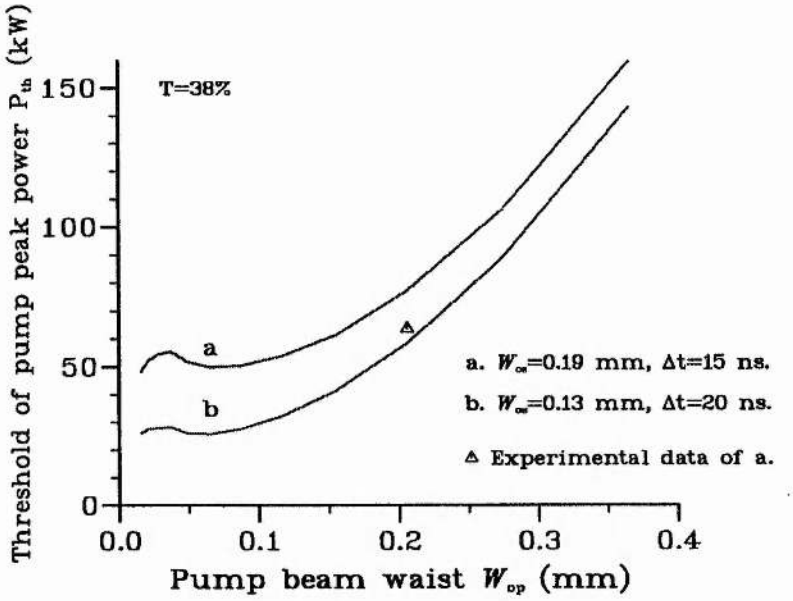

Figure 5.16: Pump threshold of double-pass-pumped CPM KTP OPO.

Table 5.5: Summary of pump threshold of KTP OPO for both double-pass and single-pass-pump configurations.

pump configuration	double-pass	double-pass	single-pass	single-pass
phase-matching	NCPM	CPM	NCPM	CPM
h_{sm}^{+}	0.0375	0.0133	0.0375	0.0133
h_{sm}^{-}	0.0360	0.0343	0	0
pump threshold energy (mJ)	0.45	0.65	0.9	2.5
peak power (kW)	33	54	60	210
pump intensity (MW/cm^2)	0.2	0.39	0.43	1.5

In summary, the experimentally measured pump thresholds for both the double-pass-pump and the single-pass-pump KTP OPOs are listed in Table 5.5. The successful operation of the double-pass-pumped OPO not only demonstrated a low pump threshold, but also the good agreement between predictions based on calculations of the h_{sm} function and experiment results has confirmed a useful technique for OPOs in general.

5.3.2 Conversion efficiency

The additional pumping during the backward going pump not only reduced the threshold but also increased the conversion efficiency, as observed in our experiment.

(1) NCPM geometry

For the case of using the 500 mm OPO cavity with the output coupling T_s=30%, the experimentally observed maximum external conversion efficiency was 37%. This is 1.4 times higher than that of the single-pass-pumped OPO. Fig. 5.17 shows the conversion efficiency behaviour of this OPO. Good agreement between the experimental and theoretically predicted curves for this OPO can be seen in this figure. The increase in conversion efficiency for this double-pass-pumped OPO can be seen by comparison with the dashed curve which was calculated for the case of the single-pass-pump.

Fig. 5.18 illustrates the variation of the conversion efficiency when different output couplers were used with the NCPM KTP OPO based on the 500mm OPO cavity. We see that 40% may be the optimum signal transmission in the pump energy range 1-5 mJ.

For the case of the 100 mm OPO cavity and pumped by the AO Q-switched laser, Fig.

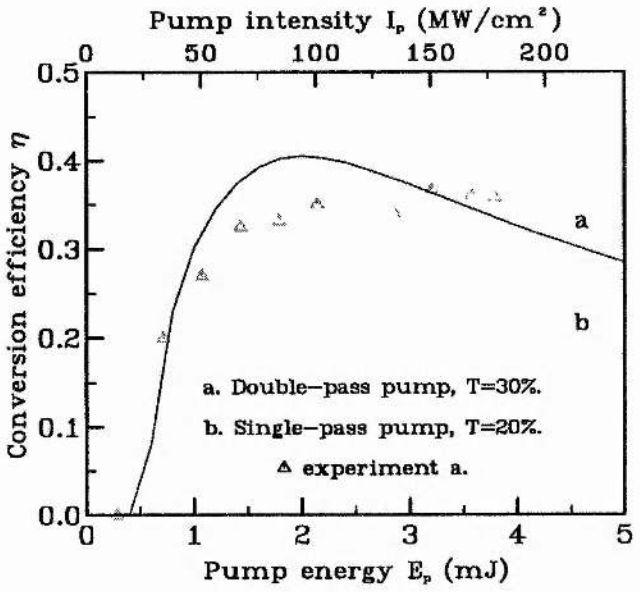

Figure 5.17: Conversion efficiency of double-pass-pumped NCPM KTP OPO for the 500 mm OPO cavity.

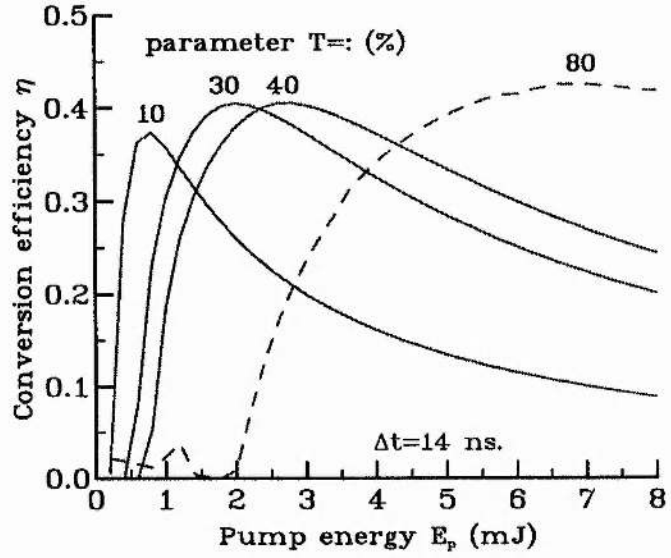

Figure 5.18: Conversion efficiency of double-pass-pumped NCPM KTP OPO with the parameter of T_s.

5.19 shows the predicted conversion efficiency behaviour. It is possible for this OPO to offer higher conversion efficiency than that in the case of using the 500 mm OPO cavity as the predicted curves of T_s=20% and T_s=30% show. To illustrate the relatively high efficiency in the double-pass-pumped OPO, we have also plotted the predicted conversion efficiency curve for the case of the single-pass-pumped OPO based on the 100 mm cavity, as shown by the dashed curve.

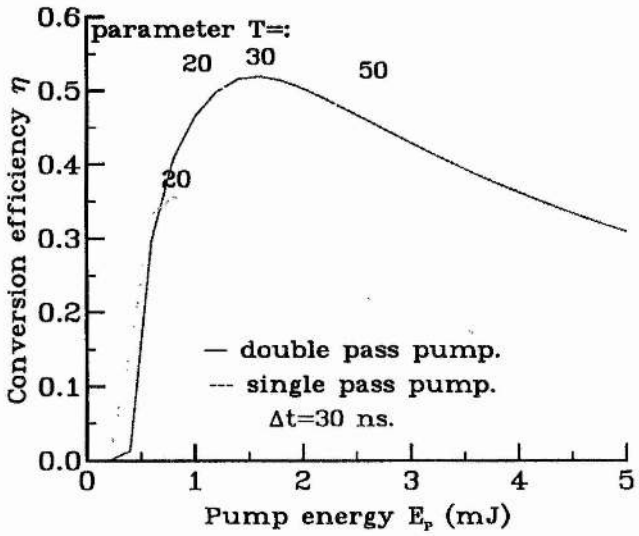

Figure 5.19: Conversion efficiency of double-pass-pumped NCPM KTP OPO for the 100 mm cavity.

(2) CPM geometry

As was mentioned before, the only available mirror transmission was 38% for the double-pass-pumped CPM KTP OPO. The measured maximum conversion efficiency for the case of the 500 mm OPO cavity was about 40%[2] measured with the pump beam normally incident on the crystal. The experimentally achieved conversion efficiency for this OPO is comparatively shown in Fig. 5.20.

[2]In fact, the observed maximum conversion efficiency was 42%. However, using a IR spectral-meter, the idler wave transmission (around ~2.7 μm) of both the output and the rear mirrors were found to be ~30%, and there may be less absorption of the idler wave in crystal as well. Therefore, possibly a very little of the idler wave output was included in the signal output power detection, and we only can say that the conversion efficiency was ~40%.

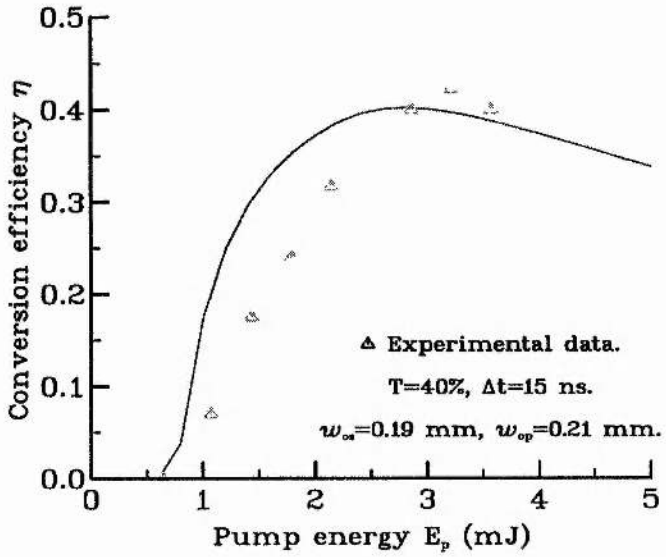

Figure 5.20: Conversion efficiency of double-pass-pumped CPM KTP OPO for the 500 mm cavity, where the pump beam waist is W_{op}=0.21 mm, the signal beam waist is W_{os}=0.19 mm, and the pump pulse width is Δt=15 ns.

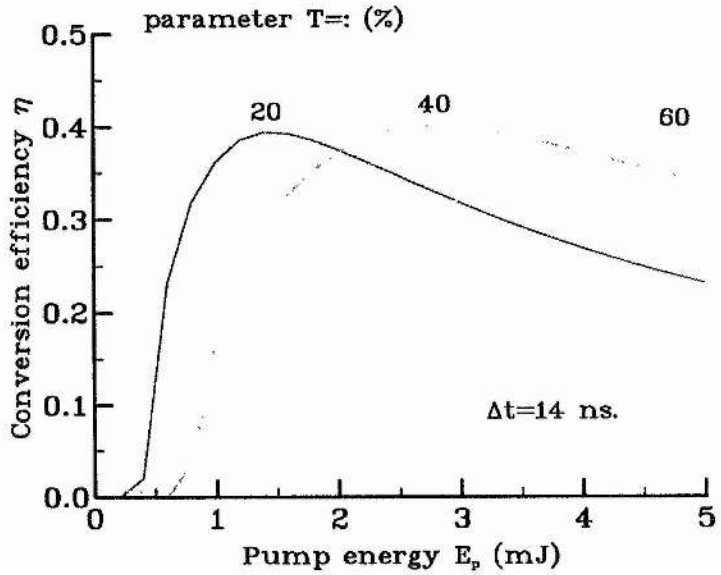

Figure 5.21: Conversion efficiency of double-pass-pumped CPM KTP OPO with the parameter of T_s.

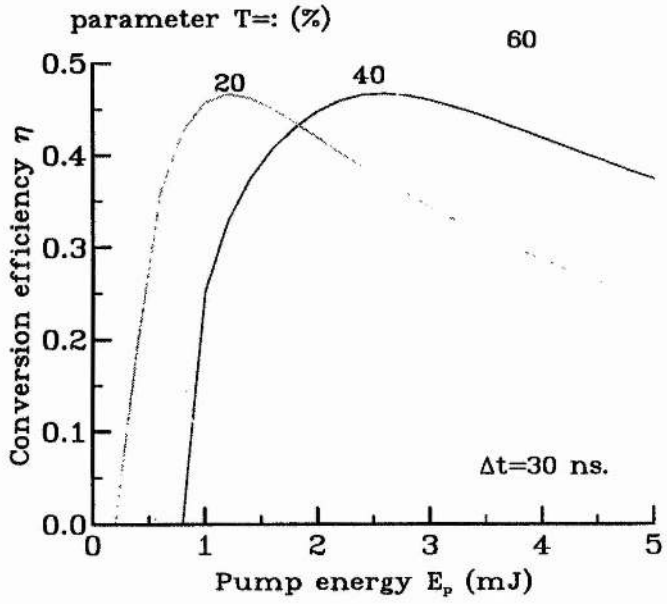

Figure 5.22: Conversion efficiency of double-pass-pumped CPM KTP OPO for the 100 mm cavity.

Fig. 5.21 illustrates the variation of the conversion efficiency when different output couplers were used for the CPM KTP OPO based on the 500mm OPO cavity. It can be seen that 40% is the optimum transmission for the pump energy in the range of 1-5 mJ. Lower transmission, such as T=20% may be needed when the pump energy is in the range of 0.5-1.5 mJ.

To show the conversion efficiency behaviour for the case of the 100 mm OPO cavity, the calculated curves with different transmissions are shown in Fig. 5.22. We see that the maximum efficiency in this case can reach 45%, and T=20% is the optimum transmission for the pump energy range 0.5-1.5 mJ.

5.3.3 Wavelength tuning

Because of the low threshold and high efficiency of the double-pass-pumped scheme, much wider tuning ranges were obtained than in the case of single-pass-pump. There were **1.587 -1.84** μm from the CPM KTP OPO, and **1.537-1.5535** μm from the NCPM KTP OPO. The corresponding idler tuning ranges were **3.08-2.42** μm and **3.284-3.211** μm. Fig. 5.23 shows the wavelength tuning curves of the KTP OPOs, where the dotted

points are experimental results (△ for the CPM KTP, and ◇ for the NCPM KTP), and the continuous curves are theoretical calculations based on the Vanherzeele's Sellmeier Equations.

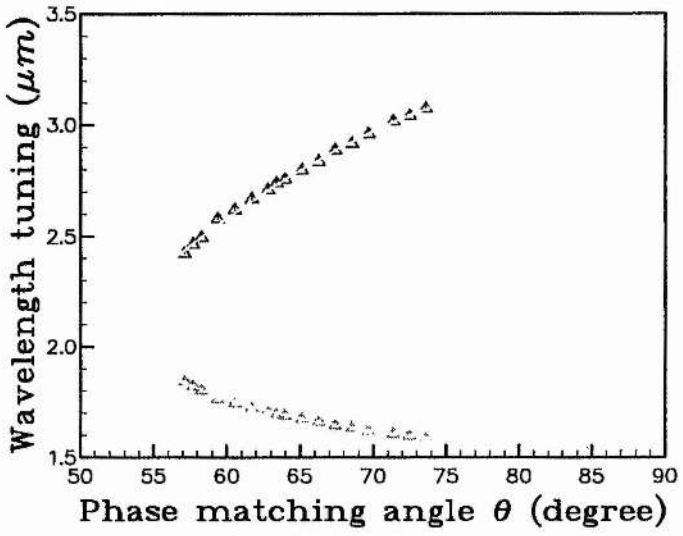

Figure 5.23: Wavelength tuning of double-pass-pumped KTP OPO.

5.3.4 Transverse mode

The doughnut transverse mode was a problem in the single-pass-pump configuration. However, a very good circular mode was observed all the time in the double-pass-pumped KTP OPO.

5.3.5 OPO line width measurement

The experimental set-up for the linewidth measurement is shown schematically in Fig. 5.24. The output spectrum at the signal wavelengths was observed by using a Fabry-Perot interferometer in conjunction with an IR vidicon (Hamamatsu Beam Finder II, C3283). The gap between the two mirrors of the interferometer was adjusted to be 0.3 mm for a Free Spectral Range of 500 GHz. The spectral content of the signal output was examined by the Fabry-Perot interferometer, and then imaged onto the IR vidicon. The signal from the vidicon went to a monitor via a frame grabber. The use of the frame grabber allowed the pulse to pulse spectral variations to be observed.

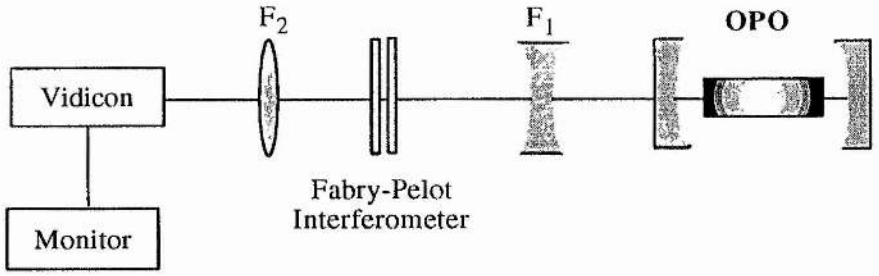

Figure 5.24: Experimental set-up for OPO linewidth measurement.

Single cluster oscillation was apparent in the NCPM OPO, and the measured spectral linewidth of the signal wave was 0.88 nm (FWHM). Two types of behaviours were observed on the signal wave spectrum of the CPM OPO with normal incidence pump. One consisted of a single 'cluster' when the measured linewidth of the signal wave was 1.16 nm (FWHM). The other consisted of 'three clusters' equally spaced. In such a case, the separation between each 'cluster' was 0.547 nm which was found to be caused by the gap between the rear mirror and the KTP surface (2.5 mm wide) acting as an etalon. The linewidth of the signal wave in this case was measured to be 1.517 nm. As shown in Fig. 5.1 (d), the measured spectral width for the case of the single cluster is very close to our calculated value using Eq.(2-125).

5.4 Cylindrical focusing pump configuration

Since the beam walk-off of the extraordinary ray is normally in one transverse dimension, *i.e.*, the plane containing the optic axis and the direction of the beam propagation, an enhanced interaction can be obtained with tight focusing of beams in the other transverse dimension.

For the CPM KTP OPO, the walk-off angle lies in the Θ-plane. As the crystal is tuned away from the NCPM point, the acceptance angle $\Delta\theta$ will decrease rapidly while the other acceptance angle $\Delta\phi$ remains exceptional large. For instance, from the data listed in Table 5.1, at normal incidence, $\Delta\phi \approx 100$ mr, but $\Delta\theta \approx 1.6$ mr. This suggests that some considerable advantage can be gained in terms of pump threshold by adopting a cylindrical focusing geometry, *i.e.* focusing beams along the Φ-plane direction, while keeping beams well collimated along the Θ-plane direction.

The experimental set-up is shown in Fig. 5.25, where the OPO was pumped by the EO Q-switched laser. The focusing length of the cylindrical lens was chosen to be between 200-

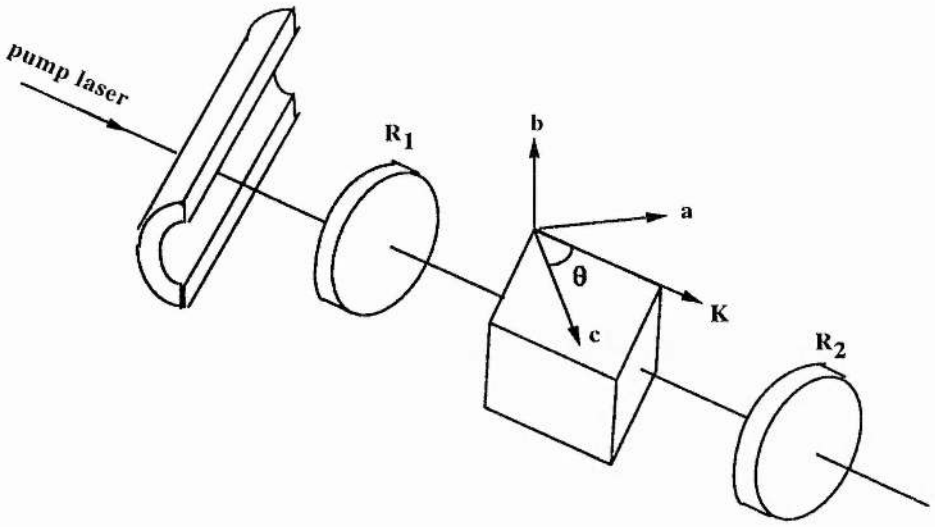

Figure 5.25: Experimental set-up of cylindrical focusing pump configuration.

400 mm, and the OPO was formed by two 500 mm curvature spherical mirrors (cylindrical mirrors were not available). Unfortunately, we did not observe any improvement in pump threshold. This, we believe, was due to the spherical mirrors used on the OPO cavity, leading to poor mode matching between the pump and the signal. If one uses cylindrical mirrors, and careful designs the beam focusing, we believe that the pump threshold can be reduced significantly.

5.5 Intracavity KTP OPO

Another pump configuration used in this KTP OPO study was the intracavity OPO (IOPO), where the crystal was placed inside the laser resonator. Our purpose of using this pump configuration was to effectively operate the KTP OPO when pumped by the low power from the AO Q-switched laser.

The theoretical analysis for IOPOs was first reported by Oshman and Harris [6], who derived the equations of motion for such oscillators by using self-consistency equations. Later, Falk *et al.* [7] extended this theory to include the dynamics of the population inversion of the laser medium. Since then very few further reports have appeared.

The experimental arrangement of the intracavity KTP OPO is shown in Fig. 5.26. The laser cavity was plano-concave, where the plane mirror was used for the output, and the concave mirror was used for the rear end of the cavity. The pump beam waist in such a configuration locates close to the plane mirror. The OPO cavity was plano-plano,

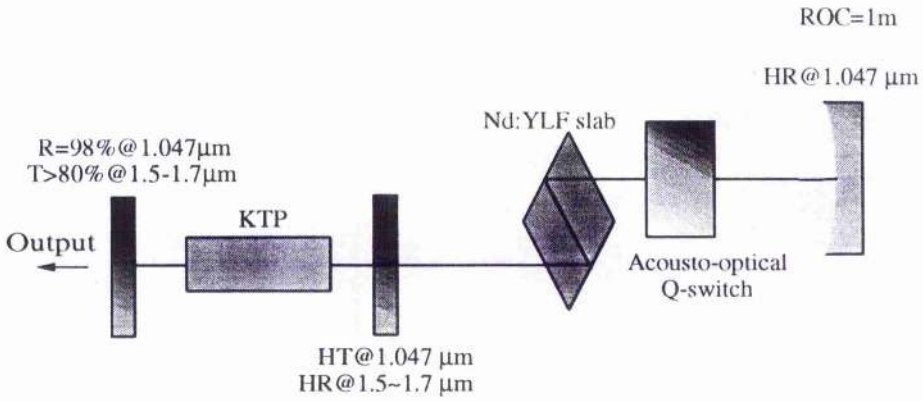

Figure 5.26: Experimental set-up of the intracavity OPO.

formed by the plane mirror of the laser resonator and a further plane mirror which was installed between the KTP crystal and the Nd:YLF slab as a short wavelength-pass and long wavelength reflector. To achieve good mode overlap, the KTP crystal was placed as close as possible to the front mirror. The output mirror of the OPO was original used as a low transmission coupler ($T = 2\%$) of the Nd:YLF laser, and its transmission at the signal wavelength 1.5~1.7 μm was found to be $\geq 80\%$. Because of the BK7 material of the mirror substrate, the output mirror of this OPO could not transmit the idler wave.

From calculation, the radius of the laser beam waist was found to be 0.3 mm, and the radius of the signal wave waist was found to be 0.84 mm. Because of the high reflection of the output mirror at the pump beam wavelength, the intracavity OPO was in some ways similar to the double-pass-pump configuration. In Table 5.6, we summarise the values of the beam waists and the h_{sm} parameter for both the NCPM and CPM KTP OPOs. To detect the signal wave output power, two methods were used. One was by using a dichroic mirror to separate the two wavelengths, this being coated for high reflectivity at 1 μm, and high transmission at 1.5-2.0 μm. The other one was using a short wave filter which provided 99% power transmission at 1.5 μm, and 80% power transmission at 1.7 μm.

(1) NCPM geometry The typical signal wave output from the intracavity NCPM KTP OPO was 240 mW with 25 ns pulse width and 1.9 kHz pulse repetition rate (the corresponding peak power was 5 kW), while the pump wave output was detected to be 77 mW with 53 ns pulse width. The estimated signal wave power inside of the OPO cavity was 240 mW/0.8$\simeq$300 mW. The estimated circulating pump wave power inside the laser cavity was ~4W, the corresponding pump intensity being 7 MW/cm^2, and the corresponding pump peak power being 39.7 kW.

Table 5.6: Parameters of intracavity KTP OPO

Parameter	NCPM	CPM
w_{os} (mm)	0.8	0.8
w_{op} (mm)	0.3	0.3
ξ_p	0.46	0.46
ξ_s	0.006	0.006
h^+_{sm}	0.004	0.0025
h^-_{sm}	0.00386	0.004

(2) CPM geometry The typical signal wave output from the intracavity CPM KTP OPO was 120 mW with 45 ns pulse width and 1.1 kHz pulse repetition rate (the corresponding peak power was 2.4 kW), while the pump wave output was detected to be 100 mW with 65 ns pulse width. The estimated signal wave power inside of the OPO cavity was 150 mW. The estimated circulating pump wave power inside of the laser cavity was ~5W, the corresponding pump intensity being 12 MW/cm^2, and the corresponding pump peak power being 69.9 kW. Like that observed in the double-pass-pumped KTP OPOs, a very good circular mode was observed all the time here in either the NCPM OPO or the CPM OPO. Since a plano-plano OPO cavity and a non-focused pump wave were used in the intracavity OPO, an additional advantage found here was the low beam divergence.

The initial experimental work on the intracavity OPO showed good promise for low pump power operation with high efficiency and good beam quality (*i.e.* TEM$_{oo}$ mode and low divergence). However the high pump wave reflection (R=98%) and high signal wave transmission (T≥80%) of the output mirror resulted in high circulating pump power inside of the laser cavity prior to OPO oscillation, and as a result the diode on one side of the pumped slab was damaged due to pump wave leakage onto the diode (this should not have happened if the coating on the pumping surface of the Nd:YLF had been perfect). The damage can be prevented by coating the pump optics for high reflection at the pump laser wavelength of 1 μm. We believe that with suitable coating of the output mirror, the pump threshold could be reduced dramatically when the intracavity OPO will provide much higher output than that we have achieved so far.

5.6 Idler wave detection

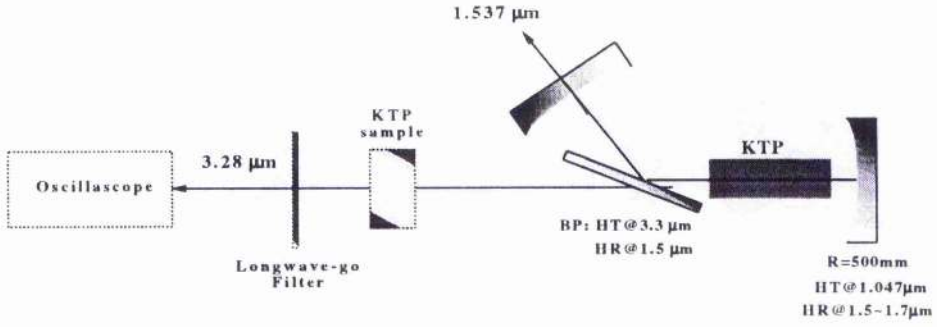

Figure 5.27: Experimental set-up of the idler wave detection.

Although high efficiencies have been demonstrated in both the NCPM or the CPM KTP OPOs, we could not detect the idler wave from the simple two mirror cavity due to absorption in the mirror substrates. As an alternative, we used a C_aF_2 Brewster plate to configure a three mirror cavity as depicted in Fig. 5.27. In this way the idler output could be maximised in the presence of absorption in both the KTP and mirror substrates. The p-polarised idler wave was detected behind a long-wave-pass filter with a lower wavelength cut-off at 2.4 μm and which was measured to have a 20% loss at 3 μm. With a average power of 37 mW pump, the idler was measured to be 0.96 mW, while the output signal wave was 3 mW. By placing another uncoated 5.5 mm long KTP crystal in front of the filter, the absorption coefficient of the KTP at the idler wavelength (3.3 μm) was determined to be α=0.049/ mm, where

$$-\alpha = \left[\ln \frac{E(L_c)}{E(0)}\right] / L_c.$$

On the above the Fresnel loss associated with each surface of the KTP was allowed for by writing the relations

$$E(0) = t \times E'(0)$$

$$E(L_c) = E'(L_c)/t,$$

where the primed quantities E'(L_c) and E'(0) are the detected amplitudes after and before the KTP sample respectively. The value for t was taken to be 0.925.

Bibliography

[1] News, Laser Focus, p18, July 1978.

[2] Larry R. Marshall and A. Kaz, *J. Opt. Soc. AM. B* **10**, 1730 (1993).

[3] David S. Anker, internal reference paper, (1995).

[4] H. Vanherzeele, J. D. Bierlein, and F. C. Zumsteg, *Appl. Opt.* **27**, 3314 (1988).

[5] J. A. C. Terry, *An all-solid-state optical parametric oscillator for the Infrared*, PhD Thesis, (1993).

[6] M. K. Oshman, and S. E. Harris, *IEEE J. Quantum Electron.* **QE-4**, 491 (1968).

[7] J. Falk, and E. O. Ammann, *IEEE J. Quantum Electron.* **QE-7**, 359 (1971).

Chapter 6

Thermo-optical coefficients of LBO

LBO is the only available nonlinear material currently which can be temperature phase-matched over the ultraviolet, visible, and infrared spectral ranges. However, its thermo-optical coefficients (*i.e.* the thermal dependence of principal refractive indices) have only been reported once, by Velsco *et al.* [1], and their measurements were limited to the temperature range 20-60°C. To improve this situation and explore more applications of temperature tuned LBO, we measured these coefficients again, but using a different method and over a more extensive temperature range 20-200°C. In this Chapter, we begin with a description of the measurement technique. We then give an assessment of their usefulness over a wide range of wavelengths. The good agreement between experimental results and predictions using our thermo-optical coefficients shows that we have provided a useful set of thermo-optical coefficients for temperature phase-matching application of LBO. Finally, we discuss the temperature phase-matching properties of LBO and summarise the potential non-critical temperature phase-matching conditions for type I and type II sum-frequency generation.

6.1 Experiment

Two LBO crystals were used in our measurements: one oriented at $\theta = 90^o$, $\phi = 0^o$, which is usually used for type I NCPM, and the other oriented at $\theta = 0^o$, which is usually used for type II NCPM. The experimental set-up is shown schematically in Fiq. 6.1. The LBO

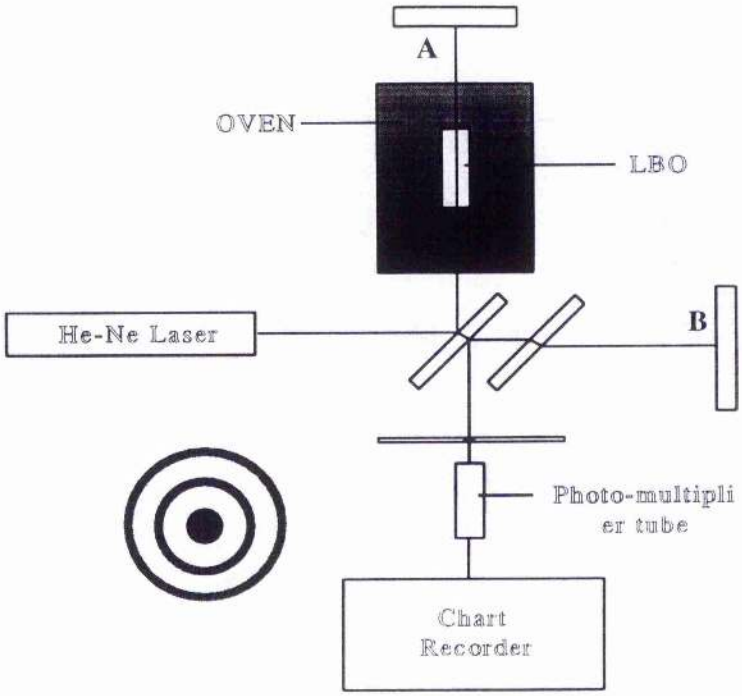

Figure 6.1: Schematic of the experimental set-up for the measurement of thermo-optical coefficients of LBO.

crystal was placed in one arm of a Michelson interferometer. A linearly polarised light beam (0.6328 μm) from a He-Ne laser was split into two beams by a half-silvered mirror **O**. One of the beams propagated through the LBO crystal with its polarisation direction parallel to a principal axis of LBO, and was then reflected normally from mirror Å. The other beam was a reference beam, falling normally on mirror B. The beams were reunited at mirror **O**, where they interfered with each other. The variation of the optical path **OA** with the temperature of LBO was contributed both by the thermal-expansion of the crystal along the beam propagation direction and the thermally induced refractive index change, and it can be measured by counting the interference fringes as described by the equation:

$$\frac{\lambda}{2}\frac{dF}{dT} = L\frac{dn}{dT} + (n-1)\alpha_T L_0 \tag{6.1}$$

where F is the number of interference fringes, L is the crystal length at temperature T,

$$L = L_0 + L_0 \int_0^T \alpha_T dT$$

n is refractive index of crystal at temperature T,

$$n = n_0 + \int_0^T \frac{dn}{dT} dT$$

a_T is the thermal-expansion coefficient,

$$a_T = \frac{1}{L_0}\frac{dL}{dT}$$

λ is wavelength of light (used in this case λ =0.6328 μm), L_0 is the crystal length at temperature 0°C, T_0 is the room temperature (T_0=20°C), and n_0 is the refractive index at room temperature T_0. We adopt the nomenclature that when interference fringes are measured with the light propagating along the i-axis ($i = x, y, z$) with polarisation (electric vector direction) along the j-axis ($j = x, y, z$), we designate F as F_{ij}. Then the thermo-optical coefficients can be derived from a set of equations similar to equation (6.1) by re-writing it as follows:

$$\left(\frac{dn_j}{dT}\right)_i = \left[\frac{\lambda}{2}\frac{dF_{ij}}{dT} - (n_j - 1)a_{Ti}L_0\right]/L \tag{6.2}$$

provided that the values of the a_{Ti}'s are known. It should be noted that, of course, the value of dn_j/dT does not depend on beam propagation direction (*i.e.*, whether subscript i is equal to x, y or z). However, as will become apparent later, improved precision in evaluating dn_j/dT can result from using one particular value of i rather than another.

The Michelson interferometer gave a resolution of about $\lambda/2$. The oven containing the crystal was made of stainless steel and was insulated by a PTFE cover. A thermistor was used for feed-back control and a thermo-couple was used for temperature measurement. The temperature resolution was within ± 2°C.

As mentioned above the three thermo-optical coefficients dn_x/dT, dn_y/dT, and dn_z/dT were previously measured by Velsko *et al.* [1]. Two of them, namely dn_x/dT and dn_y/dT, were found to be independent of temperature and wavelength, but dn_z/dT was found to be wavelength dependent. Values[1] given by Velsko are:

$$\frac{dn_x}{dT} = (-1.8 \pm 0.2) \times 10^{-6} \tag{6.3}$$

$$\frac{dn_y}{dT} = (-13.6 \pm 0.1) \times 10^{-6} \tag{6.4}$$

$$\frac{dn_z}{dT} = [-6.3 \pm 0.6 - (2.1 \pm 0.8)\lambda] \times 10^{-6} \ (\lambda \text{ in } \mu m) \tag{6.5}$$

For the measured data for dn_z/dT reported in Table IV of reference[1], we note that, except for the point at 0.365 μm, dn_z/dT appears to increase only slightly with increasing wavelength. However, this variation of dn_z/dT over the range 0.45-1.064 μm is within

[1] A mistake in sign was made in the original paper[1], but has been corrected in Eq.(6.5). The error can be easily seen if the formula for dn_z/dT is compared with experimental data given in Table IV of reference [1].

$\pm 0.5 \times 10^{-6}$ and is not significant given the accuracy of the measurement. In view of the above, we have limited our measurements to only one wavelength (0.6328 μm), and our data processing has been done under the assumption that the thermo-optical coefficients for the three principal axes are independent of the wavelength.

Four measurable cases have been investigated with the use of the two available NCPM LBO crystals. With the use of the type I NCPM crystal, where the light beam propagates along the x axis, and where it may be linearly polarized along either the y axis (called measurement a) or the z axis (called measurement b), dF_{xy}/dT and dF_{xz}/dT have been measured respectively. With the use of the type II NCPM crystal, where the light beam propagates along the z axis, and where it may be linearly polarized along either the x axis (called measurement c) or the y axis (called measurement d), dF_{xy}/dT and dF_{xz}/dT have been measured respectively. The fitted formulae to our experimental results from measurements a, b, c, and d are as follows:

$$\frac{dF_{xy}}{dT} = 0.63063 + 7.9448 \times 10^{-3}T - 1.6708 \times 10^{-5}T^2 + 4.2576 \times 10^{-8}T^3 - 1.1343 \times 10^{-10}T^4 \tag{6.6}$$

$$\frac{dF_{xz}}{dT} = 1.0236 + 7.4566 \times 10^{-3}T \tag{6.7}$$

$$\frac{dF_{zx}}{dT} = 0.87683 - 1.7194 \times 10^{-4}T - 3.3417 \times 10^{-6}T^2 \tag{6.8}$$

$$\frac{dF_{zy}}{dT} = 0.55048 - 1.7111 \times 10^{-2}T + 1.2482 \times 10^{-4}T^2 - 7.3664 \times 10^{-7}T^3 + 1.4152 \times 10^{-9}T^4 \tag{6.9}$$

The error in dF/dT through data fitting are approximately $\sim 10^{-6}$.

6.2 Determination of dn/dT

In order to use Eq.(6.2) to deduce the dn/dT values from the measured dF/dT values, we need to know the values of the appropriate α's. The anisotropic thermal expansions of LBO have been deduced by Wei *et al.* [2] from their x-ray crystallographic measurement of the lattice parameters a, b and c of LBO and their temperature dependencies. In our case,

we need to know the thermal expansions along the x axis and the z axis, *i.e.*, α_{Tx} and α_{Tz} . For reasons that we will discuss subsequently, we have chosen to go back to the original experimental data reported by Wei for a, b and c as functions of temperature rather than to use the empirical formula that they derived by curve fitting . Since the x and z axes of LBO are parallel to a and b respectively, we have used the data given in Table 1 of Ref.[2] to obtain the following empirical relations for the temperature dependencies of a and b:

$$a(T) = 8.4811(1 + 4.7325 \times 10^{-5}T + 2.3162 \times 10^{-7}T^2 - 2.6507 \times 10^{-10}T^3)(\text{Å}) \quad (6.10)$$

$$b(T) = 7.4125(1 + 2.9859 \times 10^{-5}T + 1.4154 \times 10^{-8}T^2 - 2.9336 \times 10^{-11}T^3)(\text{Å}) \quad (6.11)$$

The errors in these formulae fitting were calculated by:

$$err = \sqrt{\frac{\sum_{i=1}^{m} [L_{obs}(i) - L_{fit}(i)]^2}{m - n}} \quad (6.12)$$

Where $L_{obs}(i)$ is the experimental value of a lattice parameter at temperature T_i, $L_{fit}(i)$ is the value of the same lattice parameter deduced from either Eq. (6.10) or (6.11) above at the temperature T_i, m is the number of measurement of L_{obs} and n is the order number of the fitted polynomials. The errors are 7.9×10^{-3}Å for $a(T)$, and 3.2×10^{-3}Å for $b(T)$. It should be noticed that our fitted formula for $a(T)$ gives better precision than the one given in Ref.[2], which gives an error of 1.1×10^{-2}Å (hence our decision to go back to the original experimental data).

The thermal-expansion coefficients were deduced from the definition:

$$\alpha_T = \frac{1}{L_0}\frac{dL_{fit}(T)}{dT} \quad (6.13)$$

where L_0 is the value of the lattice parameter at 0°C. Hence we obtain:

$$\alpha_{Tx} = 6.2600 \times 10^{-5} + 3.321 \times 10^{-7}T - 5.8449 \times 10^{-10}T^2 \quad (6.14)$$

$$\alpha_{Tz} = 2.9859 \times 10^{-5} + 2.8308 \times 10^{-8}T - 8.8008 \times 10^{-11}T^2 \quad (6.15)$$

where the unit of α_{Tx} and α_{Tz} is $(^oC)^{-1}$ [2]. Consequently, dn_x/dT can be evaluated by using the relation for α_{Tz} given by Eq.(6.15) and formula 6.8; dn_y/dT can be evaluated by two methods, either with the use of the relation for α_{Tz} and formula 6.9 or with the use of the relation for α_{Tx} and formula 6.6; dn_z/dT can be evaluated with the use of the relation for α_{Tz} and formula (6.7).

However, if one draws the two curves of the function dn_y/dT as a function of T that are evaluated by the two methods previously stated (as shown in Fig. 6.2, where curve

I represents the result from the first method and curve II represents the result from the second method), a difference between the two curves of approximately 3×10^{-6} can be found. If we use the empirical relation for α_{Tx} deduced by Wei *et al.* by their curve fitting to their lattice parameter measurements (equation for α_{ta} in Ref.[2]), a third curve (curve III) is obtained. The poor agreement with the other two curve highlights discrepancies in their curve-fitting procedure in this case; hence this further confirms the validity of our approach in which we have carried out our own curve fitting to their reported experimental data (Eq.(6.14) above). Although curves I and II are in reasonable agreement, we have subsequently used curve I to deduce dn_y/dT because of the higher precision in α_{Tz} compared to α_{Tx}.

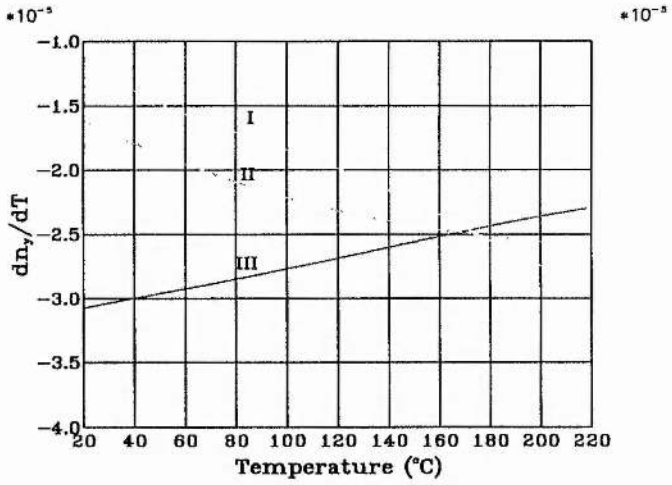

Figure 6.2: Comparison of three calculated curves for dn_y/dT against T evaluated with the use of different thermal-expansion coefficients α.

Hence, in summary dn_y/dT and dn_x/dT were determined from measurements d and c, and evaluated by the equations:

$$\left(\frac{dn_y}{dT}\right)_z = \left[\frac{\lambda}{2}\frac{dF_{zy}}{dT} - (n_y - 1)\alpha_{Tz}L_0\right]/L \tag{6.16}$$

$$\left(\frac{dn_x}{dT}\right)_z = \left[\frac{\lambda}{2}\frac{dF_{zx}}{dT} - (n_x - 1)\alpha_{Tz}L_0\right]/L \tag{6.17}$$

To determine dn_z/dT we have used a different, but related, method to the one stated above so as to reduce the influence of the lack of precision in α_{Tx}. If we evaluate $(dn_z/dT)_x$ and

$(\mathrm{d}n_y/\mathrm{d}T)_x$ with the use of Eq.(6.2), we obtain for conditions close to room temperature:

$$\left(\frac{dn_z}{dT}-\frac{dn_y}{dT}\right)_x=\left[\frac{\lambda}{2}\left(\frac{dF_{xz}}{dT}-\frac{dF_{xy}}{dT}\right)-(n_z-n_y)\alpha_{Tx}L_0\right]/L$$

$$\approx\left(\frac{dF_{xz}}{dT}-\frac{dF_{xy}}{dT}\right)\frac{\lambda}{2L_0}-(n_z-n_y)\alpha_{Tx} \tag{6.18}$$

where n_{z0} an n_{y0} are the principal refractive indices at room temperature (20°C) for the z and y axis respectively, and have values of 1.6164 and 1.6014, respectively. From relation (6.18) we see that uncertainty in α_{Tx} of $\Delta\alpha_{Tx}$ leads to an uncertainty in the left-hand side of this relation of:

$$\left|\Delta\left(\frac{dn_z}{dT}-\frac{dn_y}{dT}\right)_x\right|\approx 0.015\Delta\alpha_{Tx} \tag{6.19}$$

This is to be compared to the uncertainty in $(dn_z/dT)_x$ alone, which is given by:

$$\left|\Delta\left(\frac{dn_z}{dT}\right)_x\right|\approx(n_{z0}-1)\,\Delta\alpha T_x=0.614\Delta\alpha T_x \tag{6.20}$$

We evaluate dn_y/dT with the use of $(dn_y/dT)_z$, which is then added to relation (6.18) to evaluate dn_z/dT, according to:

$$\frac{dn_z}{dT}=\left(\frac{dn_y}{dT}\right)_z+\left(\frac{dn_z}{dT}-\frac{dn_y}{dT}\right)_x \tag{6.21}$$

If we substitute the measurement results from Eqs.(6.6), (6.7), and (6.8) into Eqs.(6.16), (6.17) and (6.21), the three principal axes's thermo-optical coefficients of LBO as functions of temperature in the range 20-200°C with unit of $(^\circ\mathrm{C})^{-1}$ can be expressed as follows:

$$\frac{dn_x}{dT}=2.0342\times10^{-7}-1.9697\times10^{-8}T-1.4415\times10^{-11}T^2 \tag{6.22}$$

$$\frac{dn_y}{dT}=-1.0748\times10^{-5}-7.1034\times10^{-8}T-5.7387\times10^{-11}T^2 \tag{6.23}$$

$$\frac{dn_z}{dT}=-8.5998\times10^{-7}-1.5476\times10^{-7}T+9.4675\times10^{-10}T^2-2.2375\times10^{-12}T^3 \tag{6.24}$$

The curves of the three principal axes's thermo-optical coefficients of LBO versus temperature are shown in Fig. 6.3. At room temperature, their values are very close to those given by Velsko *et al.*

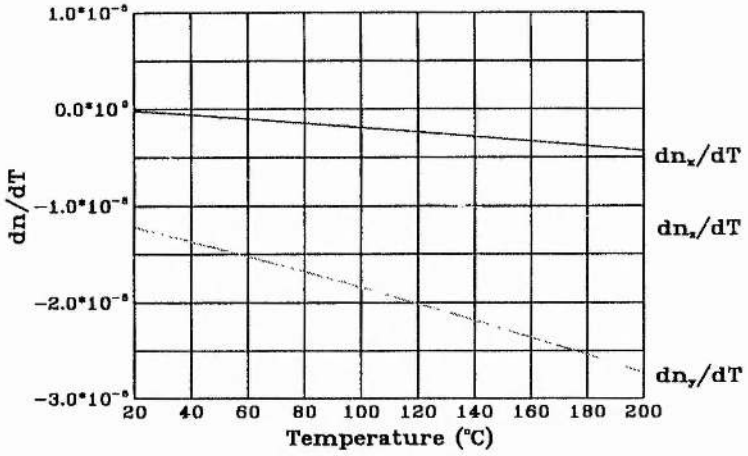

Figure 6.3: Curves of the three principal axes's thermo-optical coefficients of LBO against temperature.

6.3 Assessment

In order to verify the validity of the thermo-optical coefficients given in the previous examples, these coefficients have been used to predict phase-matching temperature and temperature bandwidth for some applications and compared with experimental results.

Figures 6.4 and 6.5 show both predicted and experimental tuning curves of type II NCPM LBO OPO pumped at 266 nm and 355 nm respectively. The data that produced the solid line were calculated with the use of our thermo-optical coefficients, and the data that produced the dotted line were calculated with the use of Velsko's coefficients; the circles represent our experimental results. It can be seen that either in Fig. 6.4 or Fig. 6.5, the solid line (our curve) is very close to the experimental results but the dotted curve is not so close, particularly in the higher temperature range. Figures 6.4 and 6.5 also show that the differences between the predicted and experimental curves increase as the temperature increases because of the accumulating error in dn/dT. At temperature 200°C the difference between our curve and the experimental curve are 0.04 μm for the idler wavelength and 0.001 μm for the signal wavelength in Fig. 6.4 and 0.02 μm for the idler wavelength and 0.0005 μm for the signal wavelength in Fig. 6.5. Figure 6.6 shows a group of temperature phase-matching curves for both type I and type II NCPM second harmonic generation. The nomenclature for these curves is the same as in Figs.

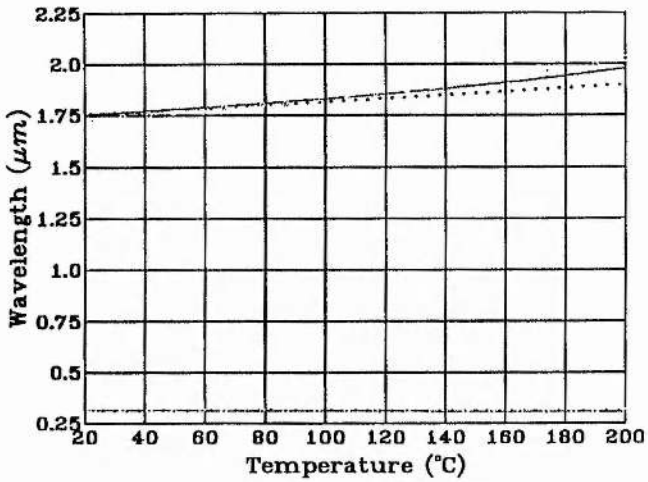

Figure 6.4: Temperature-tuning curves for type II NCPM LBO OPO's with a 266 nm pump. The circles represent our experimental results; the data that produced the solid curve were calculated with the use of our thermo-optical coefficients, and the data that produced the dotted line were calculated with the use of Velsko's thermo-optical coefficients.

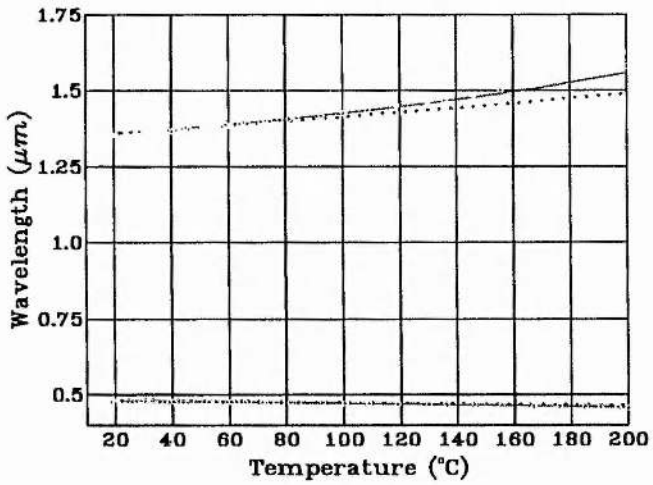

Figure 6.5: Temperature-tuning curves for type II NCPM LBO OPO's with a 355 nm pump. The curve's descriptions are the same as described in the previous figure.

6.4 and 6.5; the experimental data in this case were taken from Ref.[3]. Similarly, the phase-matching conditions calculated with the use of our thermo-optical coefficients are in closer agreement with experimental data than in the case of Velsko's coefficients.

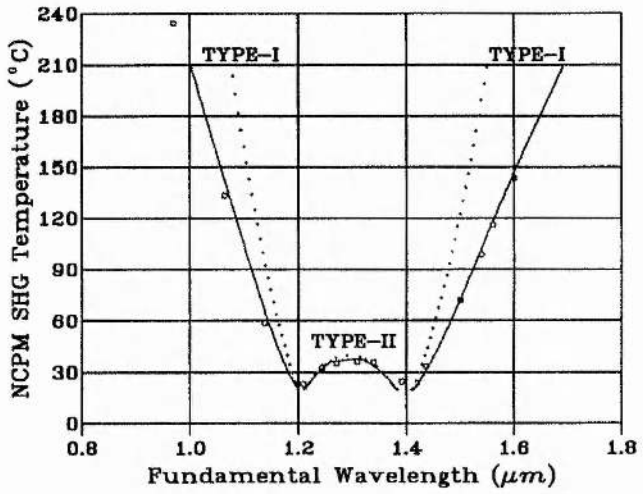

Figure 6.6: Calculated phase-matching curves for both type I and type II NCPM LBO second-harmonic generation with use of our thermo-optical coefficients (solid curve) and with the use of Velsko's coefficients (dotted curve). The circles are plotted from the experimental curve given by Lin Ref.[3].

Table 6.1: $T_{PM}(^oC)$ and ΔTL (^{o}C cm, FWHM) for some LBO SFG.

Process[a]	Type	$\lambda_1/\lambda_2/\lambda_3$ (nm)	θ_{PM}/φ_{PM} (degree)	$T_{PM}/\Delta TL$ (exp)[b]	$T_{PM}/\Delta TL$ (*cal*)[c]
NCPM SHG	I	1025/1025/521.5	90.0/0.0	190.3/3.4[d*]	184.5/3.12
NCPM SHG	I	1064/1064/523	90.0/0.0	148.5/3.94[d*]	143.5/3.95
NCPM SHG	I	1064/1064/523	90.0/0.0	149.0/4.0[e]	143.5/3.95
NCPM SHG	I	1110/1110/555	90.0/0.0	108.2/5.01[d]	94.0/5.44
NCPM SHG	I	1135/1135/567.5	90.0/0.0	77.4/4.7[e]	69.0/6.17
NCPM SHG	I	1150/1150/575	90.0/0.0	61.1/6.67[d]	55.0/6.41
NCPM SHG	I	1200/1200/600	90.0/0.0	24.3/8.58[d]	69.0/6.17
NCPM SHG	I	1064/1135/549.2	90.0/0.0	112/5[e]	106/5.04
NCPM SHG	I	1064/1908/683.1	90.0/0.0	81.0/7.4[e]	69.5/7.41
NCPM SHG	I	1064/1064/532	90.0/11.4	20/5.8[f]	20/5.85
NCPM SHG	I	1064/1064/532	90.0/11.4	20/6.4[g]	20/5.85
NCPM SHG	II	1064/1064/532	20.8/90	20/6.2[f]	20/8.6
NCPM SHG	II	1064/1064/532	20.8/90	20/8.1[g]	20/8.6
NCPM SHG	I	1064/532/354.7	90.0/37.4	20/13.6[g]	20/7.8
NCPM SHG	II	1064/532/354.7	43.1/90	20/3.7[f]	20/5.8
NCPM SHG	II	1064/532/354.7	43.1/90	20/3.9[g]	20/5.8
NCPM SHG	I	532/532/266	90.0/61.4	20/3.8[f]	20/30
NCPM SHG	I	760.5/760.5/380.2	90.0/35.85	20/15.3[h]	20/7.78
NCPM SHG	I	750/750/375	90.0/35.85	151/5.3[h]	171/5.27
NCPM SHG	I	886/886/443	90.0/24.05	20/7.8[h]	20/6.02

[a] SHG, second harmonic generation; SFG, sum-frequency mixing; CPM, critical phase-matching.

[b] Experimentally determined phase-matching T_{PM} and ΔTL. An $*$ indicates that values are measured from Fig. 10 of Ref.[4].

[c] Values of T_{PM} and ΔTL determined with the use of our experimentally measured dn/dT values.

[d] Ref.[4].

[e] Ref.[5].

[f] Ref.[6].

[g] Ref.[7].

[h] Ref.[8].

The FWHM temperature bandwidths ΔTL and phase-matching temperatures T_{PM} for some frequency conversion process have been predicted from our formulae for dn/dT. The comparison between the predicted values and experimental results which was reported in a number of papers[4, 5, 6, 7, 8] is summarised in Table 6.1. With one exception (type I critical phase-matching second harmonic generation of 532 nm), where our calculated value is nearly an order of magnitude higher than Kato's measured value, good or reasonable agreements can be seen for most of the cases listed in Table 6.1.

6.4 Temperature phase-matching properties of LBO

Some typical applications of non-critical temperature phase-matched LBO have been given in the above section. It can be noticed that the temperature tuned LBO has been mostly used for second harmonic generation, and optical parametric oscillators pumped in the ultraviolet or green. In fact, LBO also offers tunable frequency up-conversion over wide spectral ranges by sum-frequency generation. Based on our measured thermo-optical coefficients, in this section we study the temperature phase-matching properties of LBO and summarise some theoretically calculated useful non-critical temperature phase-matching conditions for applications in SHG, OPOs, and SFG.

Essentially, in the case of using type I NCPM LBO, the beam propagation direction is parallel to the x axis, so that the associated eigen refractive indices in this geometry are n_y and n_z; and in the case of using type II NCPM LBO, the beam propagation direction is parallel to the z axis, so that the associated eigen indices in this geometry are n_x and n_y. As shown in Fig. 6.3, the thermal dependencies of the three principal refractive indices are quite different. For instance, the value of dn_y/dT is nearly 7-8 times larger than the value of dn_x/dT, and more than one times larger than the value of dn_z/dT over the whole temperature range 20-200°C. Therefore, the temperature tuning would be more extensive in the type I geometry than it in the type II geometry.

(1) SHG applications: Fig. 6.6 shows that LBO is non-critically temperature phase-matchable over the near infrared region (0.9 $\mu m \leq \lambda \leq$1.8 μm) for SHG. The phase matching curves for both type I and type II show retrace behaviours. The retracing points, as reported by Lin *et al.* [3], are λ_I=1.31 μm at T=-25°C for type I, and λ_{II}=1.3 μm at T= 39°C for type II.

As shown in Fig. 6.6 and a similar curve given by Lin [3], the operating temperature

for type I NCPM SHG is limited by phase matching to be in the range $T_{pm} \geq 8°C$. In particular, the phase-matching temperature for type I SHG of 1.064 μm is found to be 143.5°C from our calculation, and it has been reported to be 148°C by Tang *et al.* [4] according to their experiment. The operating temperature for the type II NCPM geometry as the same figures show is limited to the range $T_{pm} \leq 39°C$. Within the temperature region 20-39°C, the phase-matchable fundamental wavelength range for type II SHG is 1.2 -1.4 μm.

(2) OPO applications: For optical parametric generation application, the calculated wavelength tuning curves with a range of pump wavelengths for type I and type II geometries are illustrated in Figs. 6.7 and 6.8 respectively.

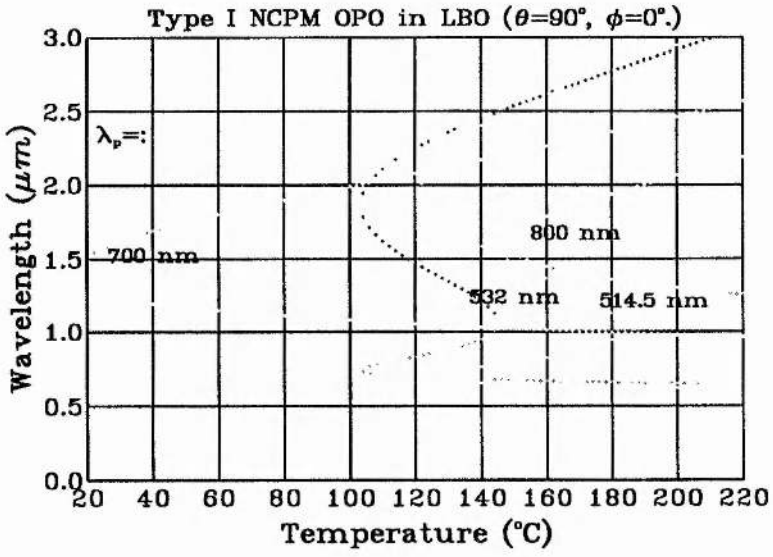

Figure 6.7: Calculated temperature tuning for type I NCPM LBO OPO's with a range of pump wavelengths.

In the type I NCPM geometry and within the temperature range 20-200°C, suitable pump wavelengths are in the range 0.5 $\mu m \leq \lambda_p \leq 0.85$ μm. An interesting feature here is the doubled value retracing behaviour when the pump is in the green (~0.532 μm). This feature offers the unique possibility of four-color radiation generation over an extensive wavelength range. Another useful feature of the type I NCPM geometry is the wide wavelength tuning range with a considerably higher tuning rate.

In the type II NCPM geometry, a much slower tuning rate than that of type I NCPM

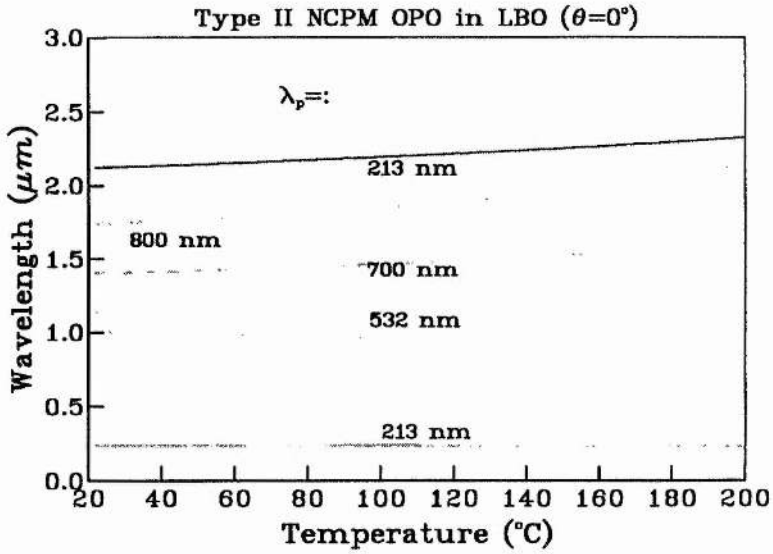

Figure 6.8: Calculated temperature tuning for type II NCPM LBO OPO's with a range of pump wavelengths.

can be seen for all the possible pump wavelengths in Fig. 6.8. This may be useful when fine frequency control is demanded. According to our calculations, LBO is type II non-critically phase-matchable for pump radiation over a wide range from the ultraviolet to the near infrared. Within the temperature range 20-200°C, suitable pump wavelengths are in the range 0.16 $\mu m \leq \lambda_p \leq 0.9$ μm.

(3) SFG applications: Finally, we discuss the temperature dependent non-critical phase-matching properties with applications in sum-frequency generation. Considering the temperature range 20-200°C, Fig. 6.9 and Fig. 6.10 show the potential wavelength phase-matchable conditions for type I and type II NCPM geometries, where we assume: $\lambda_1 \geq \lambda_2 \geq \lambda_3$, and $1/\lambda_1+1/\lambda_2=1/\lambda_3$. It shows clearly that retracing behaviour also exists in SFG, the retracing point, however is dependent on phase matching temperature.

For the type I NCPM SFG, as shown in Fig. 6.9, the wavelength phase-matchable range can be significantly extended by increasing the temperature. Within the temperature range 20-200°C, the allowed wavelength ranges are: 1 $\mu m \leq \lambda_1 \leq 2.6$ μm, 0.5 $\mu m \leq \lambda_2 \leq 1.65$ μm. This feature of wide continually phase-matchable ranges for both λ_1 and λ_2 offers the possibility of generating widely tunable light in the visible and near infrared spectral regions. This is an alternative scheme to OPOs pumped by the higher harmonics of the

Nd laser with possibility of improvement on overall efficiency. This will be discussed in Chapter 7.

In contrast, as shown in Fig. 6.10, there is a slow wavelength tuning rate with increasing phase matching temperature in type II NCPM SFG. However, an attractive feature of this type II NCPM SFG is that the wavelength phase matchable range is over the ultraviolet spectral region. This means that it is possible to generate tunable light in the deep ultraviolet region. Considering some possible available wavelengths, for example those of the Nd:YLF laser and their harmonics, or infrared radiation from OPOs, the theoretically calculated temperature phase-matching conditions are listed in Table 6.2 for type I NCPM SFG, and in Table 6.3 for type II NCPM SFG.

In conclusion, we have measured the thermo-optical coefficients of LBO with an extended temperature range (20-200°C) compared to the earlier measurements produced by Velsko. The accuracy of these coefficients are limited by the error in the α_T's (particularly for dn_x/dT because it has a relatively smaller amplitude). Although we have evaluated the temperature dependencies of the thermo-optical coefficients, we have assumed that they are wavelength independent. However, in view of the wide range of wavelengths involved in our subsequent assessment of these coefficients and the positive correlation between calculation and experiment shown therein, we believe that the predications from our measurement should provide a useful set of thermo-optical data to use to predict phase-matching temperatures with reasonable accuracy over the temperature range 20-200°C. The experimental study of SFG based on the non-critical temperature phase-matched LBO will be described in the next chapter.

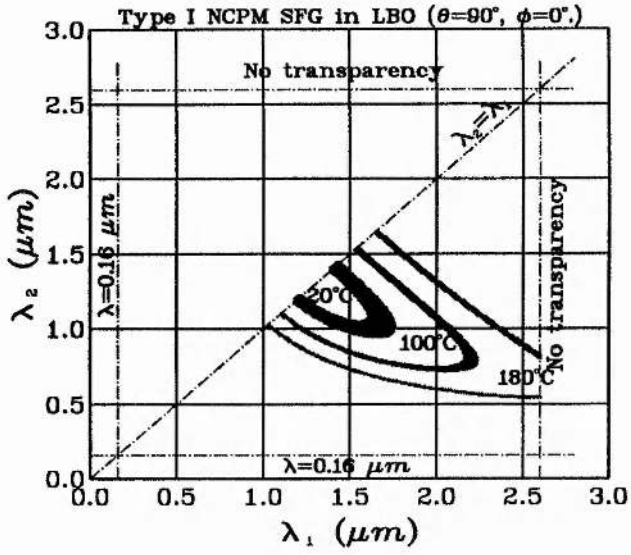

Figure 6.9: Calculated non-critical phase-matchable wavelength region for type I SFG operated by temperature tuning.

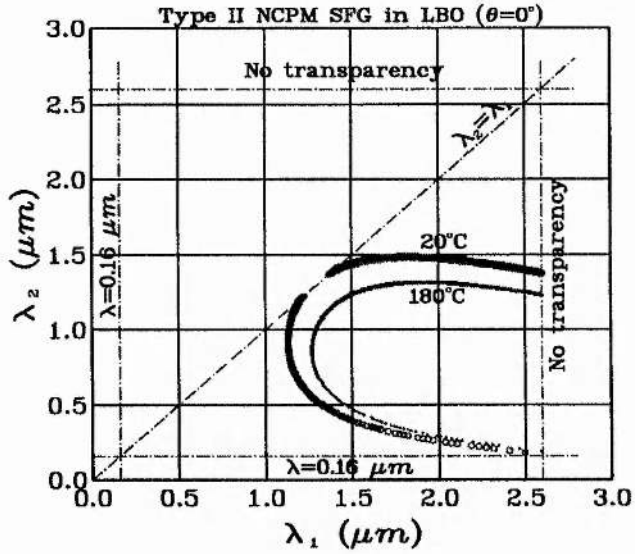

Figure 6.10: Calculated non-critical phase-matchable wavelength region for type II SFG operated by temperature tuning.

Table 6.2: Sum-frequency generation in type I non-critical phase-matched LBO by temperature tuning, where θ=90°, ϕ=0°; d_{eff}=1.05 pm/V; and acceptance angles $\Delta\theta \geq$30 mr, $\Delta\phi \geq$40 mr.

λ_1 (μm)	λ_2 (μm)	λ_3 (μm)	T (°C)
0.5235	2.38-2.6	0.43-0.436	200-193
1.047	0.98-1.48	0.506-0.613	199-20
	1.6-2.39	0.633-0.728	20-200
1.321	0.79-1.12	0.494-0.606	200-20
	1.47-2.06	0.696-0.805	20-200
1.55	0.69-1.03	0.478-0.619	200-20
	1.22-1.82	0.683-0.837	20-200
2.1	0.56-0.84-1.29	0.4422-0.6-0.799	200-85-200
2.5	0.52-0.7-0.96	0.43-0.547-0.694	198-144-200

Table 6.3: Sum-frequency generation in type II non-critical phase-matched LBO by temperature tuning, where θ=0°; d_{eff}=0.89 pm/V; and acceptance angles $\Delta\theta \geq$18 mr.

λ_1 (μm)	λ_2 (μm)	λ_3 (μm)	T (°C)
0.5235	1.29-1.43	0.372-0.383	33-190
1.047	1.13-1.33	0.5435-0.586	20-200
1.321	0.51-0.72	0.368-0.462	33-200
	0.98-1.32	0.563-0.66	200-43
	1.32-1.91	0.66-0.781	43-176
	1.92-2.6	0.783-0.876	176-96
1.55	0.38-0.45	0.305-0.349	50-200
	1.23-1.46	0.686-0.752	200-20
2.1	0.25-0.27	0.223-0.240	92-183
	1.28-1.47	0.795-0.865	199-20
2.5	0.19-0.20	0.177-0.185	87-160
	1.22-1.4	0.82-0.897	200-20

Bibliography

[1] S. P. Velsko, M. Webb, L. Davis, aand C. Huang, *IEEE J. Quantum Electron.* **QE-27**, 2182 (1991).

[2] L. Wei, G. Q. Dai, Q. Z. Huang, Z. An, and D. K. Liang, *J. Phys. D* **23**, 1073 (1990).

[3] S. Lin, B. Wu, F. Xie, and C. Chen, *J. Appl. Phys.* **73**, 1029 (1993).

[4] T. Ukachi, R. J. Lane, W. R. Bosenberg, and C. L. Tang, *J. Opt. Soc. Am. B* **9**, 1128 (1992).

[5] J. T. Lin, J. L. Montgomery, and K. Kato, *Opt. Commun.* **80**, 159 (1990).

[6] K. Kato, *IEEE J. Quantum Electron.* **QE-26**, 1173 (1990).

[7] M. S. Webb and S. P. Velsko, in Conference on Lasers and Electro-Optics (USA), OSA Technical Digest Series, **12**, paper Tuk32, (1992).

[8] D. W. Chen and J. T. Lin, *IEEE J. Quantum Electron.* **29**, 307 (1993).

Chapter 7

Tunable red light generation

This chapter describes an experimental study of temperature-tuned NCPM LBO sum-frequency generation in which light from KTP OPOs and light from the pump laser itself are mixed. The generated radiations from such a SFG device are tunable in the ranges 0.623-0.63 μm (for the case of using the NCPM KTP OPO) and 0.633-0.662 μm (for the case of using the CPM KTP OPO). Both these wavelength ranges are currently sought for medical therapies, in particular as light sources in photo-dynamic-therapy (PDT) cancer treatments.

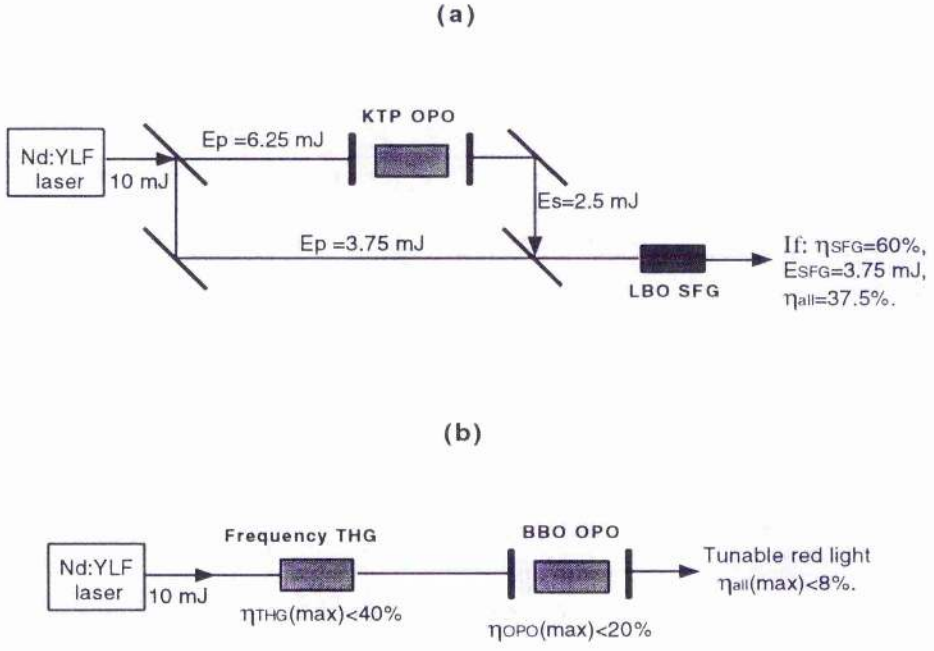

Figure 7.1: Overall conversion efficiency comparison between schemes of OPO+SFG and SFG+OPO for red light generation. (a) Scheme OPO+SFG; (b) Scheme SFG+OPO.

The use of a non-critical phase-matching condition in SFG and of highly efficient KTP OPOs are both promise well for achieving higher overall conversion efficiency in the red light generation than that associated with the standard approach, *i.e.*, SHG+SFG+OPO. For example, as the comparison given in Fig. 7.1 shows, with high enough pump laser output power, the overall conversion efficiency of this OPO+SFG system can reach 37%, while the standard approach with the use of a BBO OPO only provides a maximum 8% overall conversion efficiency.

In the following sections, we discuss the design considerations of this red light generation device and the experimental achievements.

7.1 The type I NCPM LBO crystal

As shown in Fig. 6.6, when the LBO temperature is in the range of 11-35°C, the 1 μm laser beam can be sum-frequency mixed with infrared radiation in the range 1.5 - 1.75 μm to generate tunable red light in a type I NCPM geometry. In such a scheme, the LBO crystal needs to be oriented at θ=90°, ϕ=0°, and the two input beams require to be polarized along the z-axis of the crystal; when the generated sum-frequency wave is polarized along the y-axis. As a NCPM geometry, the LBO SFG offers two advantages, *i.e.*, the maximum effective nonlinear coefficient (d_{eff}=1.05 pm/V); and the zero walk-off angle. The LBO crystal used in this work was 14 mm long with a 3×3 mm^2 aperture. The calculated acceptance parameters for this crystal length were: $\Delta\theta$=10 mr, $\Delta\phi$=12.5 mr, and ΔTL_c= 6.7°C cm. Originally, this crystal was used for green light pumped OPOs. The two optical surfaces of this crystal were uncoated, and of poor optical quality. The losses at each surface were found to be ~8% for the signal wave and ~10% for the pump wave.

7.2 Temperature control and crystal holder

The required temperature range for operation of the LBO SFG was 10°C≤ T_{pm} ≤ 35°C. Hence, a Peltier cooler was used instead of an oven to control the temperature. To keep an even and constant temperature, the crystal was placed in a brass box and the outside of the box was insulated by PTFE. The extra heat produced by the Peltier cooler was removed by circulating tap water. The temperature was controlled to within ±0.3°C. The whole

cooling block was placed in the centre of a rotation stage together with a z-dimension moveable translation stage fixed underneath, so that the crystal was moveable along the beam propagation direction (z) and finely rotatable along the vertical, horizontal and z directions.

7.3 Beam focusing and conversion efficiency

The model for calculating conversion efficiency in SFG has been given in Chapter 2, which while considering the depletions of the input waves, was based on a plane wave theory. Therefore, in this model the beam spot size, and hence the intensity of waves, were regarded as independent of position, z, within the crystal. This is only an appropriate approximation in the case of soft focusing. However, due to the low pulse energy of the pump laser, tight focusing the input beams down to ≤ 0.08 mm was an essential condition to achieve the high intensities required in this work. Typical signal and pump profiles around the focal point are depicted in Fig. 7.2. It can be seen that the beams are highly divergent for such tight focusing, and their confocal parameters z_o ($z_o = \pi W_o^2 n/\lambda$) are comparable to the crystal length. Our theoretical calculations only provide some sort of average result, and when used with the beam spot sizes equal to the focused beam waists, do, in fact, describe an upper limit.

The calculated energy conversion efficiency curves against input beam focusing are shown in Fig. 7.3, with input pulse energy at λ_1, E(λ_1), as parameter (the other input energy at λ_2, E(λ_2) was fixed by the wavelength ratio, *i.e.* E(λ_2)= E(λ_1) λ_1/λ_2, λ_1 is the signal wavelength of the KTP OPO, λ_2=1.047 μm.). Both beam cross-sections inside of the crystal have been assumed to be equal to $\pi W_o'^2$. As the input waves are increasingly focused down, so, the beam divergence correspondingly increases. The phase mismatching which enters as a factor in the calculation was given as:

$$\Delta k = \frac{\delta \Delta k}{\delta \alpha} d\alpha + \frac{1}{2} \frac{\delta^2 \Delta k}{\delta \alpha^2} (d\alpha)^2$$

where $d\alpha$ represents the angle of divergence (for the focused beam $d\alpha = \frac{\lambda}{\pi W_o'^2}$).

The conversion efficiency allowing for the beam divergence is illustrated in Fig. 7.3 by the solid curves, and the dashed curves indicate the conversion efficiency for the case of zero phase-mismatching (Δk=0). It can be seen that for the loose focusing case, the curves agree well with each other, but for the tight-focusing case the solid curves drop down dramatically while the dashed curves reach their peak.

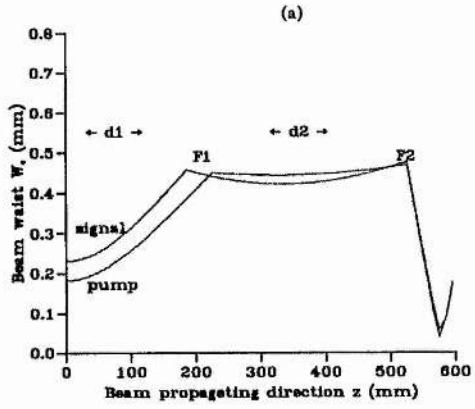

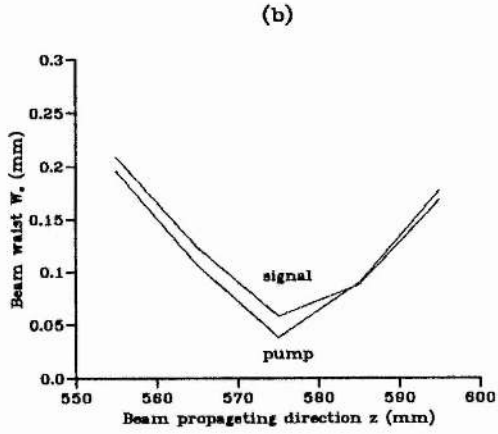

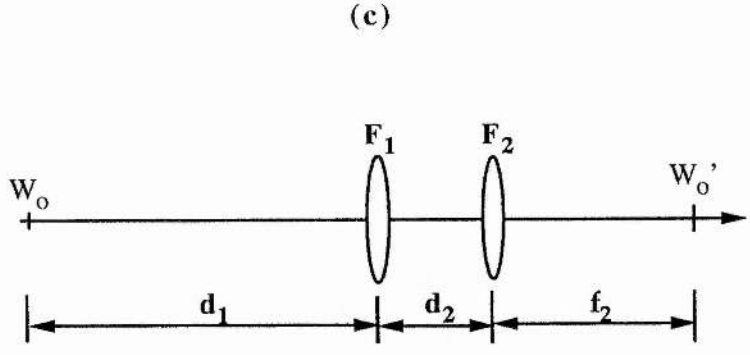

Figure 7.2: (a) Focused beam profiles of signal and pump beams. (b) Enlarged beam profiles around the focusing point. (c) Beam focusing scheme, where for pump wave, W_{op}=0.2 mm, d_1=225 mm, F_1=250 mm, d_2=300 mm, F_2=50 mm, and W'_{op}=0.038 mm; and where for signal wave, W_{os}=0.23 mm, d_1=185 mm, F_1=200 mm, d_2=340 mm, F_2=50 mm, and W'_{op}=0.058 mm.

This means that although tight focusing increases the intensity at the centre of the crystal, sum-frequency generation is limited by the beam divergence and the resulting large phase-mismatching.

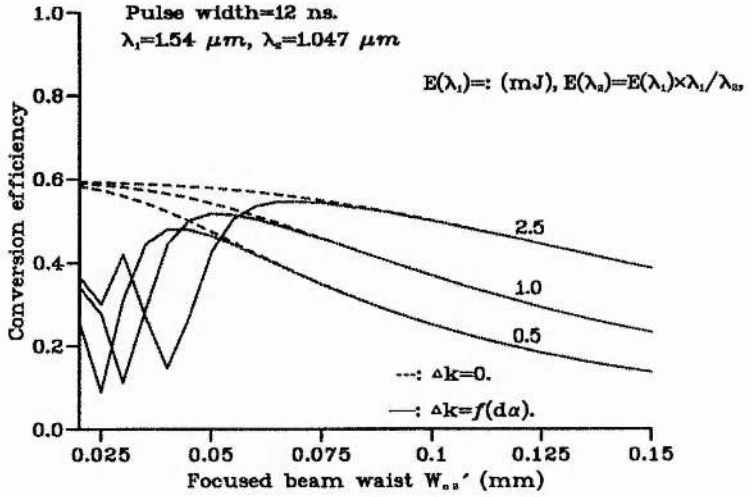

Figure 7.3: Calculated conversion efficiency curves for red light generation as function of beam waist with phase-mismatching as parameter.

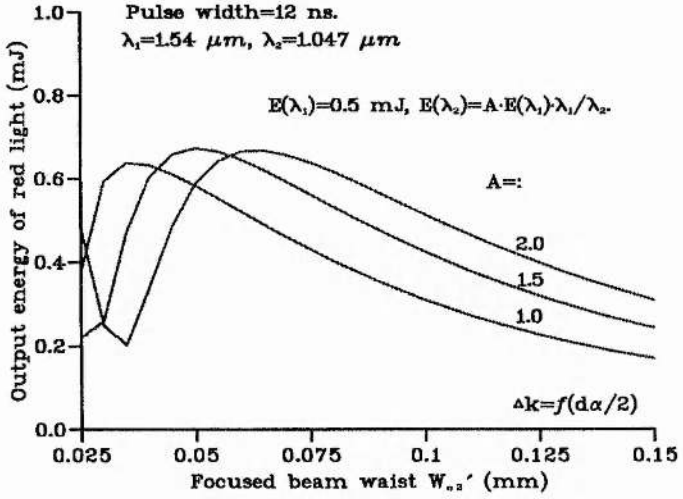

Figure 7.4: Calculated conversion efficiency curves for red light generation as a function of beam waist with different ratios of input energy as parameter.

Another important consideration is that the energy ratio of the two input waves may not

be exactly equal to the photo energy ratio, *i.e.*, $E(\lambda_2)/E(\lambda_1) = \omega_2/\omega_1$. If so, how would an inappropriate energy ratio affect the conversion efficiency? Fig. 7.4 shows numerically simulated results for the case of $E(\lambda_2) = A \times E(\lambda_1)\ \omega_2/\omega_1$, where A=1, 1.5, and 2. We can see that as the factor A increases, the peak of the conversion efficiency curve moves towards the larger beam waist.

7.4 Experiment

The main problem in the LBO NCPM SFG experiments was the low pulse energy of the pump lasers. For example, the maximum output power of the EO Q-switched laser at this time was ~3.5 mJ. If one divides the pump laser into two parts in the ratio shown in Fig. 7.1 and uses one part to pump the KTP OPO, the expected signal output of the KTP OPO will be ~0.73 mJ (assuming η_{OPO}=35%). From Fig. 7.2 (a), it can be seen that the optimum focusing condition for this case ($E(\lambda_1) \leq 1$ mJ) is $W_o' \simeq 0.05$ mm. For such a tightly focused condition, three experimental configurations were investigated in our work. The first one was a directly focused configuration, where the LBO was placed in the output path of the OPO, and the pump and signal beams were then focused using the same focusing lens. The second one was a folded configuration, where the pump laser beam was divided into two parts by a 90° beamsplitter, one part going to pump the OPO, while the other part propagated directly into the LBO crystal. The third one was an intracavity configuration, where the LBO crystal was placed inside of the OPO cavity.

7.4.1 The first configuration

We know that an advantage of the scheme KTP OPO(type III) + LBOSFG(type I) is that the signal and pump waves can be directly focused into the type I LBO SFG because they have the same polarisation direction. Therefore, the first SFG configuration is the most simple structure of the three. The experimental set-up is shown in Fig. 7.5.

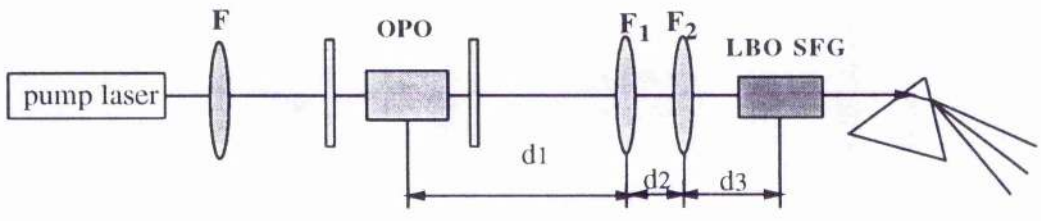

Figure 7.5: Experimental set-up of the first construction for red light generation.

In this configuration, two lenses, F_1 and F_2, were used to focus the pump and signal beams for the SFG process. The function of F_1 was to collimate the two beams, hence F_1 was placed at a distance $d_1 \simeq f_1$ from the centre of the OPO cavity. F_2 then acted as a focusing lens, and was placed as close as possible to F_1. The LBO crystal was then placed at the image point (focusing point) of F_2.

Here, both the AO and EO Q-switched pump lasers were used for the experiment.

(1) EO Q-switched pump laser: In this case, the two focusing lenses, F_1 and F_2, were chosen to be f_1=500 mm, f_2=125 mm. Using the optical ray tracing method, the pump and signal beam waists at the focal point were found to be W'_{op}=0.049 mm, W'_{os}=0.056 mm respectively. When the pump laser output was 4 mJ, 12 ns, the signal output from the NCPM KTP OPO(single-pass-pump) was 0.54 mJ, and 0.2 mJ red light at 0.623 μm was detected. The experimentally achieved conversion efficiency was, obviously, much lower than the theoretically predicted upper-limit value (see the curve with the parameter of $E(\lambda_1)$=0.5 mJ given in Fig. 7.3).

(2) AO Q-switched pump laser: In this case, the focal lengths of the two focusing lenses were chosen to be $f_1=f_2$=125 mm. From calculation, the focused pump and signal beam waists can be found to be: W'_{op}=0.0716 mm, W'_{os}=0.1 mm respectively. When the laser was pumped on each facet with 5 watts of diode light and Q-switched at a 3 kHz repetition rate, the average output power of the signal light from the intracavity KTP OPO was 100 mW with 15~20 ns pulse width. The depleted pump output was measured to be 200 mW, but its peak power was found to be only half that of the signal peak power, and its pulse profile was wide ($\sim$ 70 ns) and flat. 14 mW average output power of the red light was detected in this case.

Obviously, one problem in this configuration was that the pump and signal pulse profiles are uncontrollable. Moreover, for a highly efficient KTP OPO, there is inevitably a poor temporal overlap between the signal and pump pulses due to the pump depletion. In fact, for the case of using the EO Q-switched pump laser, a large portion of the pump energy was wasted because of the low output power of the signal light; and for the case of using the AO Q-switched pump laser, the signal energy was wasted because the highly depleted pump pulse.

To improve the energy partitioning, the second configuration was considered.

7.4.2 The second configuration

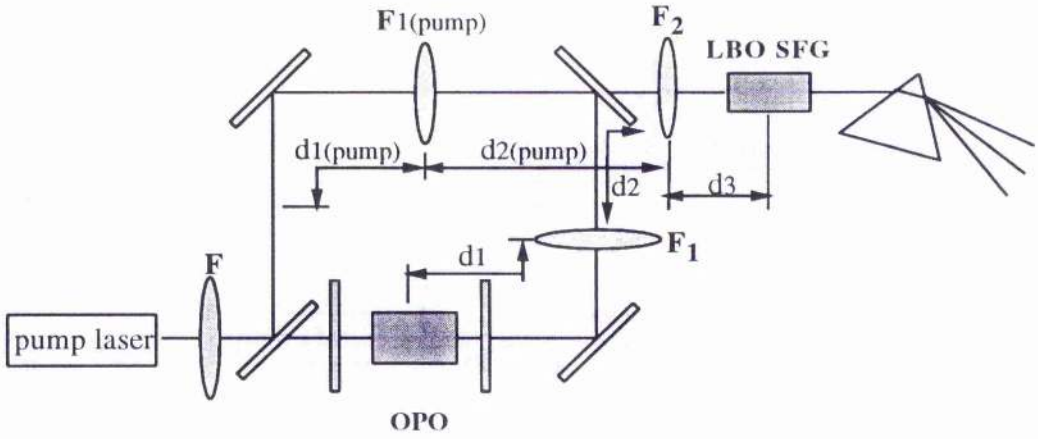

Figure 7.6: Experimental set-up of the second construction for red light generation.

The experimental set-up of the second SFG configuration is shown in Fig. 7.6, where only the EO Q-switched laser was used for the experiment. In this scheme, the pump beam was separated into two parts for the purpose of using one part to pump the KTP OPO while keeping the other part undepleted for the SFG. In front of the LBO crystal, the pump and signal beams were collimated individually by two lenses, which were F_1 and F_1(pump). The collimated beams were then combined by a 45° dichroic mirror and focused down by the lens F_2. Typical parameters of this focusing system are indicated in Fig. 7.2, the focused pump and signal waists, according to calculation, were: w'_{op}=0.038 mm, w'_{os}=0.058 mm respectively. In this experiment, by using a 45° beam-splitter we firstly divided 45 mW average pump power into two parts in the ratio of 2:1, *i.e.*, 30 mW went to pump the KTP OPO, and 15 mW went to the LBO crystal. In a double-pass-pump OPO scheme, 9 mW of signal output power was achieved at the 30 mW pump level. The energy ratio between the signal and the pump for the LBO SFG was P_p/P_s=15/9≃1.6, and this is close to the photon energy ratio, λ_s/λ_p=1.47. Behind a prism, a maximum of 6 mW of red light was detected. Taking the losses on each optical surface[1] into account, it can be shown that the conversion efficiency of the SFG process had reached to 30%, and the overall conversion efficiency from the pump to the red was more than 13%. For such a low pump energy level, the theoretical curves given in Fig. 7.3 indicate that the potential maximum conversion efficiency of the SFG process alone is ~40%.

There are several advantages in this SFG configuration. First, it is convenient to be able

[1]All the optical components used here, including the focusing lenses, crystal and the prism, were not coated.

to adjust energy partitioning between the pump and signal. Secondly, although there is always 1~2 ns delay of signal pulse due to the signal field build up, with equal distances between the beamsplitter and the centre of the LBO for both legs, the two beams can be well overlapped temporally with no pump depletion problem. Thirdly, it allows the use of a double-pass-pump configuration for the OPO, and hence increases the overall efficiency.

As our theoretical predictions show, at high pump energy levels with improved coatings, the maximum conversion efficiency of the LBO SFG process can be as high as 65%, and the overall conversion efficiency can reach to 40% (if the conversion efficiency of the KTP OPO is 40%.). This has been proved by L. Marshall *et al.* [1] recently, who reported a similar SFG scheme for uv generation at 0.289 μm with 65% conversion efficiency for the SFG and 25% for the overall conversion efficiency when the pump laser output energy was 30 mJ.

7.4.3 The third configuration

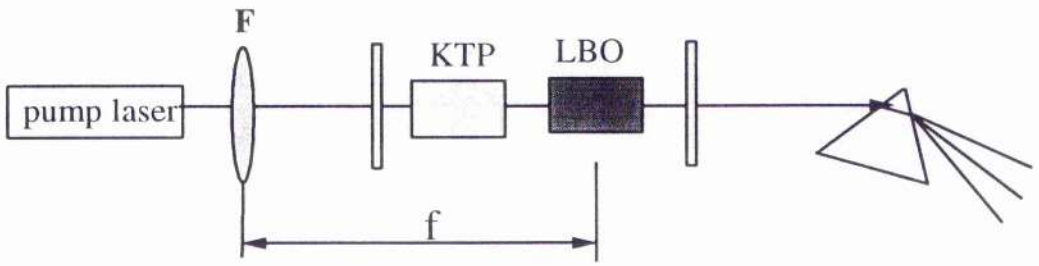

Figure 7.7: Experimental set-up of the third construction, intracavity OPO+SFG, for red light generation.

The third SFG configuration was an intracavity scheme, in which the LBO was placed inside the OPO cavity. With no additional focusing elements required for the SFG, this configuration has several advantages. Firstly, SFG is driven by the high intracavity signal power. Secondly, the pump power depletes in both the OPO and SFG crystals with freedom to distribute appropriately between the two crystals. Thirdly, the signal and pump waves are well overlapped with each other both spatially and temporally.

The experimental set-up is shown in Fig. 7.7, where again only the EO Q-switched laser was used in this experiment. The KTP was placed at the pump beam waist, and the output mirror of the OPO cavity was a high reflector for the signal wave and high transmitter for the pump wave. When the input average pump power was 63 mW, 6 mW red light was detected behind a prism. On detuning the LBO crystal by increasing the crystal

temperature, the signal output was found to rise to 10 mW.

An observed interesting phenomenon was: when we moved the LBO to the pump focus point and took the output mirror off, 3 mW of red light output was still detected, while the signal output power was found to be 4 mW on detuning the LBO. This means that the signal wave of the OPO oscillated between the rear mirror and the LBO surface, the OPO cavity in such a case being concave-plane, with the beam waist of the signal located inside of the LBO crystal.

Obviously, this intracavity configuration can be improved by using a double-pass-pump scheme for both the OPO and the SFG. This would require coating the output mirror for high transmission at the red wavelength, high reflection at both the pump and signal wavelengths, and coating the rear mirror for high reflection at the red and signal wavelengths. However, further work was limited due to the absence of such mirrors.

7.5 Phase-matching temperature and the wavelength tuning

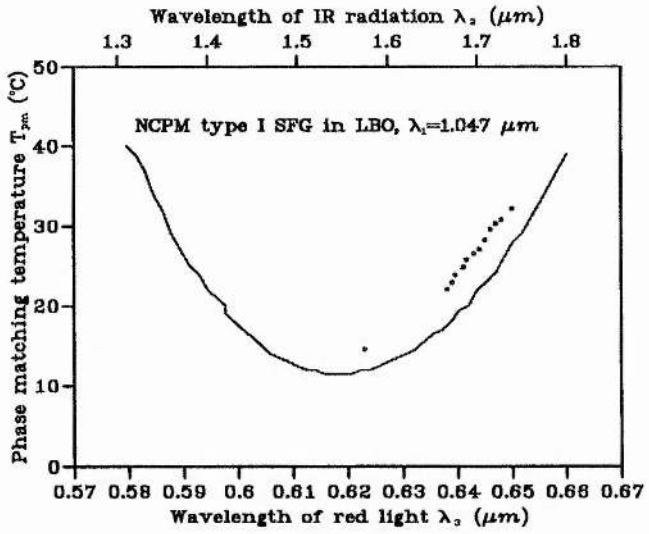

Figure 7.8: Phase-matching temperature curve of red light generation in type I NCPM LBO.

The wavelength of the generated tunable red light for the cases of using the NCPM KTP OPO and the CPM KTP OPO has been measured as the curve (scattered dots) shows

in Fig. 7.8, where the solid curve represents theoretical predictions. The experimentally achieved red light tuning range was 0.623-0.65 μm when the temperature was tuned in the range of 14.6-34°C. The slightly higher phase-matching temperatures observed in the experiment compared to our predictions are possibly due to that the thermal-sensor being placed too close to the hot-side of the Peltier elements.

7.6 Conclusion

We believe that we have demonstrated for the first time tunable light generation by sum-frequency generation in a non-critical temperature phase-matched LBO crystal. The NCPM geometry of the SFG, and the availability of a highly efficient infrared OPO (like the KTP OPO) have opened up a significant opportunity for this frequency up-conversion scheme to be both highly efficient as well as realisable as a robust device.

Bibliography

[1] L. Marshall, *LASER FOCUS WORLD* 83-87, April (1994).

Chapter 8

Conclusions

Based on a study of the newly developed nonlinear optical materials, potassium titanyl phosphate and lithium triborate, we have demonstrated two highly efficient tunable frequency-up and -down conversion schemes, *i.e.*,

- The low-threshold, high-efficiency all-solid-state KTP OPO tunable from 1.54 to 1.84 μm (signal) and 3.3 to 2.6 μm (idler).

- The all-solid-state NCPM type I LBO sum-frequency generation scheme tunable from 0.623 to 0.65 μm.

To our knowledge, the ~40% external conversion efficiency from the pump to the signal of the CPM KTP OPO, and the tunable sum-frequency generation based on the non-critical temperature phase-matched LBO are the first demonstrations of such devices.

The principal conclusions of this work are as follows:

Guha's model provides a practical and useful method for pump threshold calculation for OPOs. In this work, we have made two contributions to further extend this model. The first is the extension to make it suitable for any type of phase-matching of a SRO. The second is the extension to make it suitable for the double-pass-pump SRO configuration.

The matching of the pump and signal beams to enable the greatest power transfer from the pump to the signal and idler waves is an important factor in a parametric interaction process, and it is measurable by the introduced parameter $h_{sm}(\xi, B)$. The comparison

of operating characteristics between the AO Q-switched laser pumped KTP OPOs and the EO Q-switched laser pumped KTP OPOs presented in our work has experimentally proved how important the h_{sm} value of an OPO system is. Therefore, the calculation of the h_{sm} parameter is shown to be a useful tool in OPO design.

At high pump intensity levels for an OPO, a high value of signal output coupling T is needed to avoid back-conversion. For the same pump intensity, the intracavity signal intensity will also be lower for large values of T, which should reduce the chance of optical damage to the crystal.

The double-pass-pump and the intracavity OPO have been demonstrated to be the most effective configurations for low-threshold, high-efficiency and TEM_{00} operation of singly-resonant OPOs, and the two configurations will be particularly important in a critical-phase-matching geometry where only the non-resonant wave is an extraordinary wave.

A useful set of thermo-optical coefficients for LBO has been deduced experimentally in this work, and they can be used to predict temperature phase-matching conditions in the range of 20-200°C.

Our study has shown that LBO is non-critical temperature phase-matchable for SFG over a large wavelength range. In particular, type I NCPM LBO SFG is suitable for generating tunable light in visible, and near infrared spectral regions; and type II NCPM LBO SFG is suitable for generating tunable light from the visible to the deep uv spectral regions.

The tunable red light generation device based on the highly efficient KTP OPO and NCPM LBO SFG shows great promise as a novel tunable frequency up-conversion scheme, with much higher overall conversion efficiency than standard frequency up-conversion schemes (SFG+OPO).

The successful development of KTP OPOs and the study of the LBO NCPM SFG have opened the door for future work with several opportunities. As we have mentioned in chapter 3, KTA and other isomorphs of KTP are good alternative materials for the OPO when tunable light in the range 2-5 μm is required. The similar phase-matching properties and the relatively higher nonlinear effective coefficient of these materials should provide similar operating characteristics to the KTP based OPO. The essential phase-matching condition of the NCPM LBO based SFG is that one input wave has to be infrared, and the other wave can be any wavelength from the near infrared to as short as the cut-off wavelength of LBO, namely 0.16 μm. Therefore tunable light in the spectral regions from

the visible to deep uv can be generated effectively in the scheme infrared OPO + NCPM LBO SFG, in which the pump laser is separated into two legs, one is up-converted into its second, third, ..or fifth harmonic frequency, and the other one is down converted into tunable infrared light by the OPO, and then both lights are mixed in the NCPM LBO for the tunable up-conversion generation. This frequency up-conversion scheme, we believe, is particular important for the uv and the deep uv spectral regions.